Modeling the Fluid Dynamics of a Commercial Ebullated Bed Hydroprocessor

by

Christopher D. Lane

Submitted in partial fulfilment of the requirements
for the degree of Doctor of Philosophy

at

Dalhousie University
Halifax, Nova Scotia
June 2016

Dedication

To my mom, dad, Ciarán, Brendan, and Caitlin.

Table of Contents

List of Figures

List of Tables

Abstract

Due to the nature of bitumen extracted from Canada's Athabascan oil sands, upgrading of this heavy oil to lighter, more valuable, products is required. Ebullated bed hydroprocessors are used for the conversion of bitumen residue from atmospheric, and vacuum, distillation tower bottoms to lighter petroleum products. Studies in support of these industrial hydroprocessors have demonstrated that gas holdup within the reactor is higher than predicted. High gas holdup is unfavorable because it displaces the unconverted liquid hydrocarbons, thereby reducing the liquid phase residence time and overall pitch conversion. Due to the complex interactions between the gas-liquid-solid phases, estimation of liquid residence time, and catalyst bed fluidization behavior are dependent on a thorough understanding of the multiphase fluid dynamics.

High gas holdup has been attributed to the entrainment of gas bubbles by the internally recycled liquid. However, previous studied have not addressed the impact of the gas-liquid separation in the freeboard region of the hydroprocessor. This thesis presents a novel fluid dynamic model of an industrial ebullated bed hydroprocessor that accurately accounts for the gas-liquid separation dynamics in the freeboard. Analysis of the freeboard region multiphase flow was conducted by computational fluid dynamics (CFD) to characterize gas entrainment by the recycled liquid phase. A correlation of gas separation to liquid residence time was observed and validated with commercial pilot plant data. Outcomes of this numerical study demonstrated a sensitivity of the gas separation to the bubble drag coefficient. Using an analog fluid system, a bubble swarm drag coefficient correlation was experimentally investigated at atmospheric and elevated pressures. As pressures increased, swarm effects attenuated for bubbles within the optical probe detection limits. Based on these results, comparisons of previous generation separators were completed using CFD. Enhanced separation was primarily due to improved removal of large bubbles, providing insights for future design improvements. These results were incorporated into an integrated fluid dynamic model of an ebullated bed hydroprocessor, and a parametric analysis was conducted to determine the sensitivity of reactor gas holdup to separation efficiency.

List of Symbols Used

a	Fitted parameter for foaming correlation
A	Cross-sectional area of column annulus
A_r	Cross-sectional area of radial position r
$A_{projected}$	Projected area of bubble
Ar	Archimedes number $\left(\mathrm{Ar} \equiv \frac{g d_v \rho_l (1-\rho_l)}{\mu^2}\right)$
b	Fitted parameter for foaming correlation
B	Fitter parameter for separation efficiency correlation
Co	Courant number $\left(\mathrm{Co} \equiv u_i \frac{\partial t}{\partial x}\right)$
C_D	Drag coefficient for a single bubble in a swarm
$C_{D\infty}$	Drag coefficient for an isolated single bubble in a quiescent liquid
$C_{D,swarm}$	Swarm drag coefficient correction factor
$C_{l,x}$	Concentration in liquid at boundary x
$\mathrm{C_{VM}}$	Virtual mass coefficient
$\mathrm{C_{lift}}$	Lift coefficient
d_b	Bubble diameter
d_c	Bubble chord length
d_V	Volume equivalent diameter
D_T	Column diameter
dP/dX	Pressure drop along length of column
dV	Differential volume
e_{gg}	Restitution coefficient
Eo	Eötvös number $\left(\mathrm{Eo} \equiv \frac{g d_b (\rho_l - \rho_g)}{\sigma}\right)$
F_D	Force due to drag
F_P	Force due to pressure (buoyant force)
F_G	Force due to gravity
Fr	Froude number $\left(\mathrm{Fr} \equiv \frac{u}{\sqrt{gL}}\right)$
g	Gravitational acceleration
$g_{0,gg}$	Radial distribution function
k	Wall effect coefficient
L_s	Sensing length (instrumentation calibration value)
M	Momentum
M_{drag}	Momentum drag term
M_{lift}	Momentum lift term
M_T	Total momentum
M_{VM}	Momentum virtual mass term
Mo	Morton number $\left(\mathrm{Mo} \equiv \frac{g \mu_l^4 (\rho_l - \rho_g)}{\rho_l^2 \sigma^3}\right)$

$\dot{m}_{l,x}$	Liquid mass flow rate at boundary x
n	Richardson-Zaki exponent
n_b	Bubbles detection count
N	Number of bubbles in volume
P	Pressure
Pe	Péclet number $\left(\mathrm{Pe} \equiv \frac{Lu}{D}\right)$
R	Reynolds stress tensor
$\mathcal{R}$	Liquid recycle fraction
Re	Reynolds number $\left(\mathrm{Re} \equiv \frac{Lu\rho}{\mu}\right)$
Re_b	Bubble-liquid Reynolds number
$\mathrm{Re}_{LT\infty}$	Particle-liquid Reynolds number based on terminal free settling
u_b	Bubble rise velocity
$\overline{u_b}$	Average bubble velocity
$u_{b\infty}$	Single isolated bubble rise velocity
U_G	Superficial gas velocity
u_l	Interstitial liquid velocity
U_L	Superficial liquid velocity
$U_{LT\infty}$	Terminal free settling velocity of a particle
u_s	Bubble slip velocity (relative velocity to liquid interstitial velocity)
u_{slip}	Gas-liquid slip velocity
t	Time
t_r	Rise time
t_b	Time-on-probe
V_s	Volume of active separation region
Z	Dimensionless length

Greek symbols

α	Gas phase fraction
β	Dimensionless similitude group
ε_i	Gas holdup for phase i
ε_s	Solids holdup
ε_g	Gas holdup
ε_l	Liquid holdup
η	Separation efficiency
θ	Dimensionless time
Θ_g	Granular temperature of the bubbles
κ	Mean liquid residence time

μ_L	Liquid dynamic viscosity
ν_L	Liquid kinematic viscosity
$\mathcal{R}$	Liquid recycle fraction
ρ	Density
σ	Surface tension
τ	Laminar stress tensor
ϕ	Sphericity

Subscripts

b	Bubble
g	Gas phase
i	Bubble class size i
l	Liquid phase
p	Particle
r	Radial position r
s	Solid phase
t	Time t

Acknowledgements

I would like to acknowledge, and sincerely thank, Dr. Adam Donaldson for the opportunity, mentoring, and support he provided throughout my graduate studies. The influence of his valued input and guidance is pervasive throughout this work.

I would like to acknowledge Dr. Arturo Macchi for the many discussions and input into this work. I also want to thank him for graciously inviting me to collaborate with him and his lab group at the University of Ottawa.

I would like to acknowledge Valois Parisien for the collection of data related to the bubble drag study and comments on other portions of the work. Also, I sincerely appreciate our constructive debates, many of which were inspirational and instrumental to this work.

I would like to acknowledge Syncrude Canada Ltd. for their support and interest in this work and contribution of data related to the AMOCO pilot plant study. In particular, Craig McKnight, Jason Wiens, and Kevin Reid whose advice and guidance made this work possible.

I would like to acknowledge my committee members Dr. Dominic Groulx, Dr. Jan Haelssig, and Dr. John Grace for reviewing this work and their advisement.

1 Introduction

The bituminous sands of Canada's Athabascan region are one of the largest unconventional oil reservoirs in the world (Owen et al., 2010). The bitumen recovered from the sand matrix is a high molecular weight homogenous mixture of saturated and unsaturated hydrocarbons, aromatics, resins, and asphaltenes contaminated with high metal and sulfur content. The bitumen recovered from the sand is unsuitable for conventional refining and must be upgraded to a marketable synthetic crude for conventional oil refining and transportation purposes. An important part of this upgrading process is the conversion of high molecular weight bitumen residue to lighter oil products such as gas oil and petroleum distillate through hydrocracking processes.

1.1 Canadian Synthetic Crude Oil Production from Athabasca Bitumen

Syncrude Canada Ltd. is a major Canadian producer of synthetic crude oil through mining, extraction and upgrading of bitumen retrieved from the oil sands of the Athabascan region of Alberta. In the Syncrude process, ebullated bed hydroprocessors are implemented for the conversion of bitumen residue. An overview of this process provides context for how ebullated bed hydroprocessors integrate into the larger bitumen extraction and upgrading process.

Initially, mined bitumen sand is transported to extraction vessels, including tumblers and froth flotation separators. In the froth floatation separator, the addition of hot water creates a slurry where the bitumen separates from the sand and films around local gas bubbles, which rise to the top of the separator, allowing the bitumen froth to be collected. A secondary froth floatation separator downstream may collect middlings from the primary separator for further bitumen recovery. The remaining mixture of water, sand, fines, and unrecovered bitumen,

referred to as tailings, is removed to a tailings pond. Recovered froth is deaerated and further treated to remove remaining water and solids. Treatment of the recovered froth may include the addition of naphtha to promote separation of bitumen from the water (Romanova et al., 2013). The bitumen is then fed to an atmospheric distillation tower, where naphtha is recovered. Atmospheric tower bottoms (ATB) are further separated downstream via a vacuum distillation tower. A mix of atmospheric and vacuum tower bottoms (VTB), referred to as pitch or bitumen residue, are fed to hydrocracking processes, where high molecular weight molecules are converted to lighter products, before being sent to fixed bed hydrotreaters for final nitrogen and sulfur removal to produce a synthetic crude oil.

A range of hydrocracking processes has been developed to convert bitumen into higher value products including coking, visbreaking, catalytic cracking, solvent deasphalting, and hydroprocessing. Hydroprocessing, encapsulating hydrocracking and hydrotreating, is carried out in either fixed, moving, ebullated, or slurry bed reactors which differ primarily in their tolerance for feedstock quality, conversion, and difficulty of operation. Ebullated bed reactors, licensed primarily through LC-Fining^{SM} and H-Oil^{RC} technologies, have demonstrated residue conversion in the range of up to 80% (Sahu et al., 2015).

1.2 Ebullated Bed Hydroprocessor in Athabascan Bitumen Upgrading

Ebullated bed hydroprocessors are three-phase (gas-liquid-solid) fluidized bed reactors in which a bed of cylindrical zeolite catalyst, impregnated with Nickle Oxide (NiO) and Molybdenum Oxide (MoO_2), is fluidized by a co-current gas-liquid stream, consisting of hydrogen gas bubbles and a liquid mixture of ATB and VTB. A typical LC-Finer^{SM} hydroprocessor, presented in Figure 1.2.1, operates at approximately 440 ℃ and 12 MPa (McKnight et al., 2003) promoting thermal and catalytic hydrolysis of feedstock hydrocarbons

which are subsequently terminated by the dissolved hydrogen through the ideal reaction pathway.

Internal to the reactor is a central recycle line and pump. Above the fluidized catalyst bed, in the reactor freeboard region, a recycle pan enables separation of gas from the liquid stream. A major fraction of the liquid is subsequently internally recycled, mixing with fresh liquid feedstock and hydrogen below the distributor grid. External nuclear densitometers provide measurements of the average density of the fluid at their vertical position, located above and below the desired bed height. Due to the complex nature of the multiphase flow inside ebullated beds, there is still uncertainty surrounding the internal fluid dynamics of the unit. Improved understanding of fluid dynamics of modern hydroprocessors can lead to technology advances improving hydroprocessing efficiency thereby improving the economic viability of this upgrading process and reducing associated process emissions.

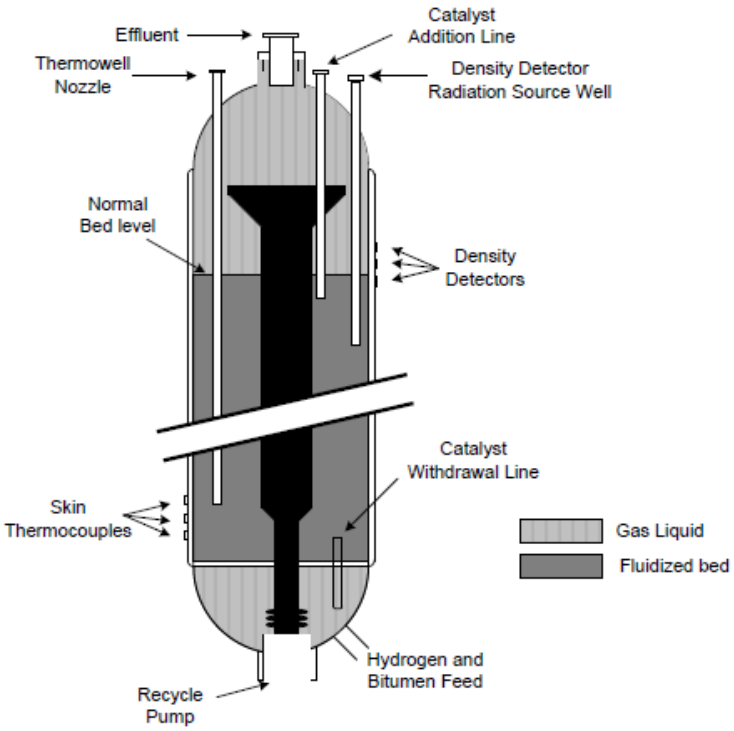

Figure 1.2.1: LC-Finer[SM] schematic (modified from McKnight et al., 2003).

1.3 Gas holdup in a Commercial Ebullated Bed Hydroprocessor

Freeboard gas holdup within an LC-Finer[SM] ebullated bed hydroprocessor has been reported, at commercial scale, to be above 50% (McKnight et al., 2003). Figure 1.3.1 illustrates gas holdup measurements for LC-Finer[SM] units compared to gas holdup estimates using the correlations of Pruden et al. (1993) and Hughmark et al. (1967), assuming no internally recycled gas. The high gas phase holdup observed is unfavorable because it displaces the unconverted liquid pitch, thereby reducing the liquid phase residence time and overall pitch conversion. In addition to hydrogen, the gas phase contains volatile hydrocarbon product. Ideally, volatile hydrocarbons are removed from the reactor in the gaseous effluent. Recirculation of volatile hydrocarbon product is undesirable because it further decreases the volume available for unconverted pitch, as well as reducing reactor efficiency as hydrocarbon product is continually processed to undesirable lighter ends.

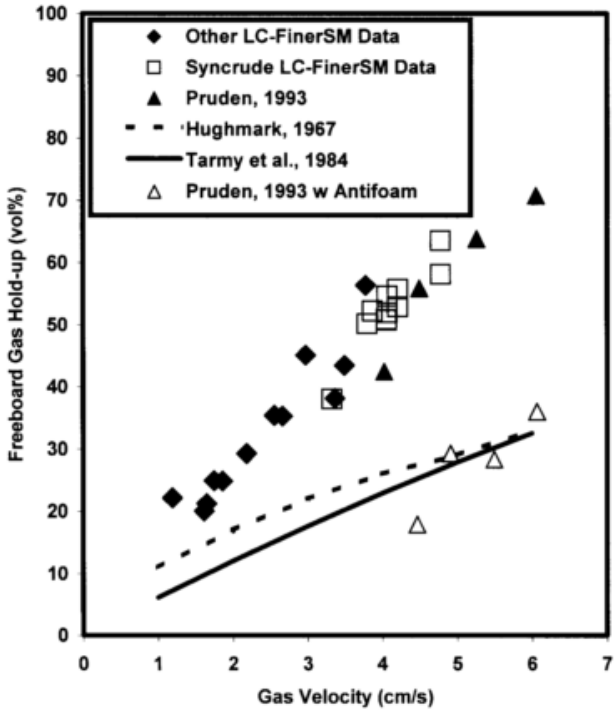

Figure 1.3.1: LC-Finer[SM] gas holdup in comparison to previous estimates (McKnight et al., 2003).

Measurements in the freeboard region and above the recycle pan show gas holdups reaching ~80% which is above the packing limit of spherical bubbles suggesting some type of colloidal flow or foam exist in this region (McKnight et al., 2003). A study by Pruden et al. (1993) using an anti-foam agent in a pilot scale unit provided reduced gas holdup. However, when tested in an industrial scaled unit, no such reduction was observed.

Athabascan bitumen has a significant asphaltenes component of approximately 15% (Dutta et al., 2000). The pitch feedstock for an LC-Finer[SM] has elevated concentrations due to the removal of lighter components at the upstream distillation towers. Asphaltenes are extremely high molecular weight, i.e., n-heptane insoluble, molecules that are known to oligomerize and precipitate from the liquid phase as coke which deposits within, and downstream of, the hydroprocessor (Gawel et al., 2005). To inhibit the rate of asphaltene compound polymerization, thereby reducing the overall rate of its deposition, hydrogenation of free radical hydrocarbons must be promoted. Hydrogenation promotion is achieved through the increased concentration of dissolved hydrogen in the liquid phase. Through the removal of volatile hydrocarbon products from the reactor, the hydrogen partial pressure can be increased, thereby promoting the hydrogenation of free radical hydrocarbons and reducing the rate of asphaltene polymerization and deposition.

Many internal geometries and other technologies have been invented to promote the separation of gas and liquid phases in an ebullated bed reactor (patents US 5624642, US 5443718, US7927404, US 4354852, US 4792391, US 3698876, US 3630687, US 5308476, US 4221653, and US 4886644). However, there exists an absence of current literature concerning the effects of the separator on the fluid dynamics of the ebullated bed reactor and the mechanisms of separation employed by various designs. Current technology has produced

unsatisfactory results, and an improved fundamental understanding of internal gas-liquid separation will provide insight for future technology improvements.

1.4 Fluid Dynamic Studies in Support of Ebullated Bed Hydroprocessors

Numerous works have been published on the theory and modeling of three-phase ebullated beds. An excellent source on this topic is the cornerstone work of Fan (1989). However, modeling and scalability of three-phase ebullated bed reactors continue to be an area of current interest (Martínez et al., 2010). Previously, Safoniuk et al. (1999) proposed a scaling approach based on the dimensionless similitude of a gas-liquid-solid fluidized bed system. Following the Buckingham π theorem, the dimensionless Morton, Eötvös, and Reynolds numbers (Eqn. 1.4.1-1.4.3) were identified along with the solid-liquid phase density ratio (Eqn. 1.4.4) and ratio of gas to superficial liquid velocity (Eqn. 1.4.5). A follow-up investigation to validate this approach found these dimensionless groups to be inadequate to characterize the fluidization behavior of an ebullated bed quantitatively (Macchi et al., 2001). Additional investigations of three-phase fluidized beds, at conditions characteristic of an industrial hydroprocessor, revised the required dimensionless groups to include the Archimedes number (Eqn. 1.4.6) in place of the Morton or Eötvös numbers (Pjontek et al., 2015).

$$\mathrm{Mo} = \frac{g\left(\rho_l - \rho_g\right)\mu_l^4}{\rho_l^2 \sigma^3} \tag{1.4.1}$$

$$\mathrm{Eo} = \frac{g\left(\rho_l - \rho_g\right)d_p^2}{\sigma} \tag{1.4.2}$$

$$\mathrm{Re} = \frac{\rho_l d_p U_l}{\mu_l} \tag{1.4.3}$$

$$\beta_d = \frac{\rho_p}{\rho_l} \tag{1.4.4}$$

$$\beta_U = \frac{U_g}{U_l} \tag{1.4.5}$$

$$\mathrm{Ar} = \frac{\rho_l d_p^3 g(\rho_s - \rho_l)}{\mu_l^2} \qquad 1.4.6$$

A water-nitrogen fluid system with the addition of ethanol (EtOH), acting as a surfactant, was shown to match the dimensionless properties of an industrial ebullated bed hydroprocessor using this dimensionless similitude approach. Further experimental studies investigated the fluidization behavior, and phase holdup estimates of a gas-liquid-solid system using the dimensionless analog water (EtOH)-nitrogen. Pjontek et al. (2015) experimentally correlated phase holdups under an analog fluid system and demonstrated that a modified Richardson and Zaki (1954) correlation was suitable for estimating the gas holdup for an industrial hydroprocessor based on gas and liquid superficial velocities. No significant difference in bubble size characteristics between the catalyst bed and freeboard region was observed at elevated pressure. This finding suggests that the presence of catalyst particles has minimal effect on the gas-liquid fluid dynamics of the system at the expected operational conditions. Table 1.4.1 summarizes the ranges of dimensionless parameters which are considered representative of industrial ebullated bed hydroprocessors.

Table 1.4.1: Summary of dimensionless group values Pjontek et al. (2015)

Dimensionless Group	**Symbol**	**Value**
Gas–liquid superficial velocity ratio	U_g/U_l	0 to 2.0
Solid–liquid density ratio	ρ_s/ρ_l	2.505 and 2.716
Gas-liquid density ratio	ρ_g/ρ_l	0.0015 and 0.0740
Particle–liquid Reynolds number	Re	61 to 450
Particle–liquid Archimedes number	Ar	0.12×10^6 to 2.14×10^6

Parisien (2016) performed gas-liquid studies at elevated pressure and high gas holdup conditions to elucidate the fluid dynamics and bubble characteristics in the freeboard region of a hydroprocessor. Experiments conducted at both low and high pressure demonstrated the suppression of the transition from dispersed bubbly flow to coalesced bubble flow. This has also been observed for a coal liquefaction pilot plant, a similar system in that both are high pressure contaminated systems (Ishibashi et al., 2001).

Although multiple authors have improved the modeling capabilities for industrial ebullated bed hydroprocessors, no current literature exists addressing the discrepancy of current model predictions for phase holdup, liquid residence time, and entrainment of recycled gas. Modeling of the fluid dynamics within an ebullated bed reactor accurately is necessary to estimate conversion and throughput with high confidence.

1.5 Research Objectives and Thesis Structure

The objective of this doctoral thesis is to provide a fluid dynamic model of an industrial ebullated bed reactor which accounts for the effects of the internal recirculation of gas bubbles. The recirculation of the gas phase will be investigated through both numerical and experimental techniques to understand how recycled gas impacts phase holdup and fluid dynamics in the hydroprocessor. A complete fluid dynamic model provides a necessary tool to understand how various operational parameters affect hydroprocessor performance. It also provides the pre-requisite knowledge to improve mass transfer, reaction, and conversion models for a complete understanding of the reactor. This work is part of a larger research project directed at improving the overall efficiency of industrial ebullated bed hydroprocessing reactors. An important outcome of this thesis is that it provides the capability and evaluation tools for use in improving the design of the reactor internal configuration and assessment of

performance impacts of various operational parameters. The scope of the presented work is, therefore:

1. Numerically conduct a parametric analysis on the separation performance of a first generation recycle pan used in an LC-Finer[SM]. Assess the performance impact of typical variations in reactor fluid conditions, and identify an appropriate correlation framework for gas entrainment and model limitations.
2. Address the requirement for an experimentally validated drag correlation. Evaluate drag models for polydisperse bubbly flow in an experimental system with similar fluid conditions to a commercial ebullated bed hydroprocessor. Study individual bubble rise rate within a swarm to improve modeling capabilities and provide confidence in separation performance estimates.
3. Validate a correlation for gas separation efficiency by comparing gas separation performance for various pilot-plant scale separator configurations. Experimental pilot-plant studies are used to validate CFD predictions, and a qualitative evaluation of different generation separators provides future design considerations.
4. Incorporate the gas separation model, drag model, and existing correlations for the fluidized bed region to provide an integrated fluid dynamics model for an industrial ebullated bed reactor.

A preliminary investigation on the separation performance of a common recycle pan geometry using CFD is presented in chapter 2. A parametric analysis of gas separation performance to the operational parameters gas-liquid flow rate, gas holdup, liquid phase recycle fraction, and bubble size was conducted. The sensitivity of results to the selected bubble drag correlation

are highlighted, and the requirement for experimental validation is discussed. Additional investigations on the effects of non-coalescing bubbles (foaming) are also reviewed. Results are presented on a recycle liquid residence timescale, identifying the correlation framework for use in the integrated ebullated bed hydroprocessor fluid dynamics model.

The sensitivity of CFD separation performance estimates presented in Chapter 2 requires an experimental validation of the bubble drag. Chapter 3 examines the effects of drag on individual bubbles in a polydisperse bubble swarm. A previously validated experimental system representative of an industrial ebullated bed hydroprocessor is used to determine the most appropriate correlation for the drag force acting on individual bubbles in a swarm. The drag coefficient for individual bubbles in a swarm at both atmospheric (0.1 MPa) and high pressure (6.5 MPa) are presented and discussed. Results from this study provide the validation for the CFD simulations presented in chapter 4.

In Chapter 4, a comparison of three unique separator configurations at pilot plant scale and operationally relevant conditions provides a verification of the previously proposed correlation framework. Geometries were evaluated experimentally and by CFD simulation at equivalent conditions. A comparison of CFD and experimental results provide confidence in the robustness of the selected CFD approach to predict separation performance among different geometry configurations. Fluid flow structures predicted by CFD are discussed to provide design recommendations for future separator geometries.

Chapter 5 presents an integrated ebullated bed hydroprocessor fluid dynamics model. The fluid dynamic model incorporates gas separation estimates as previously discussed. The assumptions, justifications, and numerical framework are outlined and reviewed. Predictions of gas holdup are compared to previously reported industrial data to assess the ability of the

integrated model to estimate gas holdup. The residence time distributions of the model are compared to the common continuous stirred-tank reactor (CSTR) assumption. An analysis of gas holdup and the ratio of feed to recycled gas is discussed to identify the possible impacts of recycled gas on reactor performance.

Finally, conclusions and recommendations for future research to further improve the modeling capability and design of industrial ebullated bed reactors are discussed in chapter 6.

2 Parametric Analysis of Internal Gas Separation within an Ebullated Bed Reactor

C.D. Lane[1], C.A. McKnight[2], J. Wiens[2], K. Reid[2], A.A. Donaldson[1]

[1] Department of Process Engineering and Applied Science, Dalhousie University, NS, Canada
[2] Syncrude Canada Ltd., AB, Canada

Abstract

Ebullated bed reactors are commonly found within residue hydroprocessors used to convert atmosphere and vacuum tower residue to lighter more valuable products in heavy oil upgrading. These units have historically experienced very high solids-free gas holdups above 30%, displacing heavy feed and limiting product throughput, with significant focus placed on the effects of the internal recycle geometry on column performance. A 3D CFD framework for simulating the gas separation region is presented here, capable of capturing tangential and rotational fluid motion and transient gas separation dynamics. The model is applied to a first-generation recycle cup separator design and is used to explore operational parameters (fluid velocity, bubble size/holdup, recycle fraction, and foam generation) and the choice of momentum coupling strategy on gas entrainment and separation efficiency. The results provide a framework for comparison and evaluation of future designs as well as fundamental insight into the separation dynamics in the freeboard region of this reactor, with efforts ongoing to compare and contrast fundamental operating modes of multiple separator designs.

***This manuscript has been published**: C.D. Lane, C.A. McKnight, J. Wiens, K. Reid, A.A. Donaldson, 2016. Parametric Analysis of Internal Gas Separation within an Ebullated Bed Reactor. Chem. Eng. Res. Des. 105, 44-54.

2.1 Introduction

Ebullated bed hydroprocessors consist of a three phase (gas-liquid-solid) fluidized catalyst bed and internal liquid recycle. Due to the high energy demands of hydroprocessing, the efficient operation of these units is important for cost and emissions reduction to the overall upgrading process. High gas holdup (>30%) within the column has been identified as a limiting factor to the reactor's residue conversion, whereby the excess hydrogen and product vapors displace potential liquid inventory and reduce overall processing capacity (McKnight et al., 2003). Methods and techniques to reduce circulating gas are thus of significant interest, with previous work exploring strategies to reduce gas holdup through operational and geometric modifications of the industrial and analogous cold-flow units (Ancheyta, 2013; Buttke and Frey, 1989; Grace and Zhu, 1992; Martínez et al., 2010; McKnight et al., 2003; Pjontek et al., 2014). While fundamental theory for gravity-based separators is thought to roughly describe the separation occurring within the system, the mechanisms governing gas-liquid separation within the ebullated bed are known to be complicated by foam formation, geometric deviation from a traditional "horizontal" separator, internal recycle fraction, and other operational properties. As such, progressive generations of separators constructed for the ebullated bed system have been based on extensive empirical testing and cold-flow optimizations. A better understanding of the fluid dynamic fundamentals for these units could identify the performance limit of current designs and lead to opportunities for reduced gas holdup within the column through the development of next-generation designs.

Previous attempts to reduce gas hold-up originally led to the addition of a recycle pan at the top of the internal recycle line within the ebullated bed reactor (Figure 2.1.1). This design was implemented in an attempt to enhance gas disengagement above the catalyst bed in the freeboard region of the reactor. Upon further testing, this first generation recycle pan was

found to result in a stable, gas-rich effervescent foam region at the top of the reactor which extended down into the recycle line, increasing gas re-entrainment and gas holdup (McKnight, 2008). Industrial designs have since evolved to next generation separators capable of reducing the total gas holdup by a few percent, corresponding to significant increases in total liquid feed production capacities.

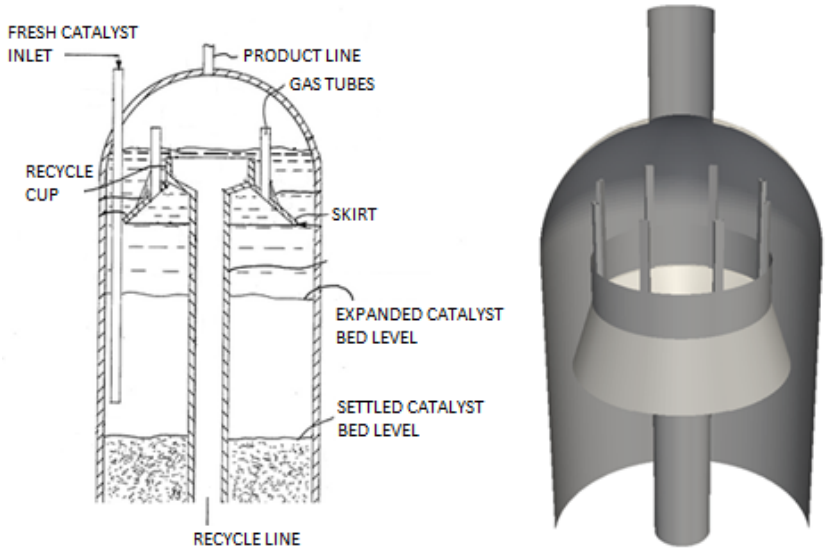

Figure 2.1.1: Left – Schematic of an ebullated bed freeboard region modified from Buttke and Frey (1989). Right – CFD Mesh rendering sectioned to illustrate the internal structure. The mesh is modeled as a 45-degree wedge geometry and is visualized by rotating the wedge about the vertical axis.

2.2 Computational Methods and Models

The recycle pan of the ebullated bed reactor was modeled using an Euler-Euler framework in OpenFOAM®-2.2.0 modified to dynamically set boundary pressure conditions to meet a target liquid recycle fraction. The computational domain was based on the unit description by McKnight et al. (2003) representative of the cold-flow unit approximately built to a 1:3 scale of the industrial column (~0.6 m radius). The cold-flow unit is a Kerosene-Nitrogen system operating at 138 kPa and 20°C, while the industrial unit operates at significantly higher

temperatures and pressures. It is assumed no solids from the catalyst bed region of the reactor enter the separation region and therefore the system is approximated as gas-liquid. These fluids have been shown to be good analogs for the operating conditions of the industrial unit (Macchi et al., 2001). A Kerosene-Nitrogen system allows for a smaller mean bubble size (~1 mm), and higher gas holdup by better approximating the physical properties of the industrial fluids. This provides some confidence in the extension of hydrodynamic studies performed at the cold-flow facility to operational conditions. The resulting physical property values applied in this study are summarized in Table 2.2.1.

Table 2.2.1: Physical properties employed within this study, representative of cold-flow conditions in a Kerosene-Nitrogen system

Parameter	**Symbol**	**Value**	**Units**
Liquid density	ρ_l	819	$kg \cdot m^{-3}$
Gas density	ρ_g	1.61	$kg \cdot m^{-3}$
Liquid kinematic viscosity	ν_l	4.0×10^{-5}	$m^2 \cdot s^{-1}$
Gas kinematic viscosity	ν_g	1.4×10^{-5}	$m^2 \cdot s^{-1}$
Bubble diameter	d_b	0.001	m
Surface tension	σ	0.026	$N \cdot m^{-1}$

Figure 2.1.1 illustrates the freeboard region of an ebullated-bed reactor (left) and the simulated geometry (right) consisting of a cup, skirt, and 8 riser pipes. The skirt's principle objective is to capture gas and divert it away from the recycle pan to the top of the unit though the riser pipes. The recycle pan draws liquid to the bottom of the unit to be recycled, ideally allowing gas bubbles to disengage and rise up to the product line. This geometry was modeled as a 45° wedge with symmetric boundary conditions about the central axis and rotated cyclic boundaries on surfaces through which tangential motion would occur. The risers are located at an angle of 22.5° within the wedge to mitigate asymmetric effects near the boundary surfaces. The inlet has flow entering from the annulus of the unit's freeboard region. The

outlets, which will be referred to as the product line (top) and recycle line (bottom), remove fluid from the vessel and recycle fluid to the catalyst bed respectively. Both the product and recycle lines were assumed to be equal in diameter and have approximately $1/20^{th}$ the cross-sectional area of the annulus. The velocity for both phases is fixed at the inlet with no-slip velocity between phases at the boundary. Although this inlet condition is not strictly true (i.e. u_g typically > u_l), the terminal slip velocity between phases was achieved prior to the phases entering the region of active separation. The outlet flow ratios for the liquid phase were determined by the recycle fraction parameter, $\mathcal{R}$ (Eqn. 2.2.1).

$$\mathcal{R} \equiv \frac{\dot{m}_{l,recycle}}{\dot{m}_{l,inlet}} \qquad 2.2.1$$

Here, $\dot{m}_{l,r}$ and $\dot{m}_{l,i}$ are the liquid mass flow rates at the recycle and inlet boundaries, respectively. The recycle fraction is the ratio of feed liquid that is recycled back into the column through the central recycle, set within an industrial unit by the rotation rate of a pump at the base of the liquid recycle. This was controlled within OpenFOAM® by modifying the solver to use a proportional control algorithm to set the pressure difference between the product and recycle lines. Controlling the pressure differential, as opposed to enforcing a liquid mass flow rate, has the benefit of allowing for the development of non-uniform and more representative velocity profiles near the boundary which still meet the mass flow rate constraint. Tuning parameters were selected which result in a short response time (<< 1 s simulated time) relative to the time scale of the separation process. The expression for the recycle line pressure is given by equation 2.2.2, where $P_{recycle}$ is the relative pressure of the recycle line boundary to the product line boundary, m_i is the mass flow rate for boundary i, and R is the specified recycle fraction 0.8 for the base case. The value of $P_{recycle}$ was bound

by 100 and 20000 to allow for simulation stability over the initial pressure field resolution. The relaxation factor of 0.05 was selected to provide adequate response time without significant overshoot.

$$P_{recycle,t+1} = min\left[max\left[P_{recycle,t} + 0.05P_{recycle,t}\,\frac{\left(\frac{m_{recycle,t}}{m_{inlet,t}} - \mathcal{R}\right)}{\mathcal{R}}, 100\right], 20000\right] \quad 2.2.2$$

The OpenFOAM® solver *twoPhaseEulerFoam* was modified for use in this work, utilizing a two-fluid approach for solving the gas and liquid phase flows, where the continuity and momentum equations for each phase are:

$$\frac{\partial}{\partial t}(\varepsilon_i\rho_i) + \nabla\cdot(\varepsilon_i\rho_i u_i) = 0, \quad \sum \varepsilon_i = 1 \quad 2.2.3$$

$$\frac{\partial}{\partial t}(\varepsilon_i\rho_i u_i) + \nabla\cdot(\varepsilon_i\rho_i u_i u_i) + \nabla\cdot(\varepsilon_i\tau) + \nabla\cdot(\varepsilon_i R) = -\varepsilon_i\nabla P + \varepsilon_i\rho_i g + M_T \quad 2.2.4$$

$$M_T = M_{drag} + M_{VM} + M_{lift} \quad 2.2.5$$

In these equations, ε is the phase fraction, ρ is the phase density, u is the velocity vector, τ is the laminar stress tensor, R the Reynolds stress tensor, M_T is the momentum exchange term between phases, and i denotes the phase. Momentum coupling terms lift, virtual mass, and drag are expressed within the solver as:

$$M_{lift} = \varepsilon_g\varepsilon_l(\varepsilon_l C_{lift,g}\rho_l + \varepsilon_g C_{lift,l}\rho_g)u_r \times \nabla \times u_l \quad 2.2.6$$

$$M_{VM} = \varepsilon_g\varepsilon_l C_{VM}\rho_l\left(\frac{\partial u_l}{\partial t} + u_l\cdot\nabla u_l - \frac{\partial u_g}{\partial t} + u_g\cdot\nabla u_g\right) \quad 2.2.7$$

$$M_{drag} = \frac{3}{4}\varepsilon_l\varepsilon_g\left(\frac{\varepsilon_l C_D\rho_l}{d_b}\right)|u_r|u_r \quad 2.2.8$$

The Saffman lift force (Saffman, 1956) model was neglected ($C_{lift} = 0$) and a virtual mass coefficient (C_{VM}) of 0.5 was used (Auton, 1981). Other proposed coupling, including the Basset history force and turbulent dispersion force, were also neglected based on the geometric scale and Reynolds numbers on the order of ~600 for the annular inlet flow. Drag was of particular interest due to its importance in separation dynamics for this system and the variety of drag models previously applied to high gas fraction bubble column simulations. The fluid coupling drag term is aggregated to a phase average from the drag experienced by individual bubbles 2.2.8, where C_D is the drag coefficient for a single bubble.

The four drag models compared within this work are based on the commonly applied Schiller and Naumann (1978) model, which expands on Stoke's law to describe the drag experienced by a rigid sphere as a function of its Reynolds number:

$$C_D = \begin{cases} \frac{24}{\mathrm{Re}}(1 + 0.15\mathrm{Re}^{0.687}) & Re \leq 1000 \\ 0.44 & Re > 1000 \end{cases} \quad 2.2.9$$

Tomiyama (1998b) proposed two closures (Eqns. 2.2.10 and 2.2.11), for pure and contaminated systems. While the Schiller-Naumann model is appropriate for rigid spheres, the Tomiyama model accounts for the deformation and surface slip of fluid particles. Effects of bubble deformation are incorporated with the addition of an Eötvös number based term.

$$C_D = max\left[min\left[\frac{16}{\mathrm{Re}}(1 + 0.15\mathrm{Re}^{0.687}), \frac{48}{\mathrm{Re}}\right], \frac{8}{3}\frac{\mathrm{Eo}}{\mathrm{Eo} + 4}\right] \quad 2.2.10$$

$$C_D = max\left[\frac{24}{\mathrm{Re}}(1 + 0.15\mathrm{Re}^{0.687}), \frac{8}{3}\frac{\mathrm{Eo}}{\mathrm{Eo} + 4}\right] \quad 2.2.11$$

While a previous estimate of the Eötvös number at industrial conditions has been 1.4 for a bubble diameter of 1 mm (Grace and Zhu, 1992), this value may vary considerably as the

surface tension is not a value known with confidence. At gas fractions greater than ~0.05 a correction should be used to account for the effects of a swarm of bubbles (Michaelides, 2006). Many authors have proposed correlations to account for this and are of a similar form to $\left(1-\varepsilon_g\right)^n$ where n is the Richardson-Zaki exponent (Bridge et al., 1964a; Davidson and Harrison, 1966a; Griffith and Wallis, 1961a; Marrucci, 1965b), a summary of these is provided by Simonnet et al. (2007). The correction factor used in this study was proposed by Lockett and Kirkpatrick (1975a) (Eqn. 2.2.12) and was applied to the contaminated Tomiyama closure (Eqn. 2.2.11).

$$\frac{C_D}{C_{D,\infty}(1-\alpha)} = [(1-\alpha)^{1.39}(1+2.55\alpha^3)]^{-2} \qquad 2.2.12$$

To gain some insight into the possible implications of a non-coalescing foaming gas, two additional data sets were collected with a gas phase packing limiter of 0.6 and 0.8. The Euler-Euler solver allows for phase inversion and does not track phase boundaries. This is most representative of a perfectly coalescing system, where there is no hindrance to bubble movement as the phase fraction surpasses the spherical particle packing limit. It is, therefore, useful to examine the other extreme, where bubbles are non-coalescing and due to their low Eötvös number, can be considered spherical in shape. To simulate this, packing limiters of 0.6 and 0.8, were incorporated.

The inclusion of a packing limiter can be conceptualized as approximating the bubbles as rigid spheres with the density of the gas phase. The solids pressure term is given by equation 2.2.13. Here Θ_g is the granular temperature of the bubbles, $g_{0,gg}$ is the radial distribution function and e_{gg} is the restitution coefficient equal to 0.9.

$$P = \alpha\rho_g\Theta_g + 2\rho_g(1+e_{gg})\alpha^2 g_{0,gg}\Theta_g \quad 2.2.13$$

This pressure term represents the contribution of collisions between bubbles as they reach their packing limit. This term was included only for a small subset of trials to estimate a worst case scenario of separation where the system could be considered perfectly non-coalescing. A detailed explanation of its implementation is given by Van Wachem (2000). With the computational framework described here, a single simulation of 300 seconds takes approximately 50 hours to run on eight cores of an Intel® Core™ i7 Xenon processor (3.3 GHz) running the Ubuntu 12.10 operating system. Mesh and Courant number independence studies were conducted for Courant numbers of 0.05, 0.075, and 0.1 and meshes with approximately 65000, 150000, and 300000 cells, with the volume average gas phase fraction tracked as an indicator of mesh independence (Figure 2.2.1). Volume average gas holdup is calculated by summation of cell averaged gas holdup over the simulation domain. It was found that a Courant number of 0.1 and cell count of 65 000 was sufficient and was used for all cases. The maximum Courant number could not be increased past 0.1 without instabilities resulting from the implemented proportional control algorithm for setting the liquid recycle fraction. The simulation times were also deemed acceptable for this study, and so lower mesh refinement levels were not explored. Additional information on the numerical methods and CFD mesh used in this study can be found in appendix A.

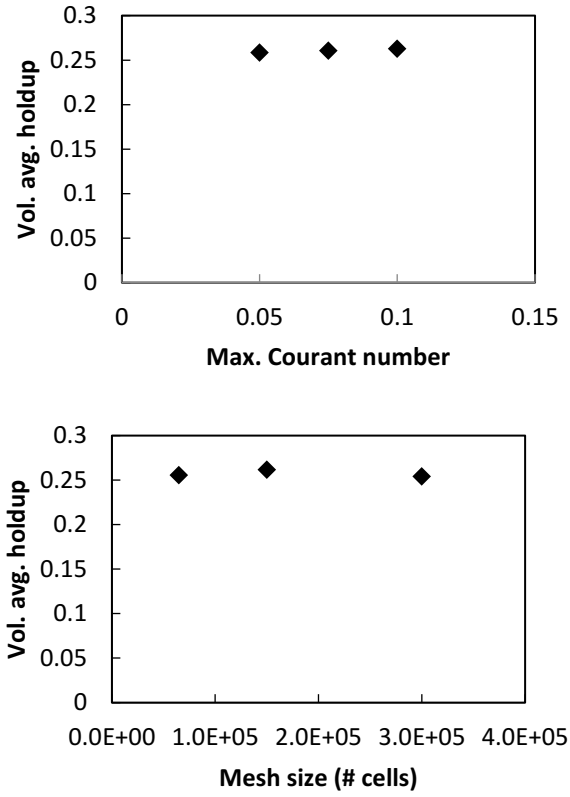

Figure 2.2.1: Left - Solution variance for Courant numbers 0.05, 0.075, and 0.1 plotted against volume average gas phase fraction. A maximum Courant number of 0.1 is required to provide good control of the pressure feedback control loop. Right - Solution variance for mesh cell refinements of 65 000, 150 000, and 300 000 cells plotted against volume average gas phase fraction.

2.3 Results and Discussion

To define the bounds of a parametric study on the effects of combined inlet phase velocity, liquid recycle fraction, inlet gas hold-up and bubble diameter, a common base condition was chosen from representative conditions for the cold-flow unit. The base condition for these parameters were u_{inlet}= 2.66 cm·s^{-1}, $\varepsilon_{g,inlet}$= 0.3, and $\mathcal{R}$ = 0.8, and a bubble diameter of 1.0 mm. The Schiller-Naumann model was used as the base drag correlation due to its prevalence as the *de facto* drag correlation in bubble-column simulations (Gupta and Roy, 2013; Pang and Wei, 2011; Tabib et al., 2008).

To facilitate the comparison of various effects on the disengagement process, a separation effectiveness parameter was defined. Separation effectiveness (Eqn. 2.3.1) gives a ratio of the amount of gas removed to the liquid phase recycle fraction.

$$\eta = 1 - \frac{\dot{m}_{g,recycle}/\dot{m}_{g,inlet}}{\mathcal{R}} \qquad 2.3.1$$

For a case with no separation, the phase ratios at the mesh inlet are equivalent to the liquid-phase flow rate ratios at both outlets, or $\dot{m}_{g,recycle}/\dot{m}_{g,inlet} \rightarrow \dot{m}_{l,recycle}/\dot{m}_{l,inlet} \rightarrow \mathcal{R}$. This would give a separation effectiveness of $\eta = 1 - \mathcal{R}/\mathcal{R} = 0$. As the separation process approaches an 'ideal' process where all gas is removed though the product line $\dot{m}_{g,recycle}/\dot{m}_{g,inlet} \rightarrow 0$ resulting in $\eta = 1 - 0/\mathcal{R} = 1$.

Within these simulations, the inlet conditions were held constant as the column reached steady state. The time-averaged phase distribution and liquid phase streamlines given by the simulation at the base condition are illustrated in Figure 2.3.1. These values were time averaged values from t = 200 s to t = 300 s. The phase distribution shows a high gas holdup region at the apex of the vessel and under the skirt, as was previously reported by McKnight et al. (2003). In these simulations, the vessel is originally assumed full of liquid and is brought to steady state conditions following a step change in inlet gas fraction. The system dynamic response to this inlet gas fraction step change from 0 to 0.3 is illustrated in Figure 2.3.2. Under these conditions, the system reaches steady state after approximately 150 seconds. For this simulation, the time averaged product line gas flow rate is 4.5 $l \cdot s^{-1}$ while the recycle line is 4.1 $l \cdot s^{-1}$ (inlet volumetric flow rate is 8.6 $l \cdot s^{-1}$). Figure 2.3.3 illustrates the development of these high gas regions after a step increase of the inlet gas fraction from 0 to 0.3. Although the gas fraction is high in this region, the product line flow rate is significantly lower than that of the

recycle line. As a consequence, the gas mass flow rates are not significantly different between these locations (Figure 2.3.2).

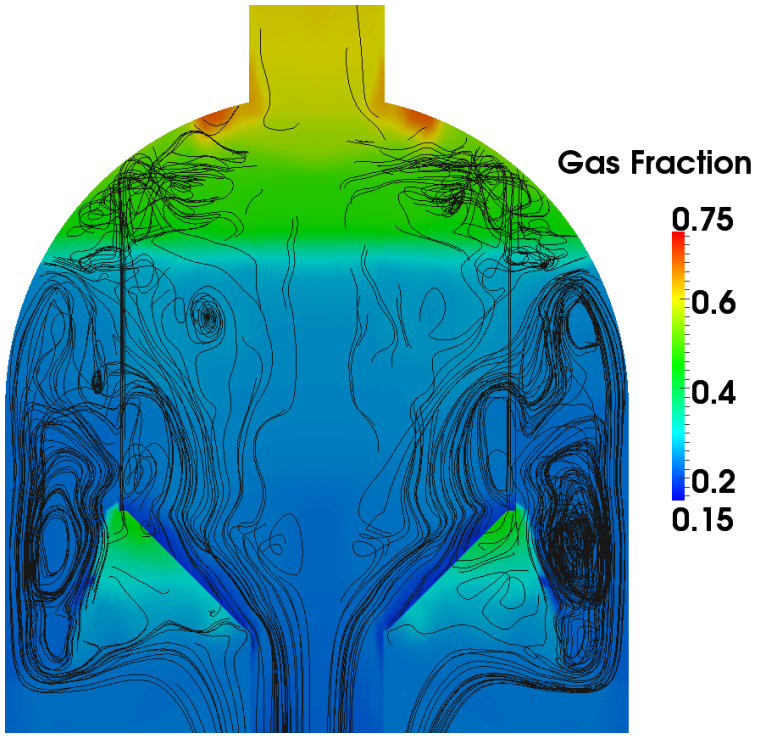

Figure 2.3.1: Phase fraction and liquid phase flow streamlines for the base simulation case u_{inlet}= 2.66 cm·s^{-1}, $\varepsilon_{g,inlet}$= 0.3, and $\mathcal{R}$ = 0.8

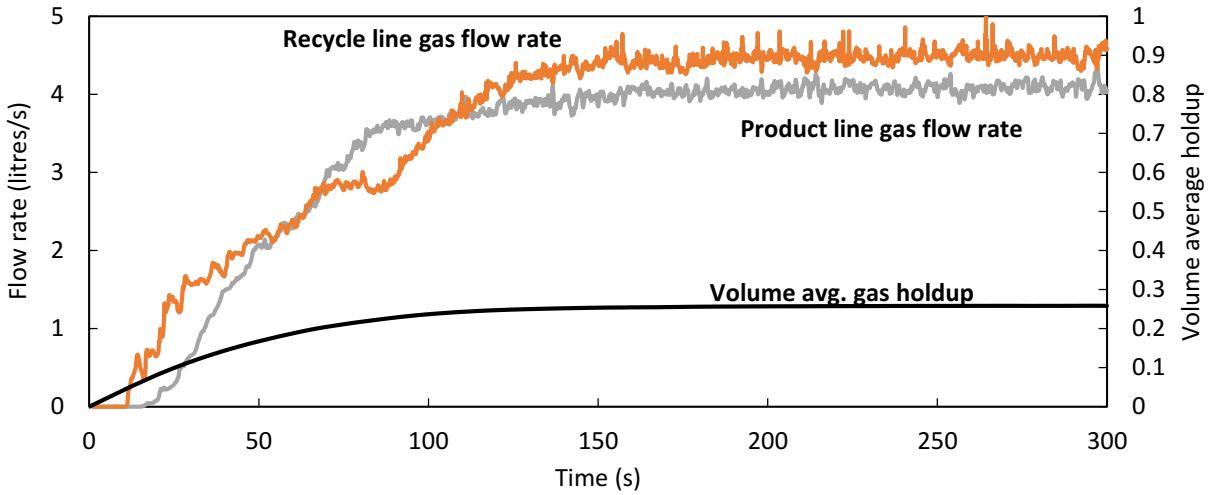

Figure 2.3.2: Time response of gas flow rates at both outlets and global gas phase fraction to a step change in gas fraction at the inlet. The system reaches steady state after approximately 150 seconds. The volume average gas holdup at steady-state is less than the inlet value because the inlet condition assumes no-slip between phases.

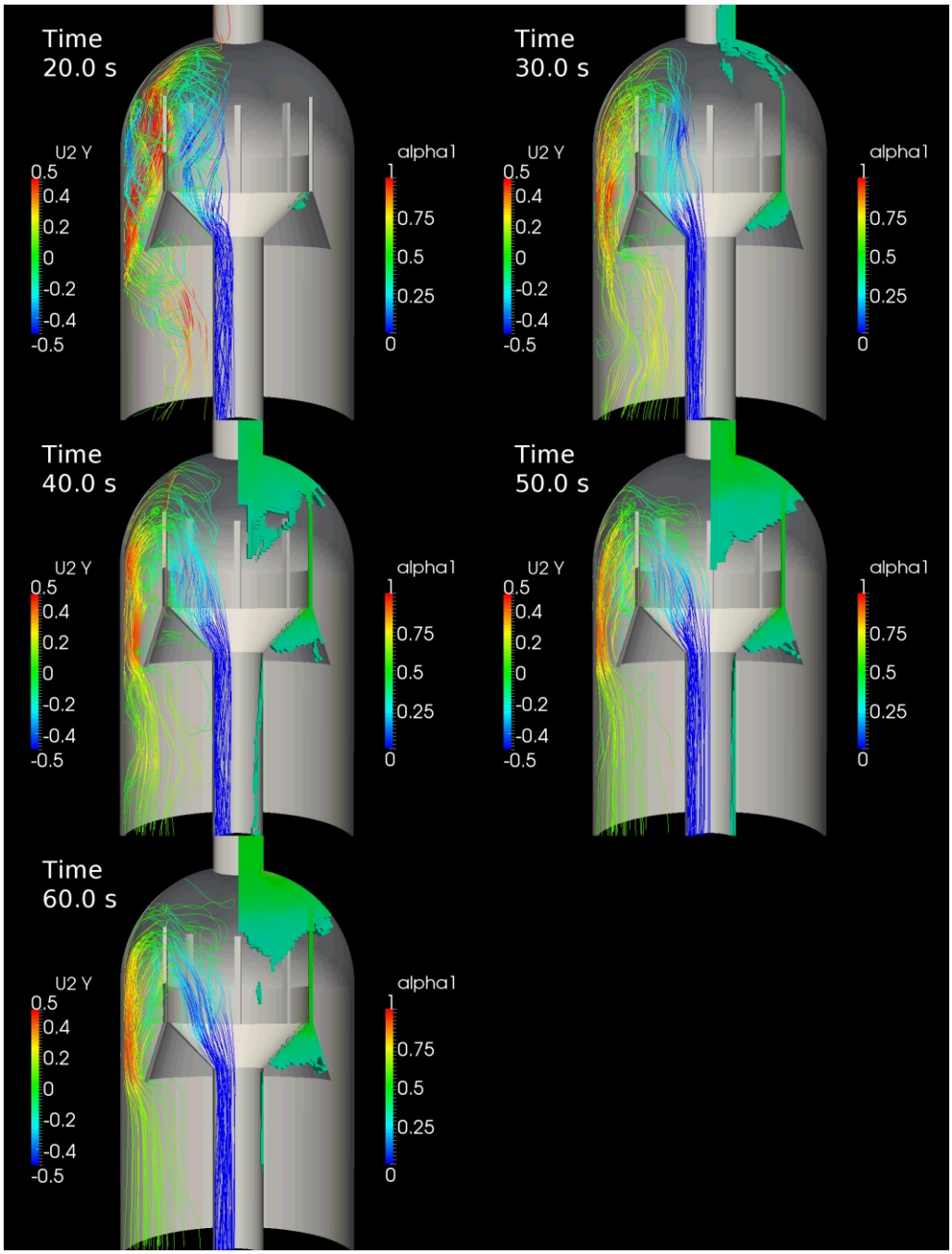

Figure 2.3.3: Rendering of the results for the base condition after a step increase in inlet gas fraction from 0 to 0.3. On the left of the unit are streamlines depicting liquid phase flow path and velocity. On the right of the unit are cells containing a gas fraction greater than 0.3 (i.e. greater than the inlet).

General separator performance was initially explored through modifications to the net processing rates by adjusting the combined inlet phase velocities to values of 0.33, 0.66, 1.33, 2.66, 4.00, and 5.33 cm/s. Figure 2.3.4 illustrates the recycle line gas holdup and separation

efficiency as a function of the combined phase inlet velocity. A reduction in separation effectiveness at increased fluid velocities was expected since the residence time in the separation region decreases. Given the lack of geometry-induced tangential flow within the recycle pan design, separation dynamics of this system are also primarily buoyancy driven, with higher velocities resulting in increased entrainment of bubbles as the liquid phase velocity in the recycle cup exceeds the terminal rise velocity. Although gas disengagement is significant at lower fluid velocities (< 2 $cm \cdot s^{-1}$), the product line holdup is about half (48%) of the inlet gas mass flow rate at the base condition (2.66 $cm \cdot s^{-1}$) with a liquid recycle fraction of 0.8. This gives a separation effectiveness of $\eta = 0.41$.

From analysis of the streamlines and downward velocities in the recycle cup, it was determined that the restricted cross-sectional area of the recycle line itself is not expected to noticeably affect separation effectiveness as the downward liquid fluid velocity within this region is well beyond the terminal velocity of the bubbles. Separation effectiveness is, however, dependent on the recycle pan area and geometry since it forms part of the active separation region where bubbles may still disengage, depending on the liquid processing rates.

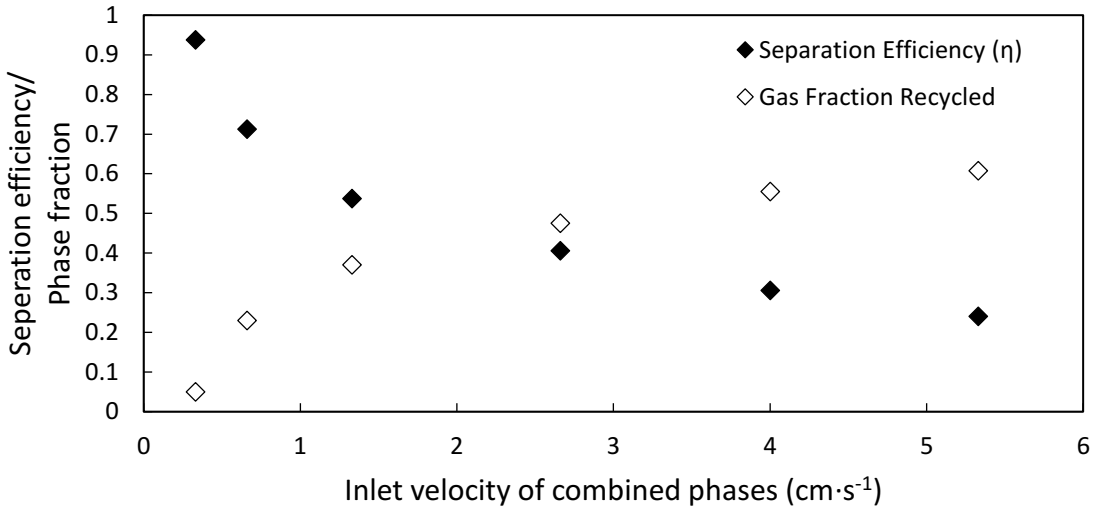

Figure 2.3.4: Effect of inlet velocity of combined phases in the range of 0.33 cm·s^{-1} to 5.33 cm·s^{-1} on gas phase disengagement ($\mathcal{R}$ = 0.8).

2.3.1 Effects of Recycle Ratio and Foam Packing Limit

The recycle ratio determines the ratio of outflows between the product and recycle lines for the liquid phase, and is controlled indirectly within an industrial unit by the rotation rate of the internal recirculation pump which is adjusted to maintain expanded bed conditions. The base condition for these simulations was chosen such that 80% of the liquid phase returned in the recycle line. This is consistent with cold-flow and industrial conditions, where some liquid is removed with the vapor products in the product line. Other recycle fractions of 50%, 60%, 70%, and 90% were used to assess the changes in bubble entrainment due to relative liquid recycle flow rate (Figure 2.3.5). At high recycle ratios, the gas entrainment increases due to greater liquid phase velocities within the recycle pan, increasing gas re-entrainment which displaces liquid phase volume leading to further increases in liquid phase fluid velocity needed to achieve the required recycle fraction. Instabilities would be expected as the system requires greater separation than is achievable to sustain the highest of recycle ratios.

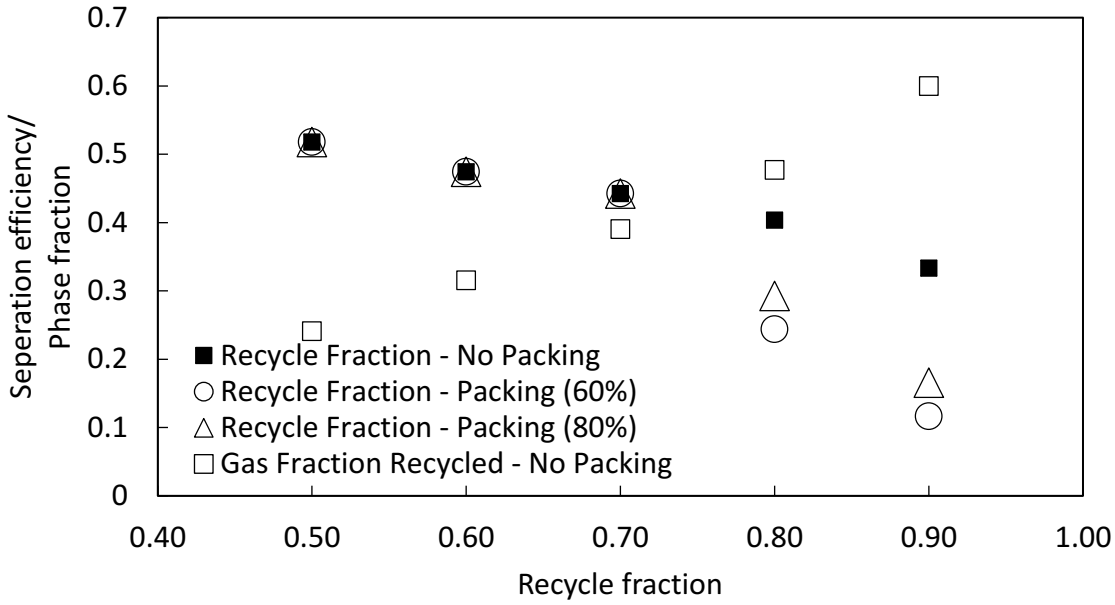

Figure 2.3.5: Effect of recycle fractions 0.5-0.9 on gas phase separation and comparison of packing limited to non-limited cases. Under some conditions gas fraction reaches a critical value at the product line and this region expands downward to the recycle line.

Previous empirical evidence suggests that the gas holdup in the top of the recycle pan approaches 80% (McKnight et al., 2003) due to the formation of a wet foam structure. To explore the impact of a foam structure on separation, a packing limiter was included with maximum packing for bubbles at both 60% and 80% by volume (Figure 2.3.5 and Figure 2.3.6). A 0.6 packing limit represents a random spherical bubble packing which can vary from 0.59-0.64 for a single diameter. This would be indicative of the worst case for the formation of slow-coalescing foam where bubbles cluster as spheres and no coalescence or film drainage occurs. Assuming a foaming system with some degree of coalescence, a 0.8 packing limit could be used to represent a wet foam. Although this limiter does not describe foam mechanics, it serves to demonstrate potential variations in column behavior between a foaming and non-foaming system. For cases where the inclusion of a packing limiter causes growth of the gas region at the limited value, the model is insufficient and requires methods

to deal with foam mechanics where phase fraction exceeds the range of applicability for sphere approximations.

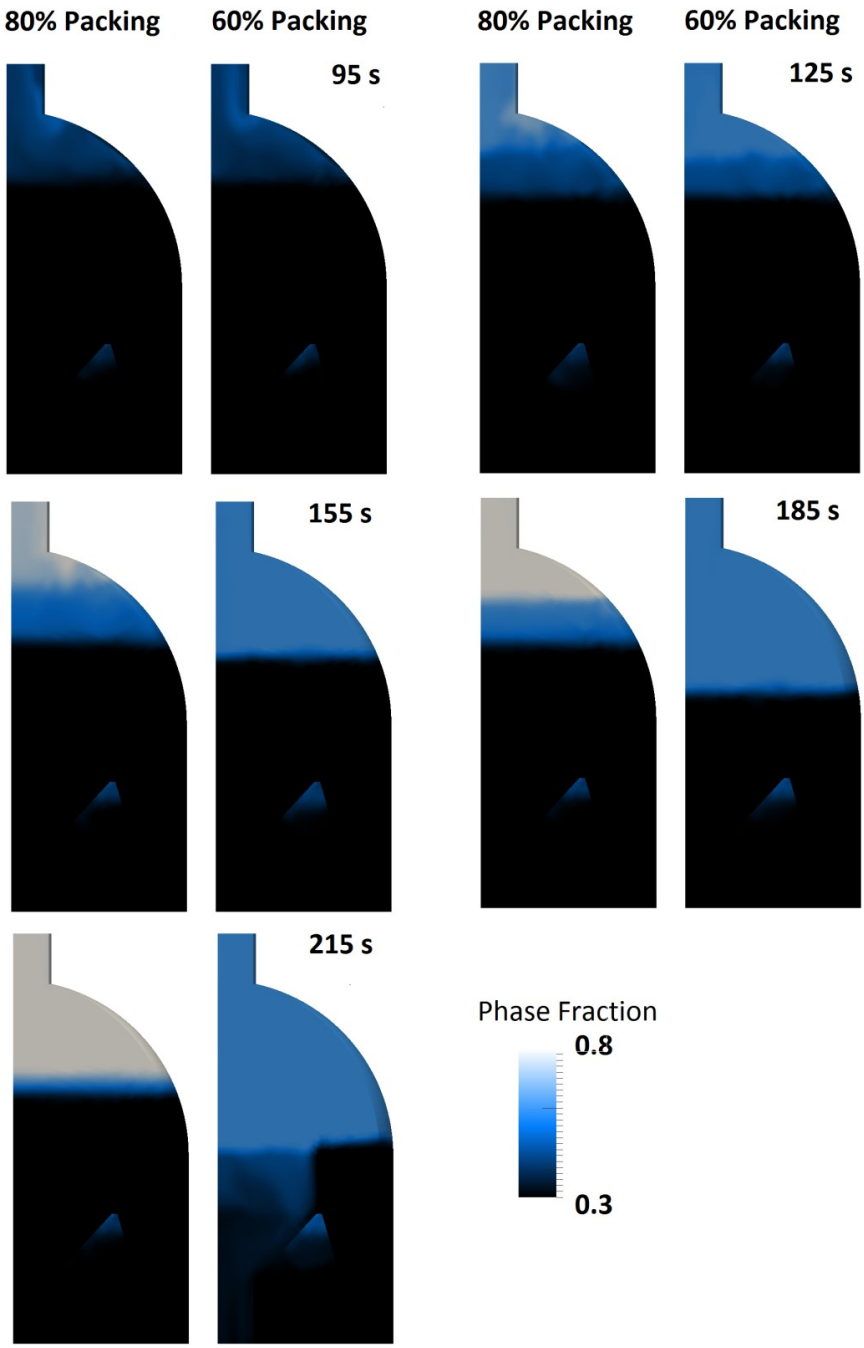

Figure 2.3.6: Development of gas region due to packing limiters of 0.6 and 0.8 for a recycle fraction of 0.9. The region of high gas fraction forms at the product line outlet and expands down into the separation region, eventually into the recycle cup, and is entrained into the recycle line.

For a packing density of 0.6, the maximum gas fraction is achieved in the product line at a recycle fraction of 0.8, whereas this is not the case for a packing density of 0.8. Figure 2.3.6 illustrates the effects of the packing limiters on the growth of the gas-rich region toward the recycle line. It is worthwhile noting that both of these simulations do not reach a stable steady state for the indicated recycle fraction of 0.9 as the gas accumulation within the recycle cup eventually prevents sufficient liquid recycle resulting in an inability for the simulation to reach a steady state. For the sphere packing case (60%), the solution was unstable at recycle ratios above 0.7, which is why there are no steady-state data points in Figure 2.3.5 for these higher recycle ratios.

At lower recycle fractions no noticeable difference in separation efficiency is observed, primarily due to the gas fraction in the product line never reaching the packing limit. As the gas fraction reaches the packing limiter, the gas phase flow rate from the product line becomes dependant on the liquid flow rate. When the net liquid flow rate is 0 at the product line outlet, the maximum gas flow rate could be estimated to have an upper bound of 60% of the product boundary's cross-sectional area multiplied by the terminal slip velocity of the gas. However, as liquid flow rate increases, so does the gas phase flow rate, maintaining the upper bound of 60% of the area at terminal slip velocity plus local liquid vertical velocity. This mass transport limitation within the current computational model is the cause of the growth of a high gas-holdup region at the top of the geometry, which eventually extends into the recycle line. There are obvious concerns over this method of describing the "foam" dynamics within the top of the column, as the drag models used to describe momentum transfer between phases and relative velocities would have limited applicability at these high gas fractions. The behavior observed is, however, in-line with experimental observations within the cold-flow unit, and offers qualitative visualization of how foaming affects the column's operation.

In a study by Guitian and Joseph (1998), foam growth was observed under conditions characteristic of the commercial CANMET reactor. While not of direct relevance to the foaming behavior expected within this system, they noted that the critical condition for foam presence could be predicted using a linear correlation which has been rearranged for clarity in equation 2.3.2:

$$a = U_g - bU_L \qquad 2.3.2$$

where U_g and U_L are gas and liquid superficial velocities respectively, and *a* and *b* are fitted parameters. This observation agrees with the simulation results in that both predict foam generation and growth when the ratio of phase flow rates surpasses a critical value (Figure 2.3.5). For the simulated separation process, this value is first reached near the product line outlet and is dependent on the disengagement of gas, as well as the liquid recycle fraction. This suggests that maintaining the phase ratios below a critical foaming value would be necessary to avoid foam growth. In the foam-affected region, separation is limited by foam generation and structure, where high recycle ratios will result in foam re-entrainment by breaking off "clumps" of foam (as seen in Figure 2.3.3, time = 60 s). Under these conditions, either a method of collapsing the foam internally or increasing the product line draw and using an external recycle should be investigated.

2.3.2 Effects of Column Gas Holdup

Inlet phase gas fractions of 5%, 10%, 20%, 30%, 40% and 50% were used to evaluate the relative impact on separation (Figure 2.3.7). The primary factor affecting the separation efficiency as gas fractions are increased was the displacement of liquid volume which reduced the overall liquid phase momentum. As a result, more gas entrainment occurred at lower inlet gas phase fractions. This effect was primarily due to a constant overall phase velocity being

used, where liquid volumetric flow rate increases to maintain constant total flow as the gas fraction is reduced, generating higher velocities in the recycle cup and more gas entrainment at equivalent recycle ratios.

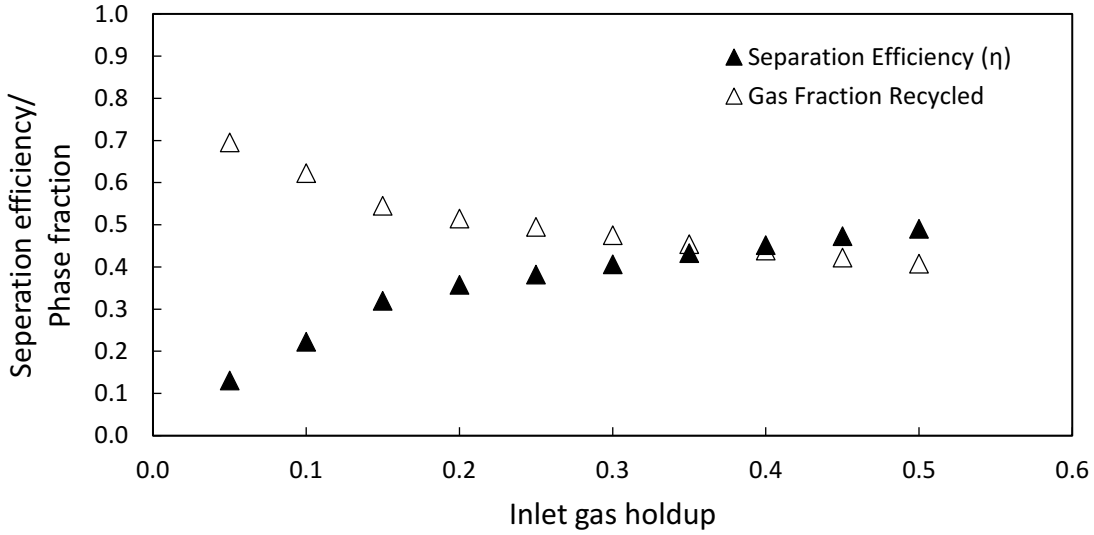

Figure 2.3.7: Effect of inlet gas fraction in the range of 0.05 to 0.5 on phase separation. These simulations were carried out at constant combine phase inlet velocity. As gas fraction decreases, liquid flow rate increases reducing separation effectiveness.

2.3.3 Effects of Bubble Diameter and Drag Closure

For two-phase gas-liquid systems where gas is the dispersed phase, the bubble diameter is a critical parameter for modeling fluid dynamic behaviors and phase separation. The relative velocity between phases is primarily driven by the buoyancy and drag force balances. With the assumption of incompressible fluids and constant densities, this force balance reduces to a dependency on the diameter of the dispersed bubbles through the volume, projected area, and drag coefficient. Figure 2.3.8 illustrates the ratio of $\dot{m}_{g,r}/\dot{m}_{g,i}$ for various drag models and bubble diameters of 0.1 mm, 0.5 mm, 1.0 m, 1.5 mm, 2.0 mm, 2.5 mm, and 3.0 mm. This range of bubble sizes was determined to be representative of the range of sizes expected in the industrial unit (Pjontek et al., 2014), while the drag models span those typically used in

bubble-column systems with and without the need for swarm corrections. For a given bubble diameter, each drag closure was applied to determine the variance in predictions.

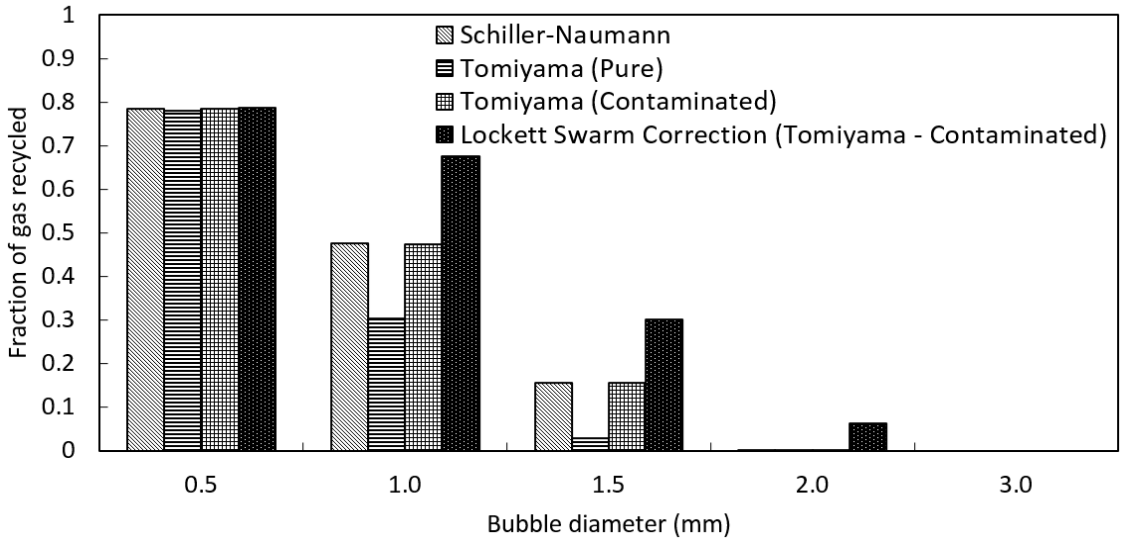

Figure 2.3.8: Effect of bubble diameter and drag model on gas fraction recycled for base simulation conditions. Note that a recycled fraction of 0.8 corresponds to no separation, while a fraction of 0 corresponds to complete separation.

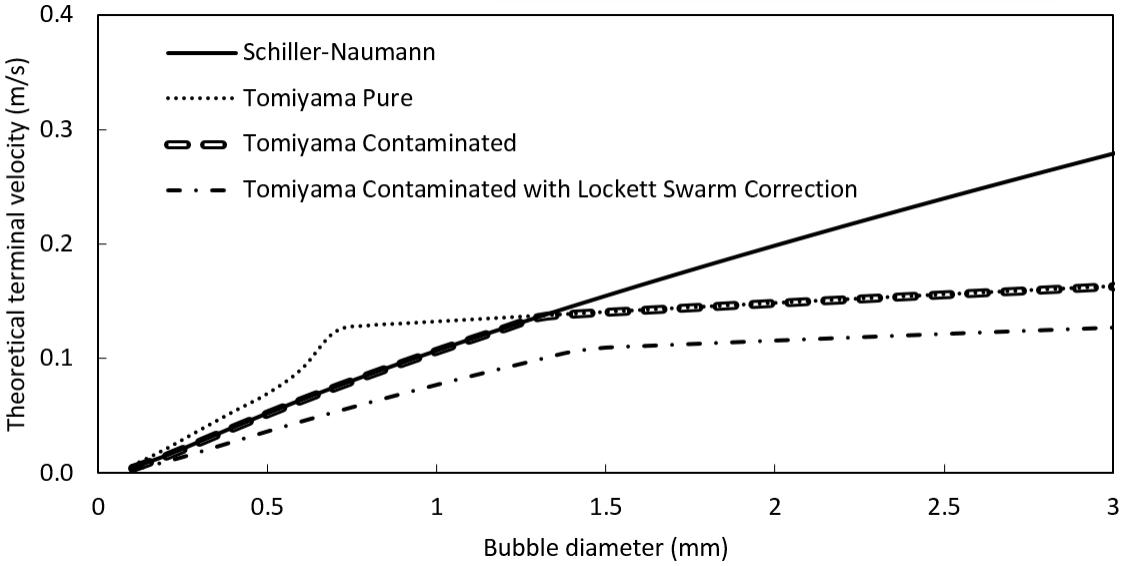

Figure 2.3.9: Theoretical terminal velocity comparison between drag correlations.

As can be observed from Figure 2.3.8, the effects of the drag closure model on separation for this unit are most pronounced around ~1 mm. The theoretical terminal velocities predicted

by the drag correlations used are depicted in Figure 2.3.9, with the greatest variation also occurring in the 0.5 to 1.5 mm bubble diameter range.

Within the small bubble region where complete entrainment occurs (i.e. <0.5 mm diameter), these bubbles would be entrained indefinitely unless absorbed by fresh feed into the column within the distributor and bed region. One hypothesis for the high gas fraction present within these industrial units is the prevalence of microbubbles formed from the high-shear conditions present in the recirculation pump and distributor. In the large bubble region no gas is entrained, and provided a non-foaming system is present, all gas will be removed in the product line. Given the elevated gas densities and low surface tensions present within these units and the significant bubble size reduction which occurs within the solid bed, the likelihood of these larger bubbles being present is minimal.

Separation of bubbles within the intermediate size region is highly dependent on the proper selection of a drag closure models. While many drag correlations exist, they are often derived under limited conditions and caution must be exercised in extending them to high gas fraction regions encountered within this type of industrial unit. Without correcting for swarm effects, many drag models including those chosen for this study are valid only up to phase fractions around 10%. Swarm corrections similar to the Lockett model extend this range of applicability as far as 30% under ideal conditions, but are not able to resolve momentum coupling at higher phase fractions or when packing becomes an issue. For these reasons, work is currently progressing to experimentally validate drag models applicable to contaminated Kerosene-Nitrogen and commercial systems at high pressures and high phase fractions, which is expected to quantitatively refine the critical bubble diameters for phase separation.

2.3.4 Scaling by Mean Residence Time

To provide a practical tool to guide future design modifications and operating decisions within these systems, the results of these simulations were analyzed in terms of a proposed scaled residence time (κ) given by equation 2.3.3.

$$\kappa = \frac{V_s}{\mathcal{R}\left(u_{l,inlet}A_{inlet}\right)\varepsilon_{l,inlet}} \qquad 2.3.3$$

Within this expression, the liquid velocity ($u_{l,inlet}$), inlet area (A_{inlet}) and liquid holdup ($\varepsilon_{l,inlet}$) are for the freeboard conditions entering the simulated geometry and a recycle:inlet area ratio of 1:20. The volume of the separating region, V_s, is approximated as the volume of the hemispherical region at the apex of the reactor starting at the wall position above the lip of the recycle cup.

Horizontal and vertical phase separator design equations relate the liquid phase residence time (by volume or mean phase velocity) to the velocity of a falling droplet. This provides a minimum theoretical residence time for the liquid phase to allow phase separation for a given particle/bubble diameter. The phase separation at the top of an ebullated-bed unit varies from typical phase separators in that liquid phase is removed through both outlets. Vapour-liquid separators will typically have a phase boundary where the dispersed phase inverts to become the liquid phase. For a gas-liquid system with good separation where coalescence isn't an issue this allows all the liquid phase to be removed from a single outlet. However, for the presented system this is not the case, and the defined recycle fraction limits the amount of liquid phase removed at the recycle line outlet. In addition, due to the geometry of the recycle pan, it is difficult to conceptualize the structure as either a horizontal or vertical separator and instead complex flow patterns primarily drive phase separation.

Hydrocyclone separators also have similarities to the system presented in this study, where various time-of-flight models for cyclone separators have been successfully employed in previous literature (Hoffmann and Stein, 2007).

Separation efficiency is plotted against log(κ) in Figure 2.3.10 for the series of simulations performed in this work within the intermediate bubble size region. Only data sets for simulations implementing the Schiller-Naumann correlation are included in this plot for clarity, as momentum coupling effects are highly dependent on the drag correlation used. While the results are preliminary at this stage, it would appear that a log-linear scaling trend exists between this residence time parameter and the separation efficiencies observed, which could provide a qualitative basis for predicting gas holdup response within an operating industrial unit as a result of variations in recycle fraction, liquid throughput and geometry modification.

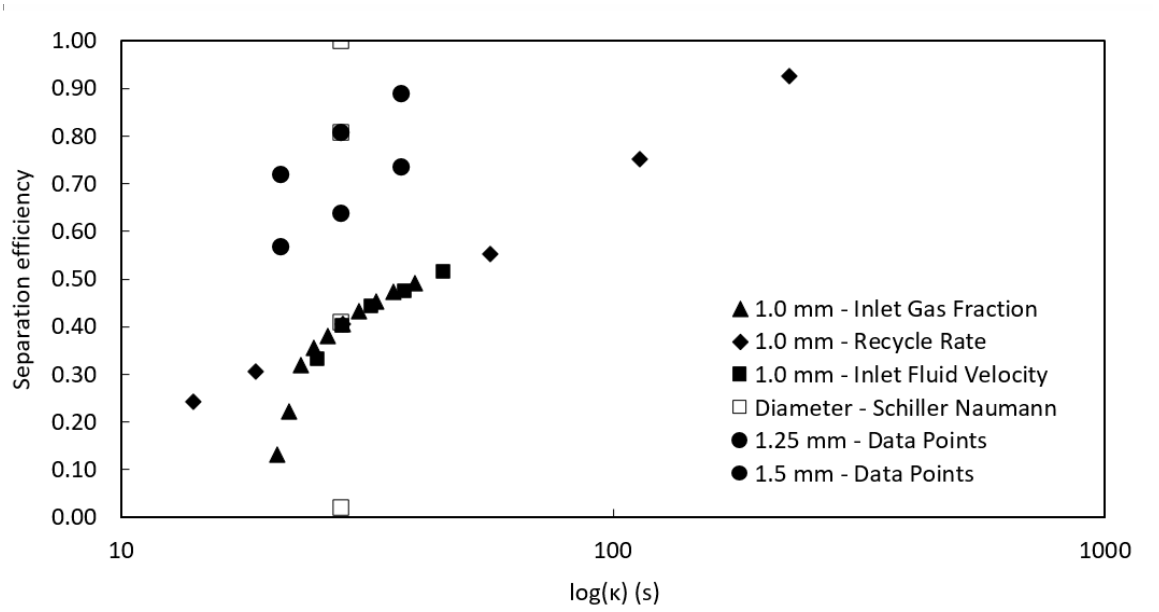

Figure 2.3.10: Separation effects of all parameters scaled by the mean residence time of an entrained bubble. Data for a given bubble diameter correlate well on this scale.

2.4 Conclusions

This work has provided visualizations of the internal flow profiles, dynamic responses, and parametric analysis of fluid dynamics and phase separation in the freeboard region of an ebullated bed reactor with internal recycle with conditions similar to those of cold-flow studies of a commercial hydroprocessor technology. The effects of fluid velocity, column gas holdup, recycle fraction, and bubble diameter were explored, and their effects on phase separation efficiency characterized, with the liquid flow rate, drag closures and bubble sizes having the greatest effects. For the range of bubble diameters commonly encountered in these units, a drag closure validated to holdups above 30% is needed to advance the performance and prediction capabilities of freeboard region simulations. This is mostly due to the difference in predicted drag coefficients for the bubbles size distributions predicted in the freeboard region, where very small (< 0.5 mm) or large (>3 mm) bubbles would be completely entrained or disengage quickly unless the separation process is limited by bubble-bubble packing present in foam structures. When a foam was introduced through a packing limiter in the CFD simulations, it was found that significant "chunks" of foam were entrained periodically in the recycle line, which would contribute significantly to increased total gas holdup within the column. This is a natural challenge for these types of units, where anti-foam additions quickly boil off at the conditions present within the unit. It's expected that the liquid fraction within these foams would approach 20%, representing a wet foam structure with deforming bubbles. For the first generation recycle pan, a log-linear relationship was observed between the separation efficiency and a residence time based scaling parameter, which may be suitable to extrapolate the effects of geometry and operational changes on gas entrainment within the recycle line.

3 Bubble Swarm Drag at Elevated Pressure in a Contaminated System

C. D. Lane[1], V. Parisien[2], A. Macchi[2], A.A. Donaldson[1]

[1] Department of Process Engineering and Applied Science, Dalhousie University, Halifax, NS, Canada

[2] Centre for Catalysis Research and Innovation, Chemical and Biological Engineering Department, University of Ottawa, Ottawa, ON, Canada

Abstract

Improved estimates of bubble dynamics in industrial gas-liquid fluid systems are important for accurately modeling multiphase flow. In many gas-liquid industrial systems at elevated pressure, bubbles exist in a polydisperse size population. This work experimentally characterizes the effects of bubble swarm polydispersity and gas holdup on drag using a monofibre optical probe in an ethanol contaminated aqueous system, providing an evaluation of current swarm drag models under industrially relevant pressures and high gas holdup conditions (up to 37% gas fraction). At atmospheric pressure, the rise velocity and swarm-corrected drag of individual bubbles within a polydisperse distribution of bubbles was found to be well-predicted by the swarm correction model of Lockett et al. (1975). An improved fit to the reported data was found using a piecewise isolated single bubble drag coefficient correlation. At elevated pressures (6.5 MPa), swarm hindrance effects were not observed for detected bubbles and the rise velocity and drag coefficient of individual bubbles within a polydisperse distribution were well predicted without the use of a swarm correction model.

***This manuscript has been published**: Lane, C. D., Parisien, V., Macchi, A., Donaldson A.A., 2016. Investigation of bubble swarm drag at elevated pressure in a contaminated system. Chem. Eng. Sci.

3.1 Introduction

To improve the robustness of gas separation estimates within an ebullated bed hydroprocessor, an experimentally validated drag correlation is required. Of particular interest for industrial scale process simulations are Euler-Euler and Euler-Lagrange type CFD solvers due to the relatively low computational cost for large simulated domains. These solvers reduce computational requirements by utilizing momentum coupling terms that are semi-empirical by nature, and thus it is important that these terms have high accuracy and robustness in order to ensure good simulation fidelity. Of the numerous proposed momentum coupling terms, drag is of particular importance. However, most drag correlations were developed for single isolated bubbles. More recent work extended these models to polydisperse bubbles traveling in a swarm where correction factors to the single isolated bubble drag correlations are proposed. Initial work by Davidson and Harrison (1966b), Bridge et al. (1964b), and Lockett and Kirkpatrick (1975b) applied the well-known Richardson-Zaki correlation for gas-solid flow to gas-liquid flow. These correlations were presented as phase velocity corrections, not as drag models, and therefore, implementation requires the selection of an unhindered/isolated bubble rise velocity value. Alternatively, more recent works by Garnier et al. (2002), Behzadi et al. (2004), Simonnet et al. (2007), Roghair et al. (2011), Roghair et al. (2013a), and Roghair et al. (2013b) have used modern experimental and numerical techniques to propose swarm corrections to the isolated bubble drag coefficient.

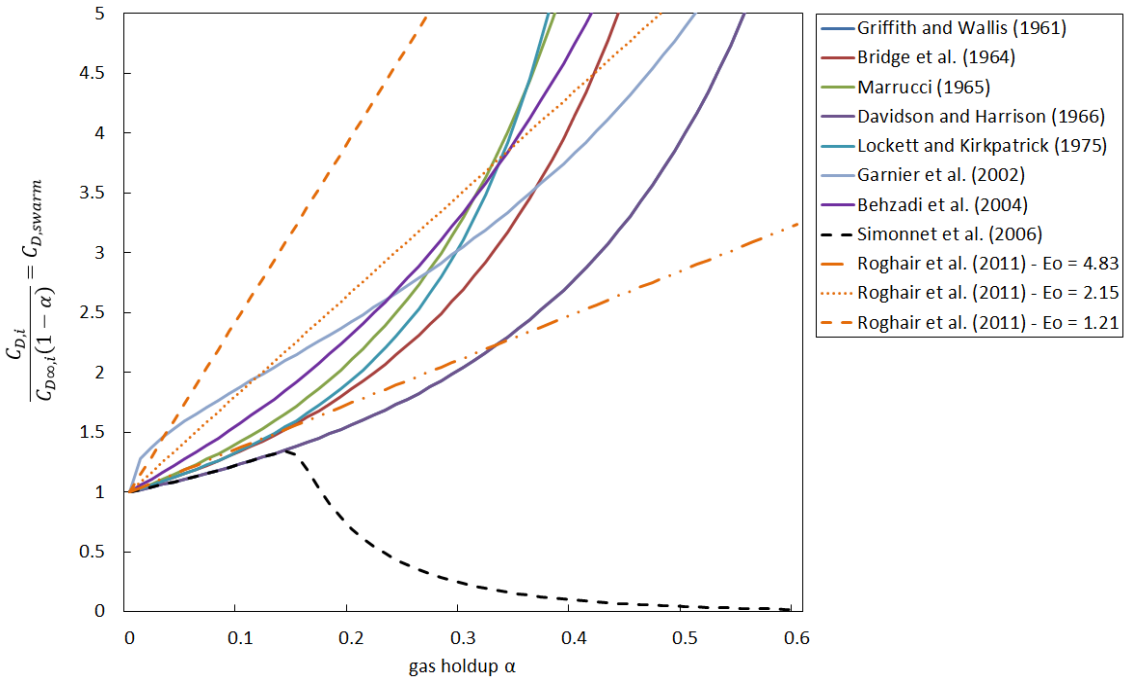

Figure 3.1.1: Current swarm correction correlations based on a single bubble model.

Figure 3.1.1 illustrates various swarm correction factors applied to the drag coefficient of a single bubble in a swarm. While there is a reasonable agreement between correlations at gas holdups below 5%, they diverge by as much as 130% (not including the Simonnet et al. model) at a gas holdup of 40%. The correlation proposed by Simonnet et al. (2007) deviates from the general increasing trend of the other models, attributed to a change in flow regime, where the onset of larger bubbles from coalescence allows for cooperative rise and therefore decreases the overall effective drag in the bubble swarm.

Consensus on a single correlation for swarm conditions appears to be elusive, partly due to isolating the contributing factors that affect the drag on a bubble in a swarm. This study investigates which model is best suited for estimating drag on bubbles in systems with contaminated fluids at both atmospheric and high pressure operating conditions where relatively small bubbles (<1.0 mm in diameter) constitute a large portion of the bubble population. These small bubbles have not been measured in isolation when developing the

swarm drag models, yet are commonly found in pressurized industrial scale processes with inherently multi-component fluid flow.

The experimental conditions and single bubble models used to develop the investigated bubble swarm models are summarized in Table 3.1.1. Of these studies, only Garnier et al., Behzadi et al., and Lockett and Kirkpatrick have experimentally presented data for gas holdups above 25%. As shown in Figure 3.1.1, experimental data at very high gas holdup conditions (>15%) is of importance, as the correlations deviate significantly from one another in this range. However, experimentally achieving gas holdup conditions above 15% is difficult without transitioning to the coalesced bubble flow regime such as that encountered by Simonnet et al. This is primarily due to the smaller diameter columns in lab-scale experimental setups and associated difficulty of maintaining the bubble-to-column diameter ratio to prevent flow regime transition into coalesced flow at gas holdups greater than 15% (Shah et al., 1982). The high gas holdup region is critical for many industrial scale operations as the larger length scales delay the onset of coalesced bubble flow to higher gas fractions, as well as inducing less non-uniformity and effects from near-wall conditions to the flow field. Therefore, it is important that drag closures are capable of accurate prediction at high gas holdup when modeling gas-liquid flow at these conditions.

.1 Summary of current single bubble swarm correction correlations

Author(s)	Approx. Max. Gas Holdup	Bubble Diameter Size Range	Contaminated/ Pure liquid	Single Bubble Model
and Wallis (1961b)	N/A	N/A	Pure	N/A
et al. (1964b)	18%	Not Specified	Pure	N/A
ci (1965a)	N/A	N/A	Pure	N/A
on and Harrison (1966b)	18%	Not Specified	Pure	N/A
and Kirkpatrick (1975b)	65%	5 mm	Pure	N/A
i et al. (2004)	45%	Not Specified	Pure	Wang (1994)
et al. (2002)	43%	3.4-5.5 mm	Pure	None Specified
et et al. (2007)	25%	5-10 mm	Pure	None Specified
et al. (2011)	50%	3-6 mm	Pure	Dijkhuizen et al. (2010)

The swarm drag correction factor is applied to a single isolated bubble drag coefficient. Typically, a monodisperse assumption is made, assuming all bubbles in the swarm to be of equal size, and the mean bubble diameter of the swarm is selected to determine the average rise velocity. This method assumes that all bubble sizes experience an identical increase in effective drag as gas holdup increases. However, in practice, all bubbly flows are polydisperse, and the monodisperse assumption is only valid when the distribution of bubble sizes is sufficiently narrow. The degree to which the distribution of bubble sizes affects the bubble swarm drag coefficient is uncertain. Two authors have previously studied the effects of bubble size distributions on the drag correction for individual bubble classes in a swarm. Roghair et al. numerically simulated a bi-disperse swarm (sphere-equivalent diameters of 3.5 mm and 4.4 mm and gas holdups from 5 to 50%) using a front-tracking method in a periodic domain (Roghair et al., 2013a). They concluded that a single drag correction correlation was able to predict the rise velocity for both the large and small bubble classes in a swarm. Recently Acuña and Finch (2010) used high-speed cinematography and bubble tracking techniques to study the velocity of bubbles in a polydisperse swarm (0.2-5 mm) rising in surfactant contaminated water. They found that faster-moving bubbles accelerate slower moving bubbles. Although no new drag model was proposed, this observation seems to be in contention with the findings of Roghair et al.

This study presents an experimental approach with novel analysis methodology that estimates swarm drag from individual bubble class measurements in polydisperse bubble flow at high gas phase holdups. The focus of this study is then to determine experimentally the most appropriate drag model for use under the following conditions:

1. High gas holdup (>5%)

2. Small and medium bubble sizes (0.1 mm < d_b < 10 mm)
3. Atmospheric and elevated pressure (0.1 to 6.5 MPa)
4. Polydisperse bubble flow

3.2 Experimental Methodology

A schematic of the experimental setup is presented in Figure 3.2.1 and detailed by Parisien (2016). The column has an internal diameter of 101.6 mm and is made of stainless steel with three sight glass windows. Gas is sparged into the bottom chamber of the column through a porous pipe where it mixes with the liquid feed. This gas-liquid mixture then passes through a perforated plate distributor into the column. Six ports are located along the column with the first 0.4 m above the distributor plate and each successive port at a 0.2 m spacing. Differential pressure transducers (Rosemount, model: 1151DP3S22C6Q4) provided measurements of the pressure profile within the column.

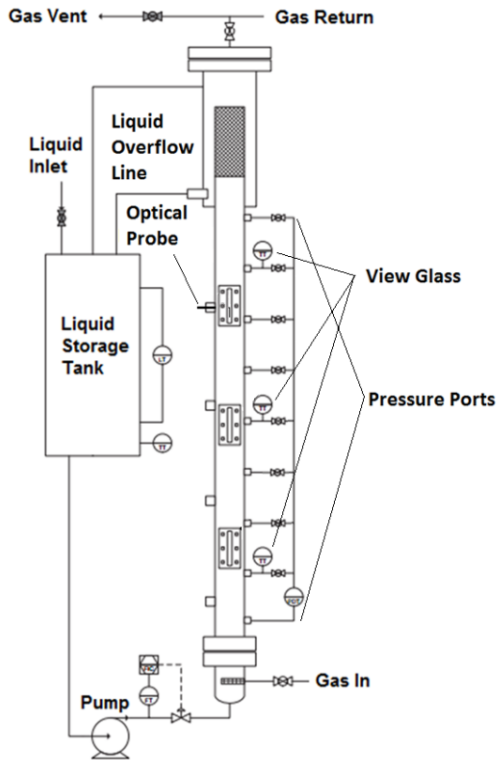

Figure 3.2.1: Experimental setup schematic. A 101.6 mm diameter column fitted with a dynamic pressure sensor and a monofiber optical probe was used for collecting all data sets.

A 0.5% wt. ethanol-water mixture was used for the liquid phase and nitrogen for the gas phase. Fluid superficial velocities were selected to limit bubble coalescence and high liquid turbulence conditions. The former leads to cooperative rise, and the latter induces large eddy currents which entrain small bubbles inhibiting optical probe detection. Flow conditions in the coalesced bubble flow regime were thus not considered as more complex phenomena affect the bubble rise velocity. Table 3.2.1 summarizes the conditions at which the system was operated.

Table 3.2.1: Experimental operating conditions and fluid properties.

Parameter	**Symbol**	**Range**	**Units**
Superficial liquid velocity	U_l	2 – 107	mm·s^{-1}
Superficial gas velocity	U_g	17.5 – 35.1	mm·s^{-1}
Pressure	P	0.1 – 6.5	MPa
Temperature	T	22	°C
Surface tension	σ	0.026	N·m^{-1}
Liquid density	ρ_l	997	kg·m^{-3}
Liquid viscosity	μ_l	0.91	mPa·s
Gas density	ρ_g	1.5 – 74	kg·m^{-3}

Gas holdup, ε_g, was measured by logging an axial pressure profile of the column at steady-state when the bubble measurements were taken. A linear regression of the differential pressure from each port provided a pressure drop per unit length of the column and can be converted to global gas fraction by equation 3.2.1, where ρ_l and ρ_g are the densities of the liquid and gas phases respectively, *g* is the gravitational constant, and *dP* is the measured differential pressure between two ports on the column located a set distance apart, *dX*. It was noted for all trials that the pressure profile along the length of the column was highly linear

($R^2 > 0.99$), indicating no significant change in gas phase holdup and a constant bubble rise velocity with respect to vertical position.

$$\alpha = \frac{dP/dX}{g(\rho_l - \rho_g)} \qquad 3.2.1$$

Bubble measurements were collected by a 1C-3C monofibre optical probe (made by A2 Photonic Sensors) positioned 1045 mm above the perforated plate distributor. The distributor plate consists of 23 holes of 3.175 mm diameter. The monofibre probe provides high spatial resolution (sensing length of approximately 30 μm) allowing direct measurements of small bubbles (<1.0 mm in chord length). This capability is important as previous experimental drag studies by optical probe have been unable to measure such small bubbles directly. The data used by Garnier et al., Behzadi et al., and Simonnet et al. to formulate their correlations was collected via optical probe. However, as noted in Table 3.1.1, measurements in this small diameter range were not reported.

Bubbles in this size range exhibit near Stokes flow behavior and provide data for drag at low, near-laminar, Reynolds numbers. The optical probe was validated by Parisien (2016) for the presented experimental setup and is shown to capture both rise velocity and chord length of bubbles down to ~0.1 mm. The velocity of a given bubble, $u_{b,r,i}$, at a radial measurement position, r, and the associated chord length, $d_{c,r,i}$ are found by equations 3.2.2 and 3.2.3, respectively, using the probe rise time ($t_{r,i}$) and time-on-probe ($t_{b,i}$) as shown in Figure 3.2.2. A minimum voltage signifies that the probe is immersed in liquid, and a maximum voltage signifies it is immersed in gas. Bubble sphere equivalent diameter for each detected bubble, $d_{b,r,i}$, can be estimated from equation 3.2.5 using a shape factor E (Simonnet et al., 2007).

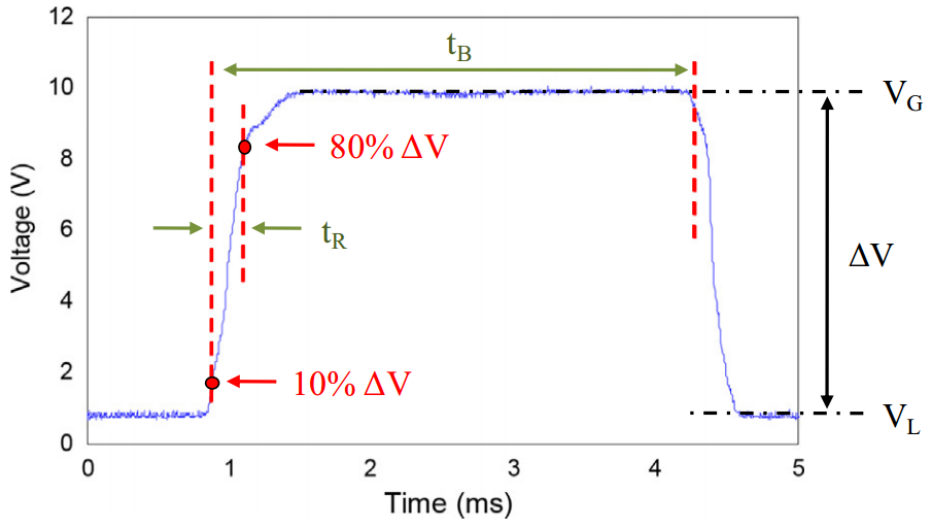

Figure 3.2.2: Example of a signal from 1C3C monofibre optical probe detecting a single bubble (Pjontek et al., 2014).

Optical probe data was collected for each radial position in 2-minute intervals, with 4 to 10 minutes of collected data for each radial position. For the lowest gas holdup condition, a total of 32 122 bubbles were fully detected, with this number increasing over an order of magnitude for the highest gas holdup condition. Partially detected bubbles, defined as bubbles for which the voltage rise did not achieve at least 80% of ΔV, were not included in the analysis to prevent bubble velocity interpolation from contributing to calculation error. Exclusion of interpolated values is not expected to contribute to sample bias as the percent of interpolated signals for a given bubble class was relatively constant although smaller bubbles (<0.5 mm in chord length) had higher frequencies of interpolated signals. The average slip velocity for a given bubble size, $u_{s,i}$, was then obtained for specific diameter-based classes accounting for both number distribution and cross-sectional weighting in the column (Eqn. 3.2.8).

$$u_{b,r,i} = \frac{L_{s,i}}{t_{r,i}} \tag{3.2.2}$$

$$d_{c,r,i} = u_{b,r,i} * t_{b,i} \tag{3.2.3}$$

$$E = \frac{1}{(1 + 0.163Eo^{0.757})} \quad 3.2.4$$

$$d_{b,r,i} = \frac{3}{2} d_{c,r,i} E^{-\frac{2}{3}} \quad 3.2.5$$

$$u_{l,avg} = \frac{U_l}{(1-\alpha)} \quad 3.2.6$$

$$\bar{u}_{b,r,i} = \frac{\sum u_{b,r,i}}{n_{b,r,i}} \quad 3.2.7$$

$$u_{s,i} = \frac{\int_r n_{b,r,i}\, \bar{u}_{b,r,i} dA_r}{\int_r n_{b,r,i} dA_r} - u_{l,avg} \quad 3.2.8$$

Here $\bar{u}_{b,r,i}$ is the time-average absolute bubble velocity measured for a given bubble size class at radial position *r*, dA_r is the fraction of the total column cross-sectional area represented by the radial measurement position *r*, $n_{b,r,i}$ is the total bubble detection count at radial position *r,* and $u_{l,avg}$ is the average liquid interstitial velocity. The average liquid interstitial velocity is computed from the superficial liquid velocity via equation 3.2.6.

The drag coefficient for a bubble class, i, is found by applying a force balance to a two phase differential volume where the drag force, $\frac{F_D}{dV}$, is equal to the buoyancy due to the shared pressure field between liquid and gas phases, $\frac{F_P}{dV}$, less the gravitational force, $\frac{F_P}{dV}$. Here, $A_{projected}$ is the cross-sectional area of a single bubble and $\frac{N}{dV}$ is the number of bubbles per unit volume. Rearranged this provides an expression for the drag coefficient, $C_{D,i}$, based on experimental measurements (Eqn. 3.2.12).

$$\frac{F_D}{dV} = \frac{F_P}{dV} - \frac{F_G}{dV} \quad 3.2.9$$

$$\frac{1}{2}C_{D,i}\rho_l {u_{s,i}}^2 A_{projected}\frac{N}{dV} = \left((1-\alpha)\rho_l + \alpha\rho_g\right)g\alpha - \rho_g g\alpha \quad 3.2.10$$

$$\frac{N}{dV} = \frac{\alpha}{\frac{4}{3}\pi\left(\frac{d_{b,i}}{2}\right)^3} \quad 3.2.11$$

$$C_{D,i} = \frac{4}{3}\frac{\rho_l - \rho_g}{\rho_l} g d_{b,i} E_i^{2/3} \frac{1-\alpha}{{u_{s,i}}^2} \quad 3.2.12$$

For a single bubble traveling in a quiescent liquid, the force balance is formulated without a shared pressure field as:

$$F_D = F_P - F_G \quad 3.2.13$$

$$\frac{1}{2}C_{D\infty,i}\rho_l {u_{b\infty,i}}^2 A_{projected} = \left(\rho_l g - \rho_g g\right)\frac{4}{3}\pi\left(\frac{d_{b,i}}{2}\right)^3 \quad 3.2.14$$

$$C_{D\infty,i} = \frac{4}{3}\frac{\rho_l - \rho_g}{\rho_l} g d_{b,i} E_i^{2/3} \frac{1}{{u_{b\infty,i}}^2} \quad 3.2.15$$

Therefore, the drag coefficient for a single bubble travelling in a bubble swarm can be expressed in terms of a gas holdup modified drag coefficient for an isolated bubble in a quiescent liquid. Note that substitution of equation 3.2.5 into equations 3.2.12 and 3.2.15 results in an expression for $C_{D,i}$ and $C_{D\infty,i}$ independent of the shape factor E.

$$C_{D,i} = C_{D\infty,i}(1-\alpha)C_{D,swarm} \quad 3.2.16$$

A corrected single isolated bubble drag coefficient, $C_{D\infty,i}$, can therefore be calculated by assuming a swarm correction term, $C_{D,swarm}$ (Eqn. 3.2.16).

$$\frac{C_{D,i}}{C_{D\infty,i}(1-\alpha)} = \left(\frac{u_{b\infty,i}}{u_{s,i}}\right)^2 = C_{D,swarm} \quad 3.2.17$$

For correlations that modify a single bubble rise velocity ($u_{b\infty}$,i) to estimate the swarm gas slip velocity ($u_{s,i}$), equation 3.2.17 can be used to compare with swarm correction factors in terms of drag coefficient.

3.3 Bubble Velocities

Bubble rise velocity data collected by the optical probe is illustrated in Figure 3.3.1. Although the data show a significant variance in measured values for a given bubble size, only the time-averaged value is of interest, and due to the large numbers of bubbles detected, there is high confidence in the time-averaged mean value. In a polydisperse swarm of bubbles, a wide variance of individual bubble velocities for each bubble size was observed. The average standard deviation of bubble velocities for a given bubble class is estimated to be roughly one-third of the time-averaged mean rise velocity.

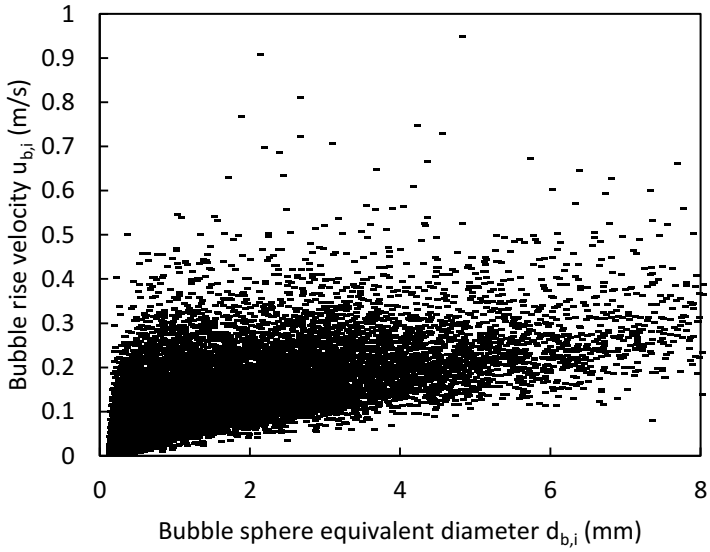

Figure 3.3.1: Plot of all bubble data points collected at U_l = 2 mm/s and U_g = 35 mm/s. An increase in the standard deviation of the rise velocity is observed for increasing bubble diameter. The mean rise velocities were found to be repeatable and of high statistical significance, providing good time-averaged rise velocity values.

Bubble measurements for each radial position of the column were collected to account for migration of the larger bubbles to the center of the column and effects of non-uniform phase distributions. For many of the trial conditions, a near uniform radial velocity profile was observed, see Figure 3.3.2. This is attributed to the relatively small bubble sizes and the combination of low liquid velocities and high gas holdup. As mentioned, low liquid flow rates are an important criterion for high confidence in bubble measurements due to the constraints of monofibre optical probes being only able to detect bubbles approaching from the direction in which the probe is oriented. It was observed from the results presented in Figure 3.3.2 that bubble detection was consistent for all radial probe positions for bubble sizes in the detection range. In the presence of non-uniform liquid flow with downward liquid currents at the wall, an increase in apparent bubble rise velocity central to the column and lower velocities near wall was observed. This effect was observed for liquid superficial velocities greater than 0.107 m/s and was not included in the data analysis. Sufficiently low liquid flow rates (0.002 m/s to 0.107 m/s) were selected to minimize near wall secondary currents formed from the no-slip wall condition and large eddy currents from churn-turbulent flow. Both of these flow regimes may entrain bubbles in downward flow, undetectable by the optical probe, biasing measurements to faster bubbles.

Table 3.3.1 and Table 3.3.2 provide the specific conditions associated with all experimental trial conditions.

Table 3.3.1: Superficial gas and liquid velocities and gas fraction for all low pressure (0.1 MPa) trials.

Trial Number	Superficial Gas Velocity (m/s)	Superficial Liquid Velocity (m/s)	Gas Holdup	Mean Diameter by Surface Area (mm)
1	0.0344	0.002	0.323	1.98
2	0.0373	0.002	0.371	2.13
3	0.0178	0.053	0.154	2.02

4	0.0349	0.053	0.272	2.19
5	0.0192	0.072	0.128	2.03
6	0.0351	0.072	0.250	2.19
7	0.0175	0.091	0.119	1.74
8	0.0352	0.091	0.221	1.94
9	0.0171	0.107	0.107	4.49
10	0.0348	0.107	0.205	3.21

Table 3.3.2: Superficial gas and liquid velocities and gas fraction for all high pressure (6.5 MPa) trials.

Trial Number	Superficial Gas Velocity (m/s)	Superficial Liquid Velocity (m/s)	Gas Holdup	Mean Diameter by Surface Area (mm)
1	0.0174	0.053	0.192	1.19
2	0.0351	0.053	0.290	1.41
3	0.0175	0.072	0.161	0.97
4	0.0341	0.072	0.263	1.29
5	0.0175	0.091	0.141	0.91
6	0.0348	0.091	0.226	1.17
7	0.0175	0.107	0.127	0.86
8	0.0352	0.107	0.203	1.08

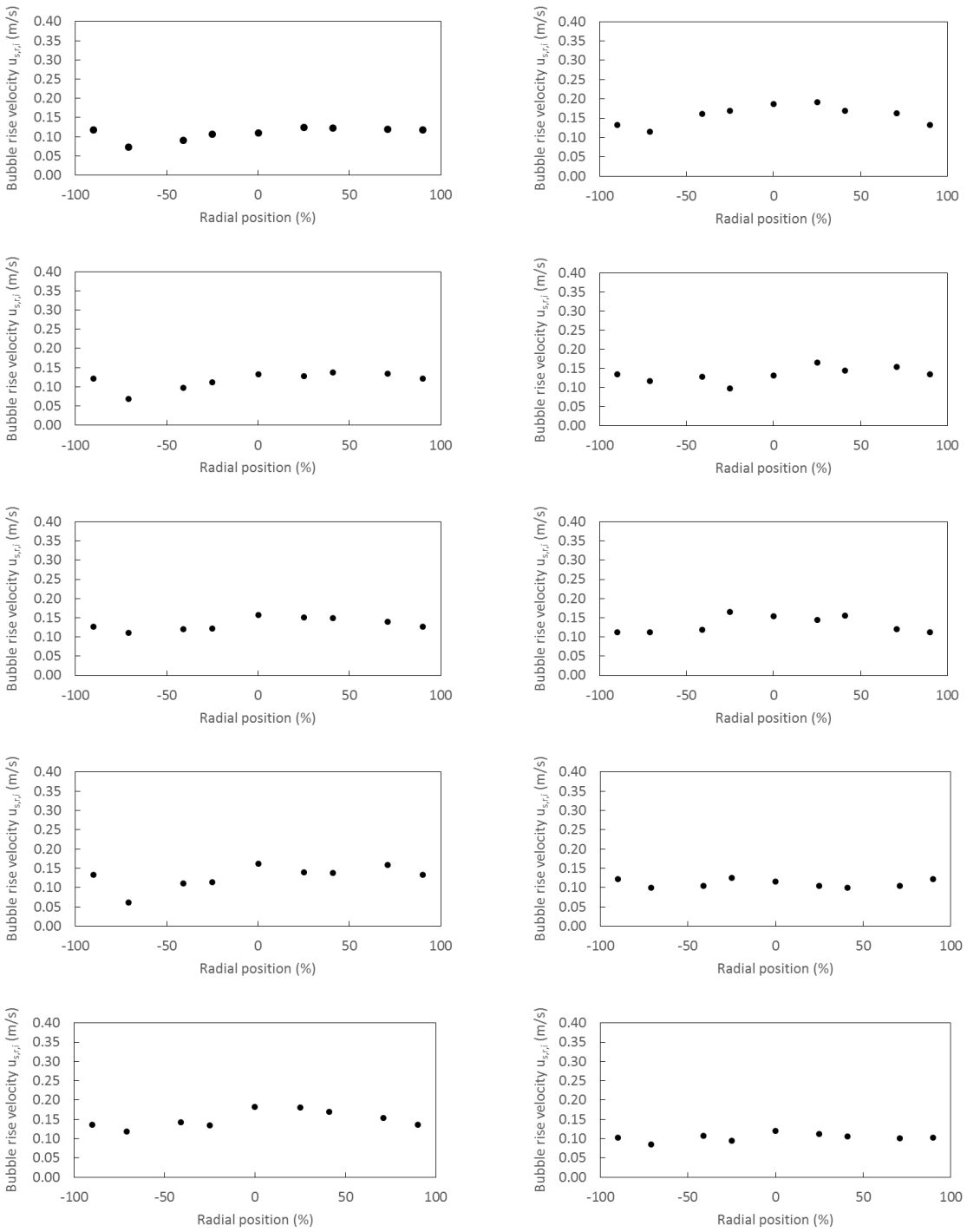

Figure 3.3.2: Radial bubble velocity profiles taken at low pressure. Relatively flat profiles were observed for all conditions.

3.4 Swarm Drag Model Comparison

Figure 3.4.1 plots the measured bubble slip velocity against bubble sphere equivalent diameter. For large bubbles ($d_{b,i}$>1.0 mm), a decrease in slip velocity is observed as gas holdup increases at low pressures, necessitating a swarm correction factor for accurate estimation of drag. At high pressures, the observed slip velocities matched well with that determined for a single bubble using the Tomiyama et al. model without swarm correction.

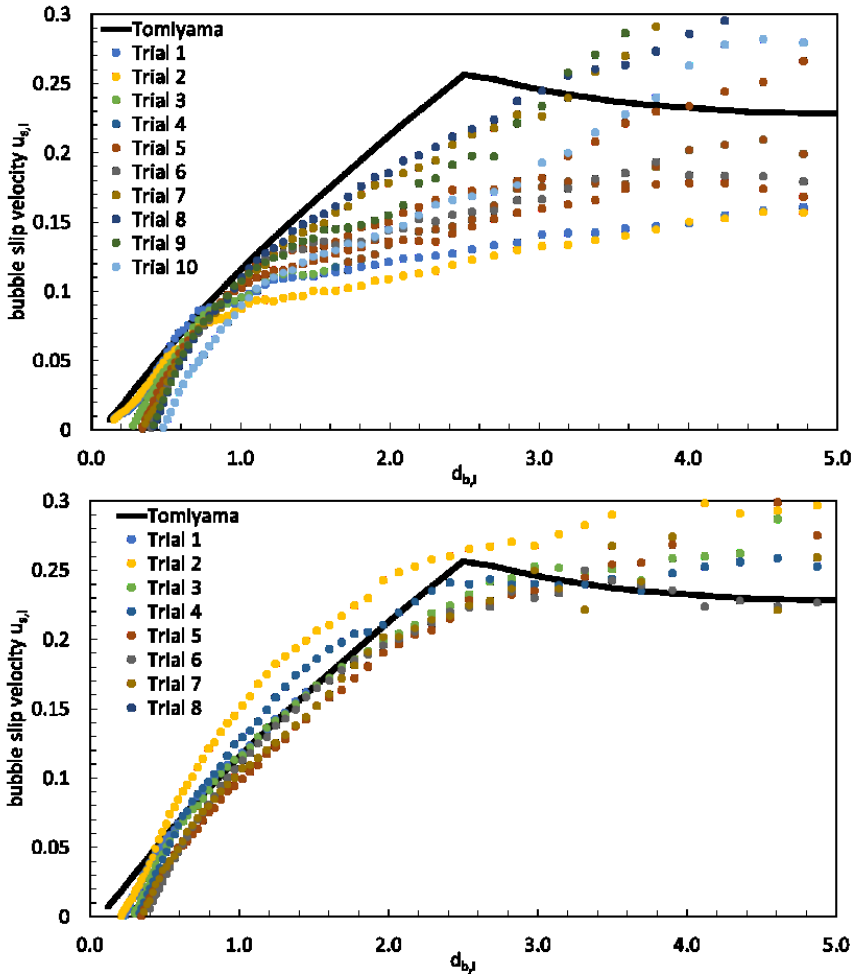

Figure 3.4.1: Bubble slip velocity ($u_{s,i}$) for low pressure (top) and high pressure (bottom) trials.

It was observed in all trials, for both low and high pressure conditions, that the experimentally measured bubble slip velocity $u_{s,i}$ is smaller than the Tomiyama et al. single bubble prediction

for very small bubbles ($d_{b,i} \lessapprox$ 0.5 mm). This deviation is attributed to a systematic measurement error where bubbles in this size range possibly have their momentum reduced on contact with the optical probe tip. This phenomena has been previously reported in literature for a similar optical probe (Vejražka et al., 2010). This causes the measured absolute bubble velocity, $u_{b,i}$, to be less than the true absolute bubble velocity. The discrepancy would then increase as bubble size decreases, as observed in our results.

The experimentally determined swarm drag correction factor $C_{D,swarm}$ vs. gas holdup for bubble sphere equivalent diameters 0.5 mm, 1.0 mm, 1.5 mm, 2.5 mm is presented in Figure 3.4.2. The swarm correction model of Lockett et al. (1975) is included for comparison. For low pressure data, the swarm correction factor is both dependant on bubble size and gas holdup. This suggests that the polydisperse nature of the bubble swarm affects the rise velocity of bubbles within the swarm. For 0.5 mm bubbles the swarm correction factor has either no trend or decreases with an increase in gas holdup, while for 2.5 mm bubbles the swarm correction factor is closely approximated by the model of Lockett et al. (1975). For high pressure trials, no such effects of polydispersity or hindrance are observed. Bubbles rise in the swarm as though they were isolated.

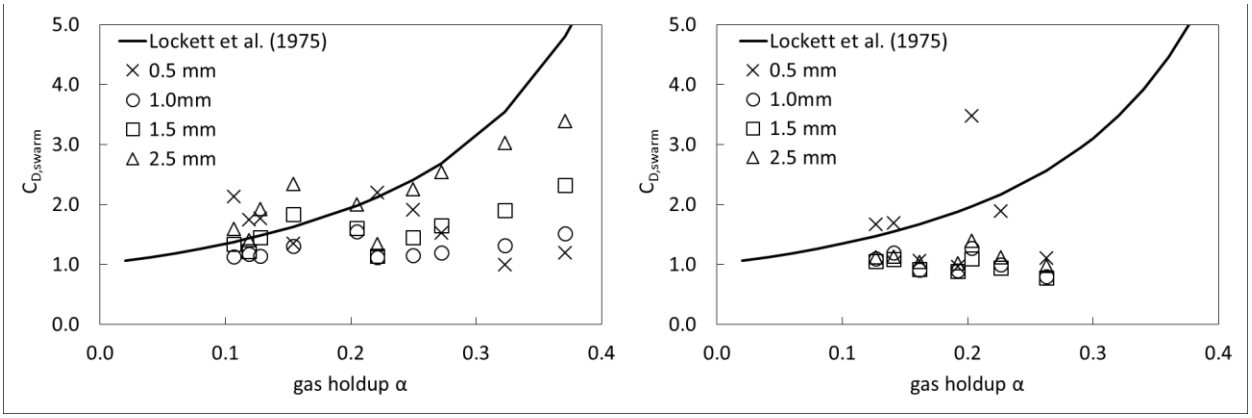

Figure 3.4.2: Swarm drag correction factor ($C_{D,swarm}$) for low pressure (left) and high pressure (right) trials.

Error analysis of previously proposed bubble swarm models is presented in Figure 3.4.3. The isolated bubble drag coefficient, $C_{D\infty,\mathrm{i}}$, is calculated from equation 3.2.16 using the models of Lockett and Kirkpatrick, Garnier et al., Behzadi et al., and Roghair et al. to estimate the value for $C_{D,swarm}$. The estimated error, defined as the difference between the calculated bubble rise velocity, computed from the experimentally derived value of $C_{D,swarm}$ and the single bubble model of Tomiyama et al. (1998), is plotted with respect to bubble diameter ($d_{b,i}$) in Figure 3.4.3. Although many single bubble drag models have been proposed, the model of Tomiyama et al. was chosen as it is applicable for bubbles in contaminated fluids and is well-known (Marchisio and Fox, 2013). The addition of a small amount of ethanol, a surfactant, reduces the nitrogen-water surface tension from 0.072 N/m to 0.0685 N/m at atmospheric pressure (Pjontek et al., 2014). Due to the Marangoni effect it is expected that the corrected drag coefficients would align best with the contaminated single bubble curve.

The authors note that Roghair et al. (2011) specified that their correlation did not extend to bubbles with an Eötvös number below 1, and as such, predictions at $\mathrm{Re}_b < 1000$ were not included as they significantly deviated from the single bubble model.

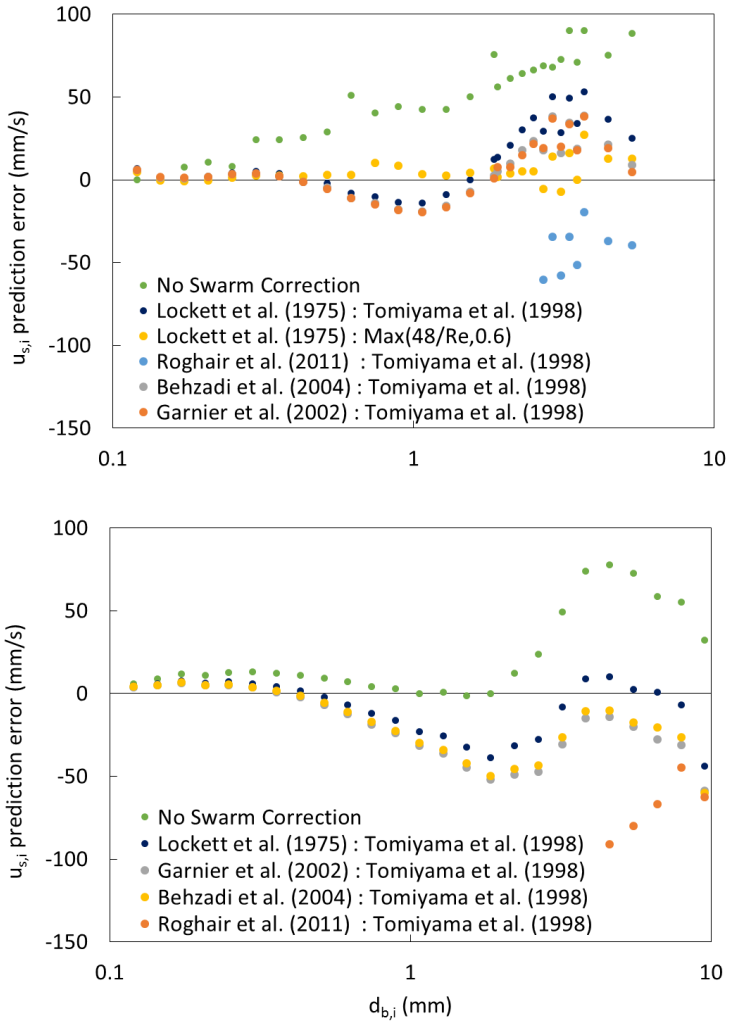

Figure 3.4.3: Error analysis for previously proposed swarm correction correlations for trials conducted at 0.1 MPa (top) and 6.5 MPa (bottom).

For low pressure trials, the swarm correction of Lockett and Kirkpatrick provides the best fit when averaged across all data sets and bubble diameters. However, an improved fit to the data was found when analysis was carried out with the single bubble drag coefficient given by equation 3.5.1 in place of the Tomiyama et al. contaminated single bubble drag correlation. For high pressure trials, a good fit to the experimentally derived $u_{s,i}$ with low variance was found when no swarm correction was applied.

3.5 Atmospheric Pressure Drag Analysis

A plot of $C_{D\infty,i}$, extracted from equation 3.2.14 using $C_{D,swarm}$ of Lockett and Kirkpatrick, as a function of bubble Reynolds number is presented in Figure 3.5.1 for all low pressure trials. The surface drag curves of Schiller-Naumann (for rigid spheres) and the Tomiyama et al. correlation for contaminated fluids are included for reference. The difference in these curves is due to the model of Tomiyama et al. accounting for bubble deformation at larger Eötvös numbers while approximating bubbles with surfactant as rigid spheres for lower Eötvös numbers.

Confidence intervals (95%) are included in Figure 3.5.1 and Figure 3.5.2 for all data sets. Confidence intervals are calculated based on the standard deviation of individually detected bubble drag coefficients from the mean isolated bubble drag coefficient and the number of detected bubbles for each bubble size class. A large number of detected small bubbles gives high confidence for the low Reynolds number region ($\mathrm{Re}_b < 100$). For larger bubble sizes ($\mathrm{Re}_b > 200$), because not as many bubbles were present, there is lower confidence in the $C_{D\infty,i}$ values.

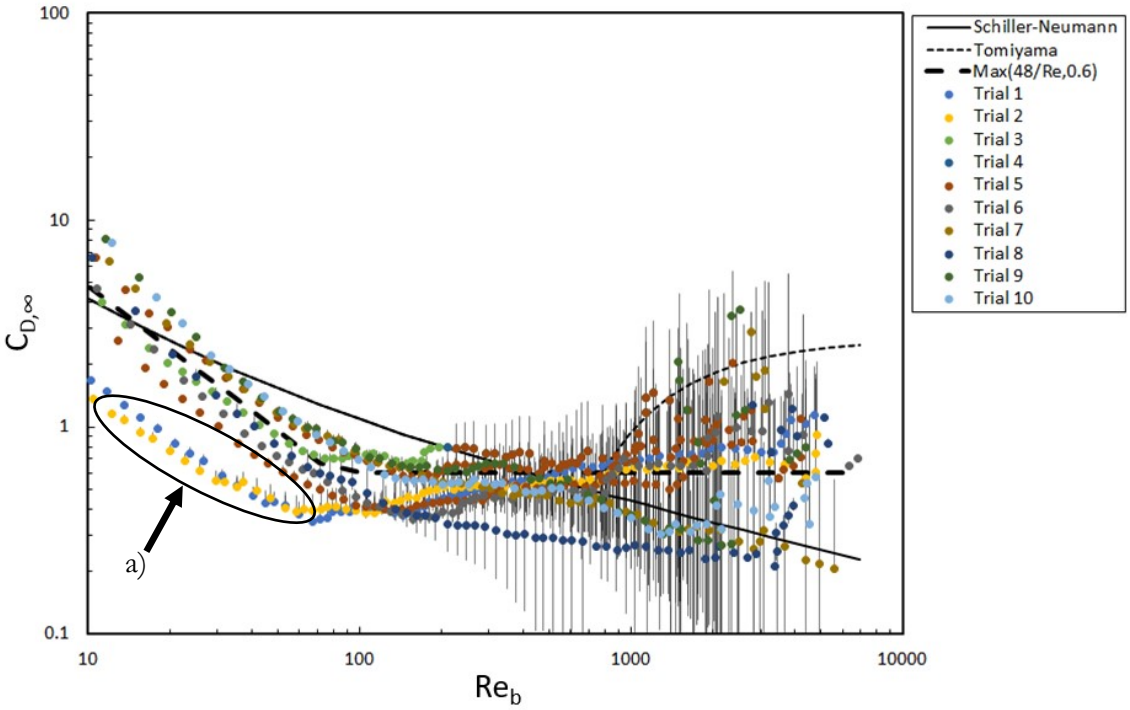

Figure 3.5.1: Experimentally derived isolated bubble drag coefficients, $C_{D\infty,i}$, for all low pressure trials. The bubble swarm correction factor of Lockett and Kirkpatrick was used. a) Small bubbles move faster in bubble distributions with larger bubble sizes.

It can be observed that, for low-pressure trials, there is significant variance in the estimated individual bubble drag coefficients across all conditions. It is noted that, under low-pressure conditions, the single bubble model of Tomiyama et al. provides a reasonable estimate for individual bubble drag coefficients in a swarm using equation 3.2.16. However, the measured drag coefficients are consistently over-predicted in the region of Re_b<200, and after the transition at Re_b>1000 (for bubbles in the ellipsoidal shape region). Two distinct slopes are observed in the experimental data for all trials. In fact, a simple piecewise function (Eqn. 3.5.1) provides a better fit than the selected Tomiyama et al. drag correlation to the observed data.

$$C_{D\infty,i} = Max\left(\frac{48}{Re}, 0.6\right) \qquad 3.5.1$$

A possible mechanistic explanation for this comes from analysis of flow through packed beds. Solid particles in a packed bed experience a more direct transition from laminar to turbulent drag conditions. This is as a result of the flow transition between laminar and turbulent flow in packed beds acting more like that of duct flow (as expressed in the well-known Ergun equation) than that of a single particle, due to the unstable and irregular nature of the flow field when particles are close together. Furthermore, this transition becomes more distinct for trials 1 and 2, corresponding to the highest gas holdup conditions of 32% and 37%, respectively. The difference in measured $C_{D\infty,i}$ values between these trials are minimal.

The bubble size distributions by surface area are given in Figure 3.5.2 for all fully detected bubbles. Surface area fraction is calculated from the square of the sphere equivalent bubble diameter. Partially detected bubbles were not included in the analysis. Partial detection occurs as a result of the raw probe signal not reaching the 80% voltage threshold as illustrated in Figure 3.2.2. A partially detected bubble may be a result of the probe piercing the bubble sufficiently off center that the gas-liquid interface interferes with the measurement by wetting the probe. Additionally, bubbles may be sufficiently small that the diameter of the bubble is smaller than the detection length of the probe. In both cases the probe cannot resolve the bubbles time-on-probe ($t_{b,i}$) and therefore is considered partially detected. For the probe employed in this study the sensing length is approximately 30 μm. Additional details on the experimental setup and probe can be found in Parisien (2016).

For trials 1 and 2, a mean surface area bubble diameter of 4.5 mm and 3.2 mm respectively while trials 3-10 all had a mean surface area bubble diameter of approximately 2.0 mm (range of 1.8 mm to 2.2 mm). This is a result of the low liquid superficial velocities used in trials 1 and 2 and reduced shearing of bubbles at the distributor plate. It can be seen in Figure 3.5.1,

notated by section a), that for small bubbles (Re_b < 100) there is a significant decrease in the experimentally derived isolated bubble drag coefficients, $C_{D\infty,i}$, and therefore bubbles in this class size range are travelling faster than the same size bubbles observed in trials 3-10. This suggests that bubbles in these small size classes affected by their larger neighbours as suggested by Acuña and Finch (2010).

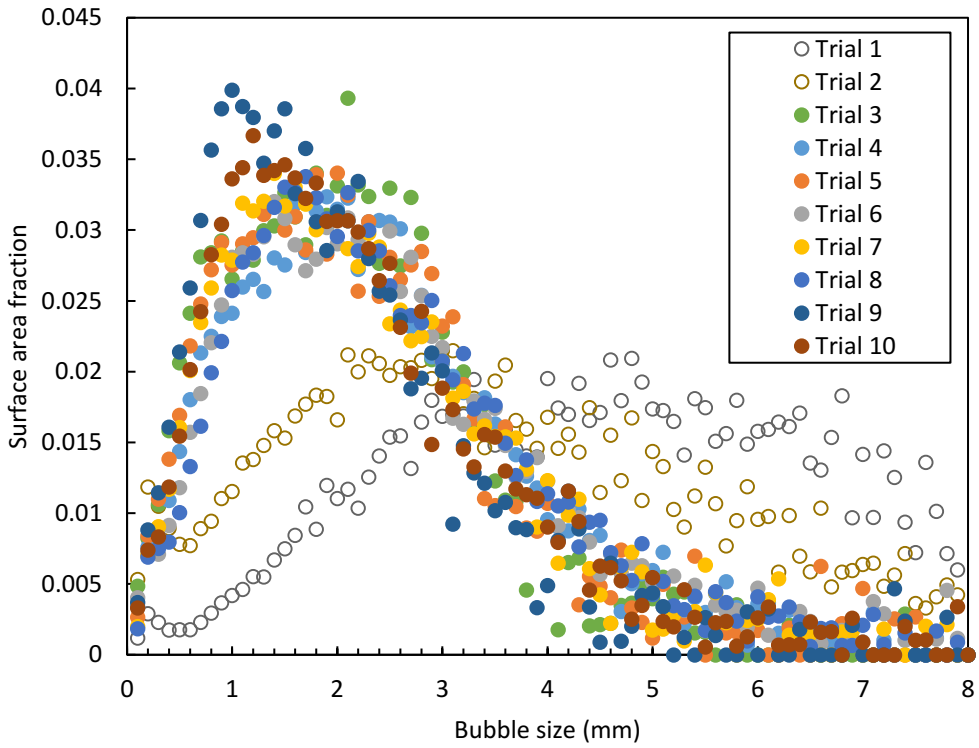

Figure 3.5.2: Surface area distributions for low-pressure experimental trials. Trials 1 and 2 have a mean bubble size shifted to the right due to low liquid flow rates providing low shear conditions at the distributor.

3.6 Elevated Pressure Drag Analysis

Under high-pressure conditions, interestingly, applying no swarm correction model provided the best agreement between experimentally measured bubble $C_{D\infty,i}$ values and the single bubble correlation of Tomiyama et al. The non-swarm corrected drag coefficient values are illustrated in Figure 3.6.1, the significant reduction in variance of measured $C_{D\infty,i}$ values between high pressure trials with respect to the variance observed for the low pressure trials

was also unexpected. Increased confidence in the mean value of $C_{D\infty,i}$, illustrated by the plotted confidence intervals, is primarily due to the increased bubble population count under high pressure trials due to a smaller mean bubble size.

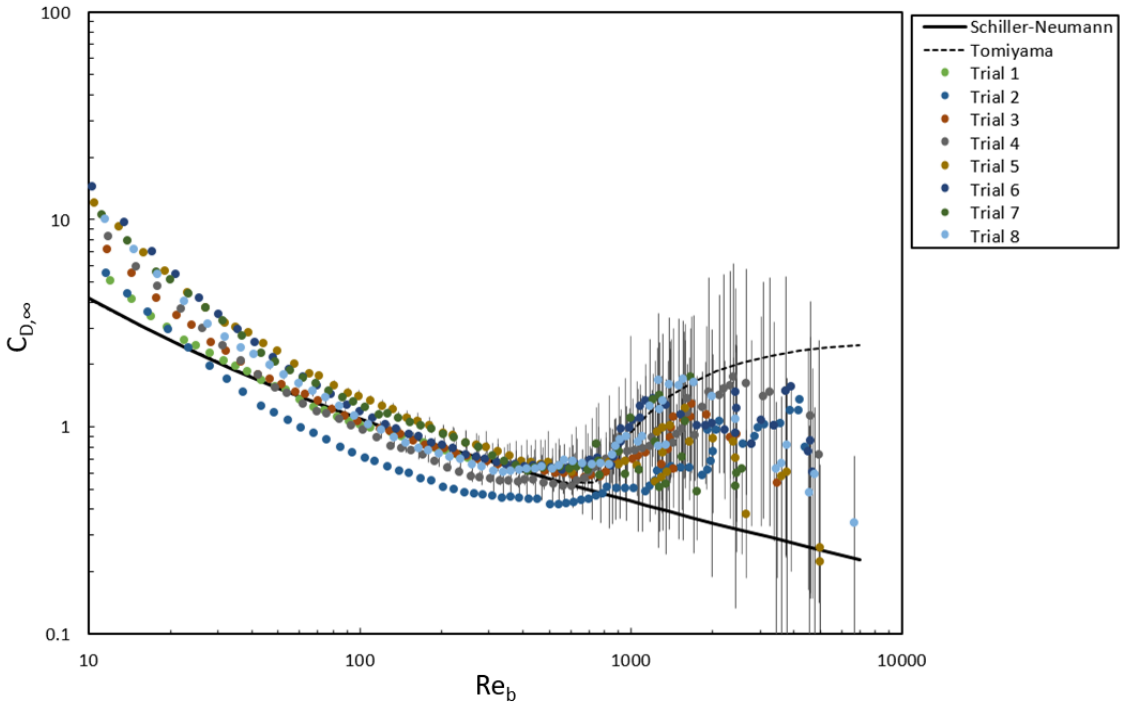

Figure 3.6.1: Experimentally derived isolated bubble drag coefficients, $C_{D\infty,i}$, for all high pressure trials. No bubble swarm correction factor was used.

Increased bubble drag at elevated gas phase fractions is a well-known phenomenon with parallels in solids hindered settling and often characterized using a Richardson-Zaki type correction term of the form $(1-\varepsilon_g)^n$. The value, n, in this expression should be considered a lumped parameter. From a fundamental perspective, this expression represents all effects of bubble liquid boundary layer changes due to the decreased length scale between bubbles at higher holdup fractions, as well as effects of changes in bubble population characteristics due to coalescence and breakage mechanisms (not found in solid systems). In addition, at high pressure conditions (6.5 MPa), increased bubble breakage and reduced bubble sizes are known to occur (Lin et al., 1998) and have been observed in this study. The bubble size distributions

by surface area for fully detected bubbles at the elevated pressure conditions is presented in Figure 3.6.2. It is noted that the bubble population for all high pressure trials is significantly smaller and narrower than the low pressure results. Surface area average bubble diameters for high pressure trials range from 0.85 mm to 1.4 mm, while equivalent low pressure trials range from 1.8 mm to 2.2 mm (trials 3-10). It is, however, possible that a significant population of micro-bubbles (less than 0.5 mm) are not represented in this figure due to the proximity of their diameter to the detection limit of the probe. It was observed from the raw probe data that detection rates of bubbles decreased significantly for bubbles under 0.5 mm and was lowest for 0.1 mm bubbles.

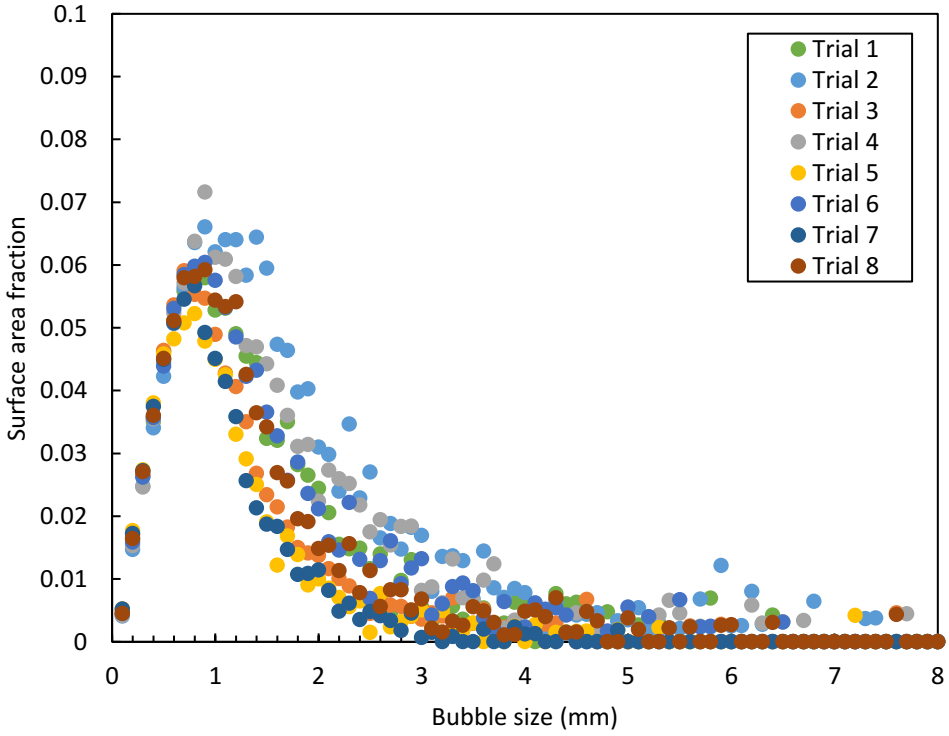

Figure 3.6.2: Surface area distributions for high-pressure experimental trials.

Our observed results, in this context, suggest that for the investigated experimental conditions, the various forces characterized by a bubble swarm correction factor and other forces, have a minimal net effect on individual bubble slip velocity.

For a similar experimental high pressure, 6.8 to 18.7 MPa, and contaminated system (coal liquefaction pilot plant), a minimal dependence of slip velocity on gas holdup (Eqn. 3.6.1) (Ishibashi et al., 2001) was also observed.

$$u_s = 0.114\left(1 - \varepsilon_g\right)^{0.02} \qquad 3.6.1$$

3.7 Bubble Morphology

A plot of the shape regime for bubbles, modified from Clift et al. (1978), shows the range of data collected in this study (Figure 3.7.1). It is noted that the transition from the spherical to ellipsoidal or wobbling shape regimes occurs at $\mathrm{Re}_b \approx 1000$, which is consistent with the drag curve divergence from the rigid sphere drag correlation of Schiller-Naumann (Figure 3.5.1 and Figure 3.6.1).

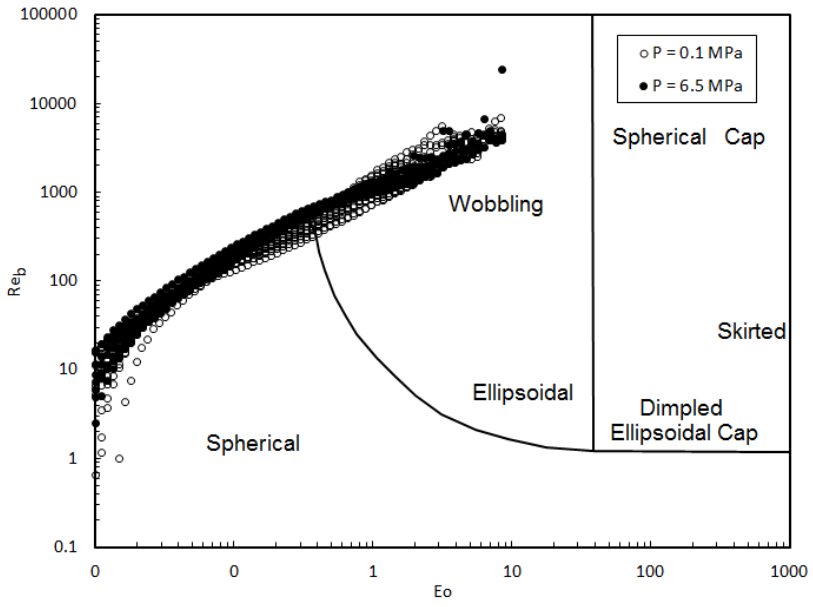

Figure 3.7.1: Shape regime map for presented results, bubbles transverse the spherical and wobbling regions.

For bubbles with an Eötvös number in the wobbling regime, the deformation of larger bubbles from buoyant forces dominating surface tension forces would be expected. This deformation

causes increased drag on the bubble primarily as a result of a larger cross-sectional area perpendicular to the rise velocity. However, in contrast to a single bubble rising in a quiescent liquid, in a chaotic flow field the pressure profile surrounding the bubble is irregular. This irregular pressure field should resist the deformation of a bubble in any single orientation. The result is that bubbles retain more sphericity at high gas holdup which would otherwise be more ellipsoidal in shape when traveling alone. This phenomenon is numerically predicted by Dijkhuizen et al. (2007) who studied the shape factor of bubbles in a swarm for gas holdups up to 15%. Our experimental results are consistent with these predictions; this effect is observed as an under-prediction of the drag curve in the high-pressure trials with respect to the Tomiyama et al. correlation at high Reynolds numbers (Re_b>1000). For low-pressure conditions, the variance in drag due to free stream turbulence obfuscates this phenomenon.

3.8 Effects of Liquid Velocity

It was observed in all low-pressure trials that higher liquid velocities generally resulted in an increased slip velocity for all bubble sizes (Figure 3.8.1). Although an increase in $u_{s,i}$ is expected with increased liquid velocity due to the dilution of the gas phase and subsequent drag reduction from a lower gas fraction, this is controlled by collecting data at two gas superficial velocities, and therefore two gas fractions. Continuous phase turbulence is known to reduce drag on spherical particles (Moradian et al., 2009; Torobin and Gauvin, 1960). For bubbly flow in a vertical pipe, liquid turbulence has three primary sources, inlet turbulence, wall-induced turbulence, and bubble-induced turbulence. Of these turbulent energy sources, bubble-induced turbulence is accounted for through the swarm drag model as previously discussed. The other two sources can be grouped into free stream turbulence which promotes momentum exchange between phases, and is proportional to the liquid velocity in this system. Trials 7, 8, 9, and 10, corresponding to the higher liquid velocities tested (91 and 107 mm/s),

show a downward trend in the drag coefficient (Figure 3.5.1) similar to that observed by Moradian et al. (2009). This phenomenon was also observed by Garnier et al. (2002) who studied liquid superficial velocities between 16 mm/s and 62 mm/s and found a consistent increase in average bubble slip velocity with increasing liquid velocity.

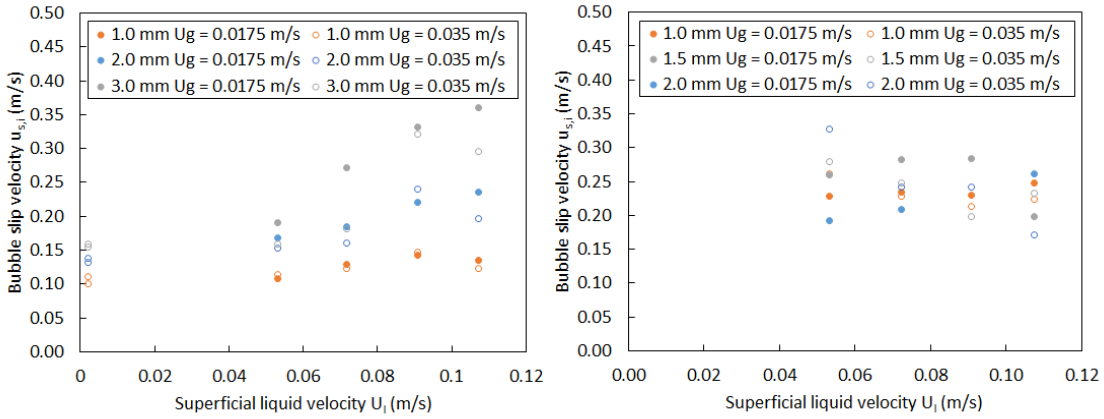

Figure 3.8.1: Dependency of bubble slip velocity on superficial liquid velocity for low (left) and high (right) pressure trials. At low-pressure large bubbles (3.0 mm) experience greater drag reduction due to free stream turbulence compared to small (1.0 mm) bubbles, a similar trend is not observed at high pressure.

It is understood that the effects of freestream turbulence cannot be fully separated from the apparent effect of the bubble size distribution on individual bubble rise velocities and subsequently drag coefficient values. One explanation for these reduced drag values is inter-swarm bubble interaction and wake effects where larger bubbles with greater terminal velocities speed up their smaller, slower neighbors (Acuña and Finch, 2010). This causes a reduction in effective drag on the small bubble classes as seen for bubbles with a $\mathrm{Re}_b < 100$ (Figure 3.5.1). For high-pressure trials, no trend is observed correlating superficial liquid velocity to bubble slip velocity. This is attributed to the reduced free stream turbulence due to the small length scales observed in the high-pressure bubble distribution. The mean length scale between neighboring bubbles for these trials is significantly smaller than that of the low-pressure trials. It is thought that these smaller length scales hinder the formation of larger

eddies and therefore reduce overall freestream turbulence, thereby limiting the accelerating effects of a turbulent flow field.

3.9 Conclusions

The presented study experimentally determines the most appropriate drag coefficient for individual bubble size classes in a polydisperse swarm under the following conditions:

1. High gas holdup (>5%)
2. Small to medium bubble sizes (0.1 mm < d_b < 10 mm)
3. Atmospheric and elevated pressure (0.1 to 6.5 MPa)
4. Polydisperse bubble flow

A high spatial resolution monofiber optical probe allowed for the determination of drag coefficients for small bubbles (< 1 mm), a bubble size class that has not previously been included in swarm drag studies, providing new insight into the behavior of these small bubbles at high gas factions.

It was found, for atmospheric conditions, that the swarm correction factor of Lockett and Kirkpatrick (1975b) applied to the single bubble drag coefficient present in equation 3.5.1 provided the best prediction of individual bubble velocities. At elevated pressure (6.5 MPa), the single bubble model of Tomiyama et al. without swarm correction yielded the lowest error. In addition, some evidence that individual bubble drag is effected by the polydisperse nature of a bubble swarm was observed, supporting the observations of Acuña and Finch (2010). Further investigation of the mechanisms of polydisperse bubble swarm drag is required to clarify the effects of hindrance at the industrially relevant conditions presented in this study.

4 Internal Gas Separation in Commercial Ebullated Bed Hydroprocessors

C. D. Lane, A.A. Donaldson

Department of Process Engineering and Applied Science, Dalhousie University, Halifax, NS, Canada

Abstract

Ebullated bed reactor technology is found in the oil and gas industry as part of the hydrocracking process, within which heavy oils are cracked under elevated temperatures and pressures to produce increased fractions of refinable petroleum products. A unique feature of these types of reactors is the presence of an internal gas/liquid separation and liquid recycle line, through which 60 to 90% of the net liquid flow through the column is recycled to maintain fluidized conditions within the internal catalyst bed. The performance of two commercial recycle pan designs are assessed by CFD and compared to experimental results from pilot plant tests. The flow-through pan performs better than the two-stage recycle cup for the bubble diameter range of 1.0 – 2.0 mm. Assessment of the flow structures and RTD using CFD is carried out suggesting that the main benefit of the flow-through pan is that it provides a more uniform RTD for bubble disengagement. The trends predicted within this work show significant similarities to current operational trends observed in the pilot plant experiments and provide a basis for predicting the effects of operational changes on the overall performance of these units.

4.1 Introduction

Reliable estimates for gas separation efficiency are essential to the overall modeling of the multiphase fluid dynamics within an ebullated bed hydroprocessor. Analysis of this separation process by computational fluid dynamics (CFD) provides relevant information about the phase separation process within these units. Ideally, direct measurement of the gas-liquid separation within a commercial unit would be used to validate CFD predictions. However, due to the severe conditions present within commercial ebullated bed reactors, fluid dynamics studies are carried out in pilot-scale experimental systems.

In this study, two patented recycle pan geometries are compared to a no-pan configuration using CFD and experimental measurements from the AMOCO cold-flow pilot plant. Unlike conventional phase separators, hydroprocessor recycle pans do not conform to generic designs or dimensions. The approach taken in this study is the selection of two industrial separator designs modeled at equivalent scale and conditions for the purpose of identifying the fundamental hydrodynamic changes which have led to an observed performance increase within the second-generation design. The two separators considered are a two-stage recycle cup (Buttke and Frey, 1989) and the second-generation flow-through pan (Devanathan et al., 1997) (Figure 4.2.1). The two-stage recycle cup is best described as a gravity based separator with no tangential flow. In contrast, the flow-through pan induces tangential or rotational flow and thus is more akin to an inverted hydrocyclone. Both of these geometries have previously been implemented in commercial scale operations, and it has been determined that the flow-through pan provides an overall favorable performance improvement (McKnight et al., 2003).

4.2 Numerical Methodology

The gas-liquid separation dynamics in the AMOCO cold-flow pilot plant unit are modeled by CFD using an Euler-Euler framework as implemented by the open-source CFD software package OpenFOAM®-2.2.0. The CFD framework employed for the study is identical to the framework described in Chapter 2.

The computational domains are based on the recycle pan geometries as illustrated by Buttke and Frey (1989) and Devanathan et al. (1997) in addition to a no-pan configuration. The no-pan configuration is modeled with the recycle line ending at the flanged connection between the downcomer and recycle pan. Detailed descriptions of these geometries can be found in the patent documentation Buttke and Frey (1989) and Devanathan et al. (1997). Figure 4.2.1 illustrates renderings for both recycle pan geometries. Additional information on the numerical methods and CFD mesh used in this study can be found in appendix A. Recycle pans are meshed as 45° wedges with symmetric boundary conditions about the vertical axis. Risers are located at the 22.5° position within the wedge to mitigate asymmetric effects near the boundary surfaces. The inlet has flow entering from the annulus of the column. The two-stage recycle cup consists of a skirt and risers, designed to capture gas under the skirt and transport it through riser tubes above the recycle cup to the top of the column ideally preventing gas from being entrained by the recycled fluid. The total cross-sectional area of the risers is 81 cm^2. The flow-through pan consists of eight 0.102 m I.D. pipes which flow enters from the freeboard region of the column. Each pipe has a 90-degree elbow expelling the fluid in a radial direction above the recycle pan.

For all simulations, the velocity of both phases is equivalent at the inlet boundary. Although this inlet condition is not strictly true, the terminal slip velocity between phases is achieved

prior to flow entering the region of active separation. This condition provides a method for matching measured gas and liquid flow rates from the annulus of the column without assuming a relative velocity between the gas and liquid phases.

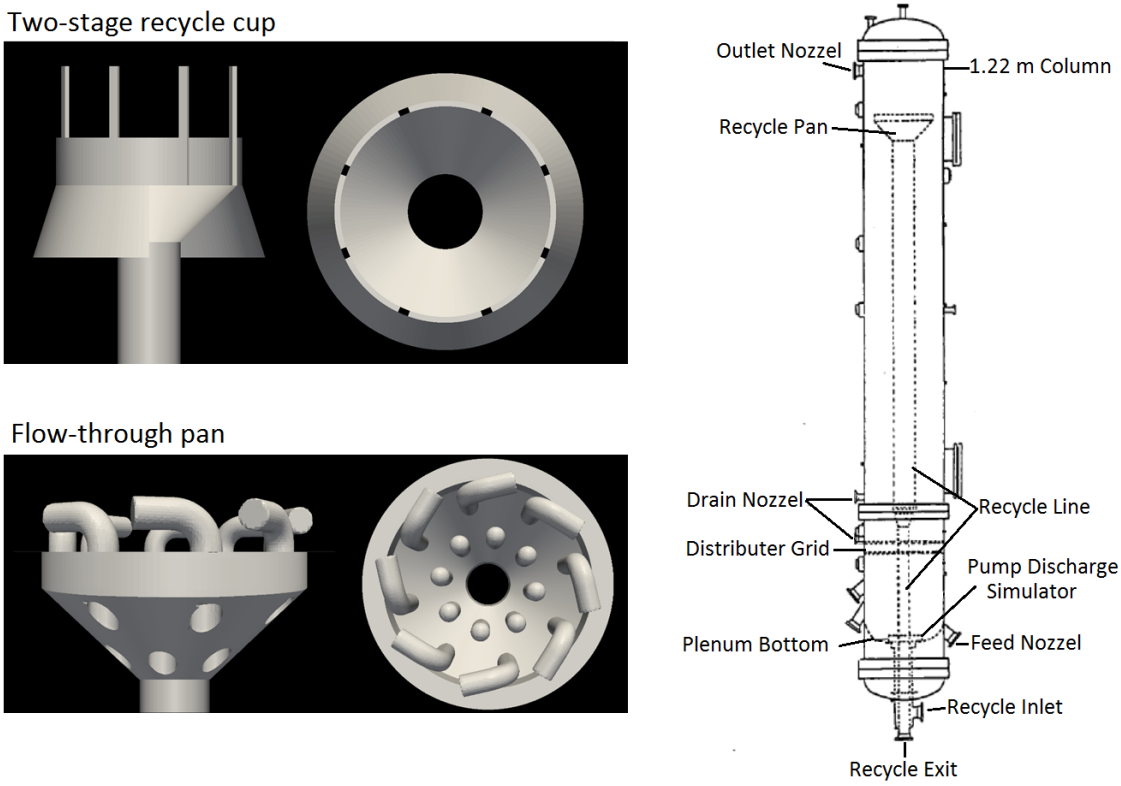

Figure 4.2.1: Left – Rendered plan and profile views of the two-stage recycle cup and flow-through recycle. Right – Schematic of the AMOCO cold flow pilot plant column.

Outlet liquid flow rates for the recycle line and product line are controlled by a recycle line outlet boundary condition which enforces an explicit ratio between the liquid mass flow rates at the recycle line relative to inlet boundary liquid flow rates as expressed in equation 4.2.1. This boundary condition is implemented by modifying the solver to use a proportional control algorithm which modifies the pressure difference between the product and recycle line boundaries. Tuning parameters are selected to result in a negligible response time relative to the time scale of the separation process.

$$\mathcal{R} \equiv \frac{\dot{m}_{l,recycle}}{\dot{m}_{l,inlet}} \quad 4.2.1$$

The recycle fraction, $\mathcal{R}$, is the ratio of liquid flow from the fluidized catalyst bed that is recycled back through the column via the internal recycle line. In the operation of a pilot-scale or commercial unit, this recycle fraction is controlled by the rotation rate of a pump located at the base of the recycle line.

Equivalent to the parameter commonly used in solids separation processes, separation efficiency (η) will be used throughout this study. Separation efficiency gives a ratio of the amount of gas removed to the liquid phase recycle fraction (Eqn. 4.2.2).

$$\eta = 1 - \frac{\dot{m}_{g,recycle}/\dot{m}_{g,inlet}}{\mathcal{R}} \quad 4.2.2$$

In the worst case scenario, where gas is perfectly mixed with liquid and no phase separation occurs the ratio of recycled gas flow rate to gas flow rate in the fluidized bed is equivalent to that of the liquid ratio in the same regions, hence, $\eta = 1 - \frac{\mathcal{R}}{\mathcal{R}} = 0$. For complete phase separation, no gas is recycled and therefore, $\eta = 1 - \frac{0}{\mathcal{R}} = 1$.

The momentum coupling drag term is aggregated to a phase average from the drag experienced by individual bubbles, where C_D is the drag coefficient for a single bubble. As multiple authors have noted, many drag correlations exist for bubble swarm flow and selection of a drag model should be empirically validated (Buwa and Ranade, 2002; Gupta and Roy, 2013; Xiao et al., 2013). As demonstrated in Chapter 3, the drag correlation for accurately estimating bubble velocities within industrial ebullated bed hydroprocessors was experimentally validated for this study. Therefore, the contaminated single bubble model of Tomiyama et al. (1998) accurately predicted individual bubble velocities (Eqn. 4.2.3).

$$C_D = max\left[\frac{24}{Re}(1 + 0.15Re^{0.687}), \frac{8}{3}\frac{Eo}{Eo+4}\right] \quad 4.2.3$$

4.3 Experimental Methodology

The AMOCO cold-flow pilot plant, representative of the commercial LC-Finer[SM] hydroprocessor, is approximately a 1:3 scale model of the industrial column (0.61 m radius) and operates with a kerosene-nitrogen analog fluid system at 138 kPa gage pressure and 20°C, while industrial ebullated bed hydroprocessors operate at significantly higher temperatures and pressures (11.7 MPa and 440 °C). This nitrogen-kerosene fluid system has been shown to be a reasonable dimensionless analog to the industrial unit operating conditions, providing confidence in the extension of hydrodynamic studies performed at the pilot facility to operational conditions. Table 4.3.1 summarizes the resulting physical properties of the gas and liquid phases for the described system.

Table 4.3.1: Physical properties of the AMOCO cold flow pilot plant

Parameter	**Symbol**	**Value**	**Units**
Liquid density	ρ_l	819	$kg \cdot m^{-3}$
Gas density	ρ_g	1.61	$kg \cdot m^{-3}$
Liquid kinematic viscosity	ν_l	4.0×10^{-5}	$m^2 \cdot s^{-1}$
Gas kinematic viscosity	ν_g	1.4×10^{-5}	$m^2 \cdot s^{-1}$
Bubble diameter	d_b	0.001	m
Surface tension	σ	0.026	$N \cdot m^{-1}$

A schematic of the AMOCO cold-flow pilot plant is presented in

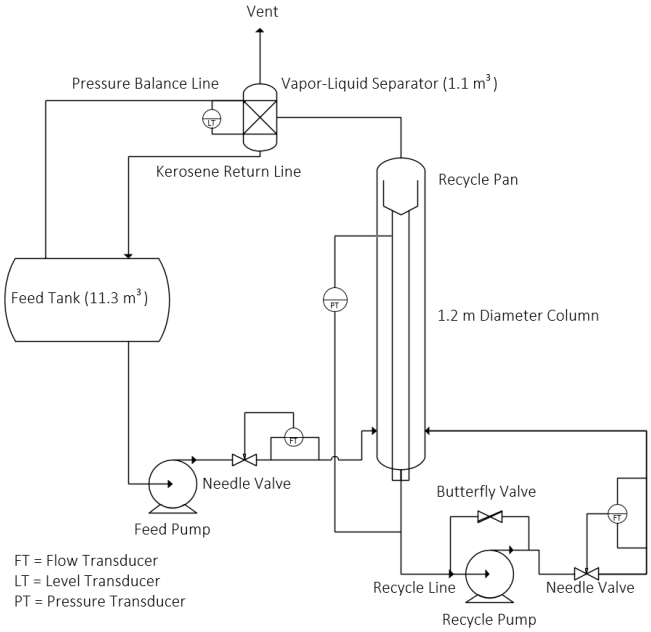

Figure 4.3.1. Fresh nitrogen gas is sparged below the distributor grid where it mixes with fresh kerosene feed, recycled kerosene, and recycled nitrogen gas. This nitrogen-kerosene multiphase mixture flows vertically through the annulus of the column where, at the top, gas bubbles are preferentially separated. Liquid and entrained gas are then drawn down the recycle line where recycled fluid is pumped through a static inline mixer and back into the column below the distributor grid.

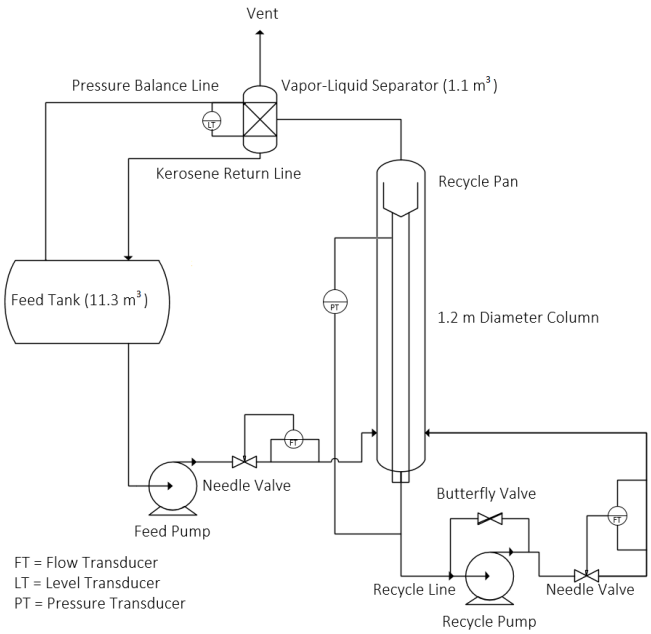

Figure 4.3.1: Schematic of the AMOCO pilot plant.

Gas separation efficiency of the recycle pan is determined experimentally from equation 4.3.1. The flow rate of gas in the annulus of the column ($\dot{m}_{g,c}$) is found from the summation of the fresh nitrogen gas flow rate ($\dot{m}_{g,i}$) and recycled gas flow rate ($\dot{m}_{g,r}$) (Eqn. 4.3.2). The fresh nitrogen gas flow rate is constant for the duration of each trial controlled by the nitrogen flow control valve. The gas holdup in the recycle line was determined using a differential pressure measurement taken between the top and bottom of the recycle line. Assuming negligible frictional drag from the recycle line wall and negligible acceleration of the phases in the vertical direction, gas holdup can be estimated by equation 4.3.4.

$$\eta \equiv 1 - \frac{\dot{m}_{g,recycle}/\dot{m}_{g,column}}{\mathcal{R}} \tag{4.3.1}$$

$$\dot{m}_{g,column} = \dot{m}_{g,recycle} + \dot{m}_{g,inlet} \tag{4.3.2}$$

$$\dot{m}_{g,recycle} = \frac{\dot{m}_{l,recycle}}{(1-\varepsilon_g)}\varepsilon_g \tag{4.3.3}$$

$$\varepsilon_g = \frac{\Delta P/(g\Delta z) - \rho_l}{\rho_l - \rho_g} \qquad 4.3.4$$

The experimental test conditions selected provide a broad range of feed gas flow and recycle rates which are considered representative of the operational conditions found in commercial scale units. Table 4.3.2 summarizes experimental and simulation conditions. CFD simulations for each configuration, flow-through pan, two-stage recycle cup, and no-pan were conducted at approximately equivalent conditions to the pilot plant experimental trials.

Table 4.3.2: Test condition ranged for CFD and cold flow studies

Parameter	Value	Units
Liquid feed flow rate	3.15×10^{-3}	m^3/s
Gas feed flow rate	1.97×10^{-3} - 6.05×10^{-3}	m^3/s
Recycle fraction	0.246 - 0.93	
Column gas holdup	10 - 30	%

4.4 Separation Performance Analysis

In Chapter 2 it was determined that the process variables, recycle fraction ($\mathcal{R}$), freeboard interstitial liquid velocity (u_l), column annular cross-sectional area (A), and freeboard liquid fraction (ε_l) provide a good correlation for separation efficiency based on an estimated recycled liquid residence time (Eqn. 4.4.1).

$$\kappa = \frac{V_s}{\mathcal{R}(u_l A)\varepsilon_l} \qquad 4.4.1$$

Separation efficiency for bubble diameters in the range of 0.05 mm to 2.5 mm were determined by CFD simulation for each configuration (Figure 4.4.1). CFD recycle fraction, flow velocities, and gas holdup simulation conditions corresponding to pilot plant experimental conditions at the intermediate liquid residence time (κ = 29 s) were selected. For all simulations, a recycle

fraction of 0.8, column superficial liquid velocity of 2.66 cm/s, and freeboard gas fraction of 0.3 were used.

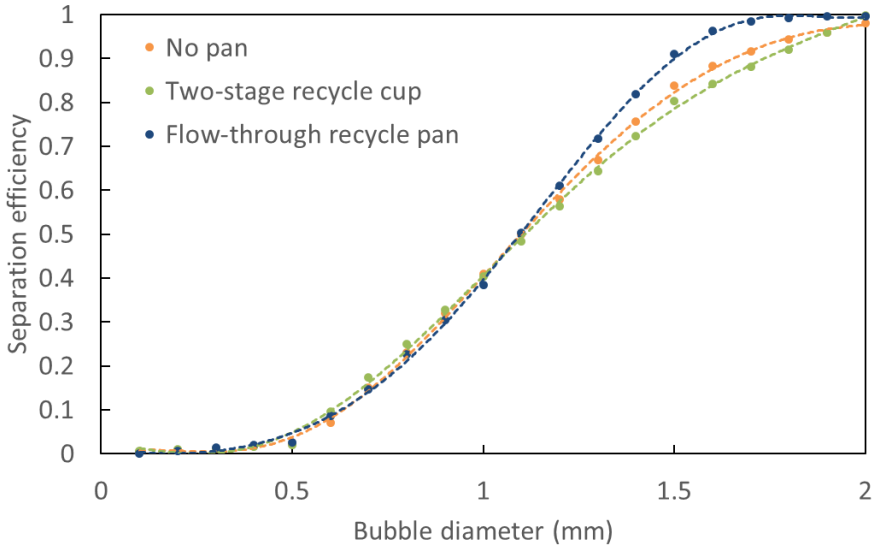

Figure 4.4.1: Separation efficiency curves for the flow-through pan, two-stage recycle cup, and no-pan configurations for the intermediate experimental liquid residence time (κ = 29 s) based on CFD results.

For large bubble diameters (d_b>1 mm), the flow-through pan demonstrates improved gas-liquid separation efficiency with respect to the two-stage recycle cup and no-pan configurations. However, for small bubbles (d_b<1 mm) there is a negligible separation difference between all three cases. This is a result of the high momentum coupling between gas and liquid phases due to increased drag on small diameter bubbles. The range, for which separation efficiency is between 0 and 1 corresponds to bubble diameters of 0.1 mm and 2.0 mm respectively. This range of bubble diameters is in agreement with the estimated bubble diameters expected in industrial ebullated bed hydroprocessors (Parisien, 2016). However, it is anticipated that the mean bubble diameter in the AMOCO pilot plant is larger than that of the commercial unit due to the significant pressure increase (0.24 MPa to 11.7 MPa) in a commercial ebullated bed hydroprocessor which is known to reduce bubble size.

A sixth order polynomial was fitted to each configuration's separation efficiency curve presented in Figure 4.4.1. Equations 4.4.2, 4.4.3, and 4.4.4 correspond to the no-pan, two-stage recycle cup, and flow-through pan respectively. Due to the nature of a polynomial fit these correlations are valid only for the range of bubble sizes tested. More generally, for bubbles less than 0.1 mm, $\eta = 0$, while for bubbles larger than 2 mm, $\eta = 1$. A polynomial function was selected over the more commonly used cumulative log-normal distribution to provide improved fit to the data. For all three equations the R^2 value was greater than 0.999.

$$\eta_{GE,NP} = -0.167d_b^6+1.33d_b^5-3.956d_b^4+5.097d_b^3-2.252d_b^2+0.366d_b-0.01 \quad \text{for } 0.1 \text{ mm} < d_b < 2 \text{ mm} \qquad 4.4.2$$

$$\eta_{GE,2S} = -0.102d_b^6+0.815d_b^5-2.339d_b^4+2.657d_b^3-0.558d_b^2-0.094d_b+0.02 \quad \text{for } 0.1 \text{ mm} < d_b < 2 \text{ mm} \qquad 4.4.3$$

$$\eta_{GE,FT} = 0.326d_b^6-1.682d_b^5+2.847d_b^4-1.922d_b^3+1.068d_b^2-0.263d_b+0.02 \quad \text{for } 0.1 \text{ mm} < d_b < 2 \text{ mm} \qquad 4.4.4$$

Experimental separation efficiency for each geometry configuration was computed for a minimum of 20 trials carried out in the AMOCO cold-flow pilot plant. Experimental separation efficiency was compared to the predicted separation efficiency by CFD for the flow-through pan and two-stage recycle cup configurations in Figure 4.4.2. It can be observed for both experimental and CFD datasets that the liquid residence time scale provides a good corollary for separation efficiency in the range of expected mean residence times.

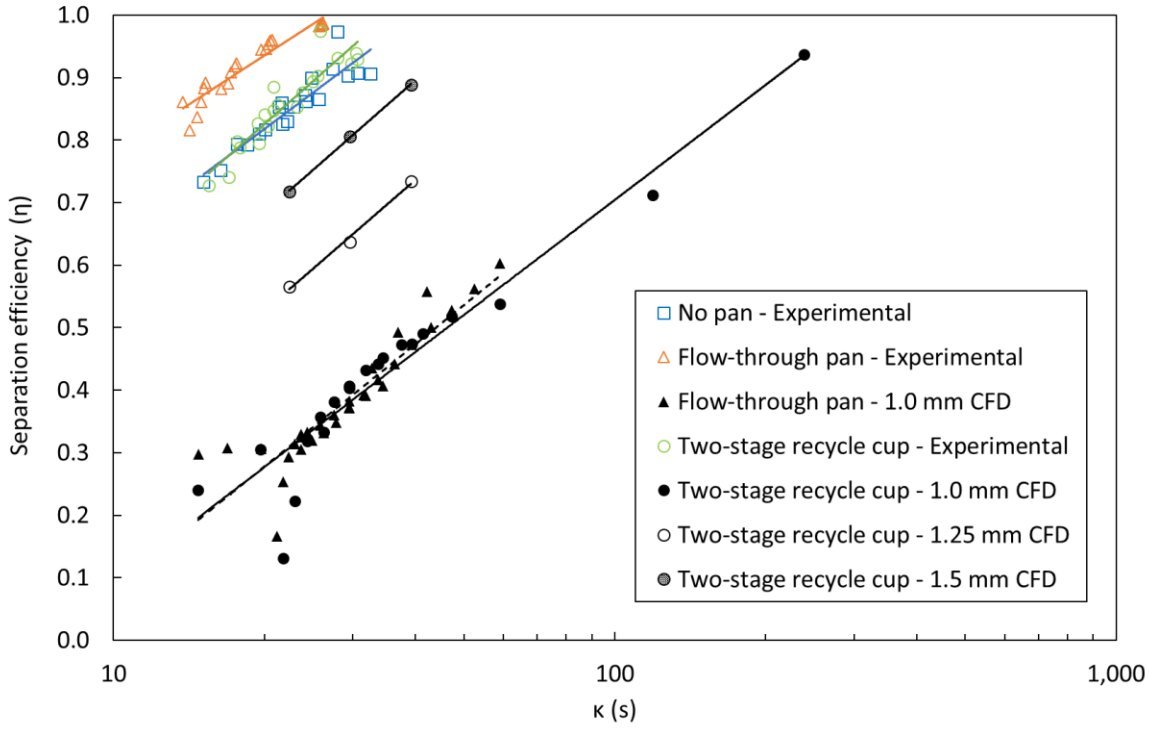

Figure 4.4.2: Gas separation efficiency from CFD predictions and AMOCO cold-flow unit experimental measurements scaled to the estimated residence time of recycled liquid. A linear regression of the log transform is applied to all CFD and experimental data sets.

For both the flow-through pan and two-stage recycle cup CFD simulations of 1 mm diameter bubbles, a log-linear regression for these data sets is found with R^2 values of 0.83 and 0.91 respectively. The coefficient of variance of the slopes for the logarithmic regression was calculated for all CFD datasets as 6.5% with a mean value of 0.29 s^{-1}. For the experimental datasets, the coefficient of variance for all slopes was found to be 15.5% with a mean value of 0.265 s^{-1}. The strong agreement between CFD predicted and experimental slopes for the log-linear relation provides confidence that this correlation can be used for the prediction of separation efficiency in commercial ebullated bed hydroprocessors. Equation 4.4.5 is therefore proposed for the estimation of separation efficiency. Here B is determined from the separation efficiency at $\kappa = 29$ s.

$$\eta = max(min(0.29ln(\kappa) + B, 1), 0) \quad 4.4.5$$

$$B = \eta_{GE}|_{d_b} - 0.29ln(\kappa)|_{\kappa=29\,s} \quad 4.4.6$$

As demonstrated in Chapter 3, a polydisperse bubble size distribution is expected within the experimental pilot plant system. Analysis of the individual bubble velocities in a polydisperse swarm demonstrates that bubbles rise independently of one another. Therefore, measured separation efficiency is an aggregate value for all bubble sizes with small bubbles preferentially entrained by the recycled flow.

Separation efficiency can be improved by two mechanisms, an increase in residence time and an increase in bubble size. While the correlation with liquid residence time are well captured by CFD, changes in the bubble population due to coalescence and breakage are not captured. For the presented pilot-plant system the flow-through pan geometry may, in addition to providing improved separation for bubbles in the range of 1.0 mm to 2.0 mm, also induce bubble coalescence, thereby improving the effective separation relative to the other geometries. Due to the small cross-sectional area of the inlet pipes (0.102 m I.D.) and a factor of 16 increase in flow rate due to a reduction of area from 1.06 m^2 to 0.065 m^2, a transition out of the dispersed bubbly flow regime is expected. However, while the onset of coalesced bubbly flow is well known for pressures near atmospheric pressure, this transition is suppressed for systems operating at pressures relevant to ebullated bed hydroprocessors (Ishibashi et al., 2001; Parisien, 2016; Rollbusch et al., 2015). While the flow-through pan may exhibit improved separation performance at near atmospheric conditions, for the purpose of assessing its performance in a commercial setting, the effects of coalescence are ignored.

For horizontal and vertical gravity separators the residence time distribution (RTD) provides insight into the difference in separation efficiency. Analysis of the recycle liquid RTD using CFD methods provides a tool for comparison of designs and assessing the potential for future improvements. For the no-pan, two-stage recycle cup, and flow-through pan geometries the recycle liquid RTD is plotted for the simulation base case condition (recycle fraction of 0.8, column superficial liquid velocity of 2.66 cm/s, and freeboard gas fraction of 0.3) in

Figure 4.4.3.

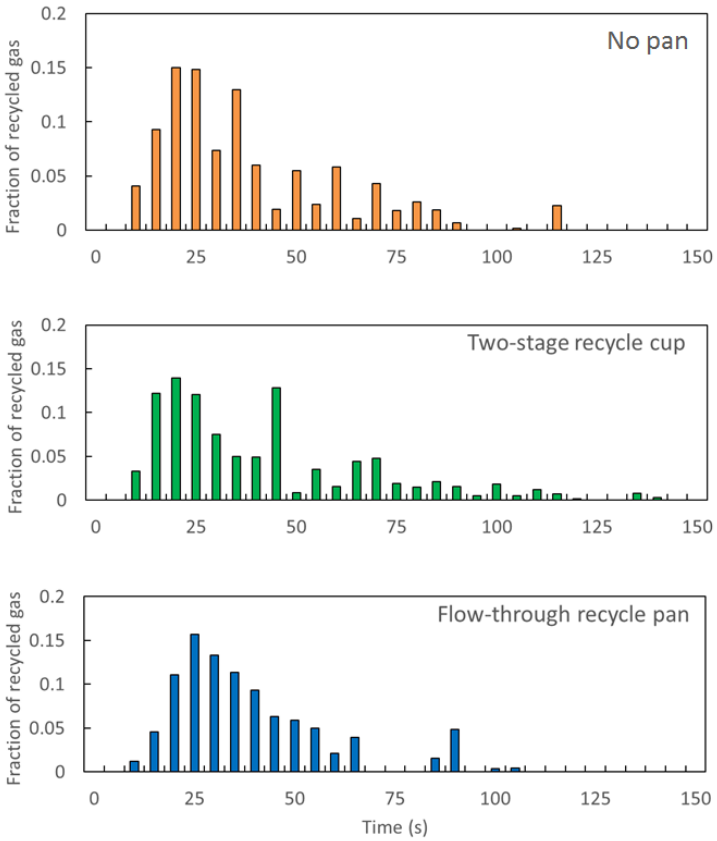

Figure 4.4.3: Normalized residence time distribution comparison between separators designs. The flow through pan exhibits a narrower distribution with respect to the two-stage recycle cup and no-pan configurations. The difference in RTD's leads to preferential separation of larger bubble diameters (>d_{50}).

Due to the inherent differences in separator geometries, the internal volume available for flow is not equivalent. Both RTDs have been normalized to the volume of the two-stage recycle cup giving a mean residence time for both geometries of 29 s. No significant phase separation is expected to occur in the freeboard region beneath the recycle cup and gas and liquid phases are assumed to be perfectly mixed at the inlet.

The two-stage recycle cup and no-pan configurations have broader RTDs (standard deviations of 26.9 s and 24.6 s respectively) than that of the flow-through pan (20.3 s) due to a combination of bypassing and dead zones. The effects of this range difference can be seen in separation efficiency curves. All geometry configurations have equivalent normalized mean residence times of approximately 29 s and show near identical separation efficiencies for an average cut diameter (d_{50}) of 0.41 (no-pan), 0.41 (two-stage recycle cup), and 0.38 (flow-through pan). For bubble diameters smaller than d_{50} no geometry provides superior performance. This is attributed to the streamlines of flow where bubbles have long residence times to disengage. However, a consequence of these regions are the areas of short circuiting where bubbles are entrained into the recycle line due to insufficient disengagement time. For bubbles greater than d_{50}, an increase in separation efficiency is observed. Two factors contribute to this. An increase/decrease in residence time has more relative significance at smaller time scales. Secondly, large bubbles (d_{50}), are not as tightly coupled to the continuous liquid phase, a result of the increased buoyancy due to increased bubble volume.

4.5 Description of Flow Characteristics

Both the two-stage recycle cup, and flow-through pan have been implemented commercially. A qualitative analysis of the flow structures developed by each geometry is presented to provide insight into the differences in the recycled liquid RTD produced by each. The two-

stage recycle cup separator generates flow profiles primarily aligned on the vertical axis, with induced recirculation near wall edges where fluid shear is high. In contrast, the flow through pan generates a tangentially circulating flow due to the orientation of the inlet pipes. Radial flow, combined with higher near-wall fluid velocities (due to the reduced inlet cross section), generates a whirlpool effect. Figure 4.5.1 and Figure 4.5.2 illustrate the time-dependent nature of the flow profiles in each separator after a step change in gas fraction at the inlet.

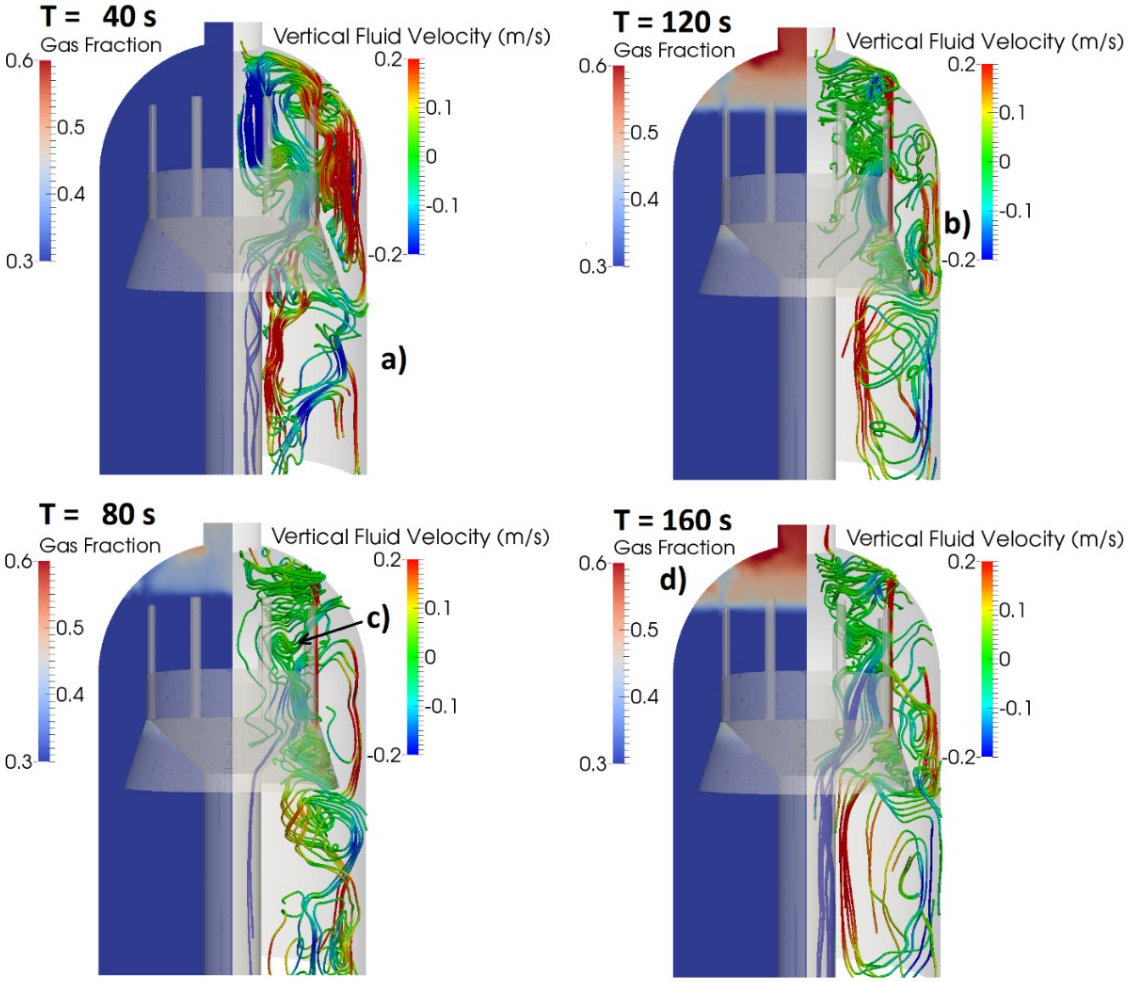

Figure 4.5.1: Streamline analysis of the gas phase flow at steady-state for the two-stage recycle cup. Identified regions: (a) Circulation induced by the presence of skirt, (b) Circulation region above the skirt, (c) region of mixing and eddy formation, and (d) region of high gas holdup and low fluid velocities are reducing active separation region.

The two-stage recycle cup geometry consists of a cup, skirt, and riser pipes, three features to aid in gas separation. The recycle cup has a larger diameter than the recycle line to reduce the downward liquid velocity, allowing for bubble disengagement prior to flow entering the recycle line. A skirt located below the recycle cup collects gas bubbles and routes the gas through risers into the headspace bypassing the region of the unit where entrainment can occur. However, due to low flow through the risers, a dead zone is produced under the skirt, inducing a region of recirculation below the cup (a). The protruding edges of the skirt generate regions of recirculation between its outer edge and the wall of the vessel (b). Phase separation occurs primarily above the skirt, and a region of high gas holdup (>60%) is predicted at the top of the vessel (d). Due to the high momentum coupling between gas and liquid as high gas fractions, this region is relatively stagnant with respect to the dispersed bubble flow below it and, therefore, reduces the overall volume available for gas disengagement. A pseudo-phase interface is developed between the regions of high and low gas holdup. This interface is horizontal and is observed to have a stagnating effect on the local fluid flow in the high gas region, caused by significant momentum coupling between phases. This stagnation region potentially reduces the available volume for phase separation and ideally should be minimized. Within the recycle cup, smaller but more numerous regions of local recirculation are induced (c) by flow over the upper edge of the recycle cup. The two-stage recycle cup is shown to create regions of recirculation and stagnation in the active phase separation region of an ebullated bed reactor. These regions of recirculation at locations (a), (b), and (c) are caused by immersed edges inducing shear into the fluid.

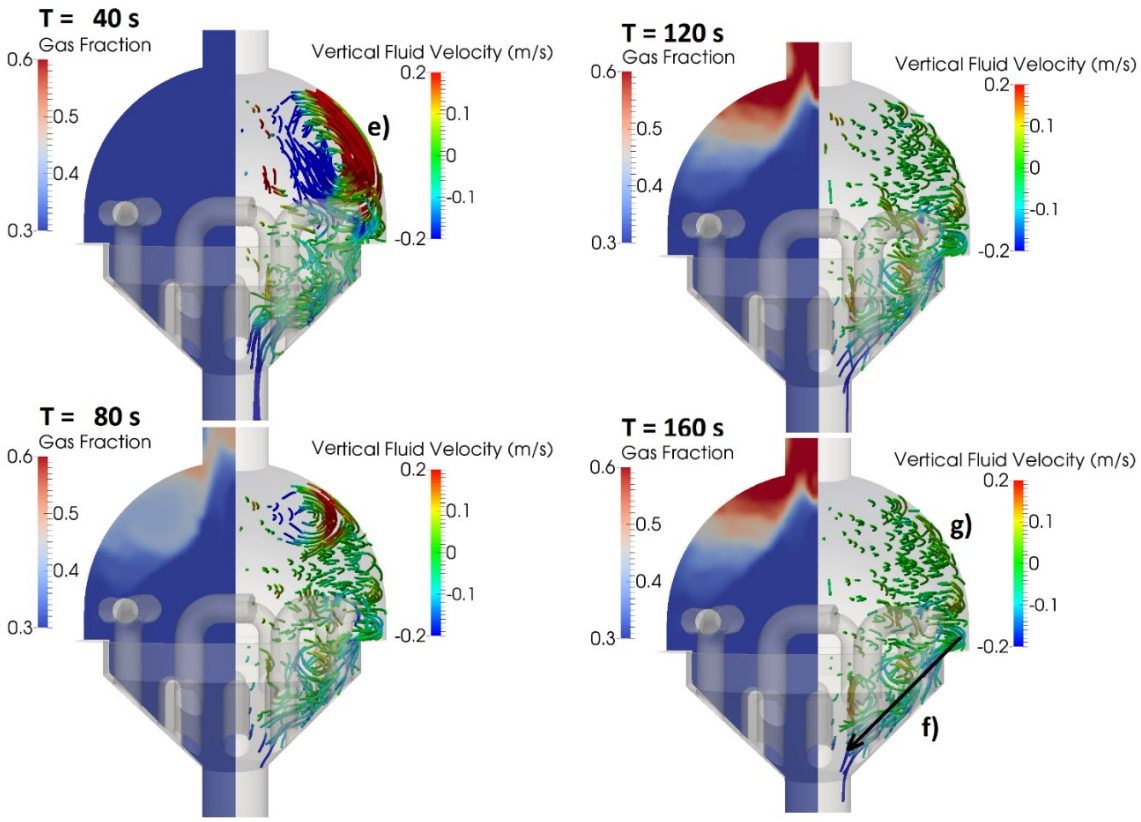

Figure 4.5.2: Streamline analysis of the gas phase flow at steady-state for the flow-through pan. Identified regions: (e) induced vertical secondary flow from the radial flow, (f) inlet flow bypassing, and (g) region of low fluid velocities due to high gas fractions.

The flow-through pan operates fundamentally differently to the two-stage recycle cup. The inlets are oriented nearly tangential to the vessel wall to maximize the incoming tangential component of velocity of the fluids. The inlet combined phase velocity is increased by a factor of ~16 due to the reduction of inlet area. Inlet pipes cannot be oriented perfectly radially tangent, as this configuration obstructs the inlet of preceding inlet pipes. This would cause intense mixing and, therefore, inlet pipes are oriented such that inflow is aligned with the outer edge of following the pipe. By configuring the inlets to maximize the inlet tangential velocity, this design mimics an inverted hydrocyclone.

Bypassing is observed in the flow-through pan simulations (f). A significant portion of the inlet fluid does not circulate upward, instead flowing down the pan walls to the recycle line. This bypassing prevents bubbles that would otherwise be removed, due to the longer path length in the secondary flow, from disengaging from the fluid and is a clear opportunity for future design revision. This is a result of the inlet located near the recycle line.

No effects of centrifugal separation are observed due to the large column diameter relative to the tangential velocity of the flow. Centrifugal acceleration does not meaningfully contribute to the gas separation. Instead, the centrifugal force causes the pressure to increase radially towards the wall of the vessel. Secondary flow is developed (e) due to the low near-wall velocities inducing an inward flow. This secondary flow is colloquially referred to as the "tea leaf effect" (Jakubowski et al., 2014). The induced secondary flow increases the path length for bubbles local to those streamlines and, therefore, is expected to improve separation efficiency. In addition to an increased path length, the secondary current circulates upward from the inlet, inward, near the top of the unit, and downward centrally. This is the optimum circulation direction for bubble separation since bubbles with a terminal velocity greater than that of the current downward velocity will be removed. Unlike the recycle cup, the gas distribution at steady state in the flow-through pan is higher near the outer wall of the reactor and lower near the central downcomer. This gas holdup distribution is similar to the characteristic solids concentration distribution of hydrocyclones with a dense discrete phase (Cortes and Gil, 2007; Neesse and Dueck, 2007; Schubert, 2010). This is unintuitive because bubbles are less dense than the continuous medium, the opposite of typical hydrocyclones. However, as noted above, this can be explained by the negligible effects of centrifugal acceleration, and induced secondary currents.

For both the two-stage recycle cup and flow-through pan, a high gas fraction region is observed near the product line. In this region, there is high momentum coupling between gas bubbles and the continuous phase liquid. The result of this high phase fraction region is reduced fluid velocity. For both configurations, it can be seen that a low-velocity region is associated with high gas holdup (d & g). We conclude that although this vertical circulation may play a role in improved separation initially, at steady state the gas-rich region provides stability to the flow, reducing internal recirculation and providing a more uniform residence time for gas disengagement. Foam generation is not accounted for in this study. The volume and phase distribution of this region may vary from that predicted, but the effect on the separation process is expected to be comparable to the simulation results.

4.6 Conclusions

A comparison of CFD predictions and experimental studies of the internal gas-liquid separation process of an ebullated bed hydroprocessor has been presented. CFD analysis of the flow-through pan geometries gas separation efficiency and RTD predict improved performance over a previous generation two-stage recycle cup for the bubble diameter range of 1.0 mm to 2.0 mm. The flow characteristics of two commercially implemented internal geometries were studied to gain insight into the inherent differences in separation efficiency. The geometries selected for this study are representative of two fundamentally different fluid dynamics, gravity based and swirling separation. It was determined that the flow-through pan design was capable of inducing secondary flow through simulation of the multiphase separation process by CFD. The secondary flow developed by the flow-through pan promoted phase separation by increasing the residence time for large bubbles. A correlation for the gas separation efficiency in an ebullated bed hydroprocessor was proposed.

Experimental pilot plant results agree with CFD trends on the recycled liquid residence timescale.

Analysis of the flow structures present in both the flow-through pan and two-stage recycle cup revealed the sources of flow short-circuiting and dead zones. To maximize the time available for the separation of large bubbles (1.0 – 2.0 mm), it is recommended that future designs eliminate geometrical irregularities where possible to minimize flow circulation and dead zones. The flow entering form the annulus of the column should not enter the separation region near the recycle line, as this is an observed cause of short-circuiting in the flow-through pan configuration. In general, new geometries should attempt to provide as narrow a recycled liquid RTD as possible. Both geometries induced gravitational separation, as no centrifugal separation was observed in the flow-through pan simulations. Enhanced phase separation may be achieved through the implementation of cyclone separators or swirl tubes. The suitability of these technologies to the severe conditions and fouling present within a commercial ebullated bed hydroprocessor is recommended.

5 Modeling Commercial Ebullated Bed Hydroprocessor Fluid Dynamics

C. D. Lane, A.A. Donaldson

Department of Process Engineering and Applied Science, Dalhousie University, Halifax, NS, Canada

Abstract

Ebullated bed hydroprocessors are a widely adopted technology for the upgrading of heavy oil. Due to the energy intensive nature of this process, improvements and optimization are highly desirable. However, a complete understanding of the complex multiphase fluid dynamics in these units is still required to provide insight for future performance improvement. Specifically, current literature has not addressed the effects of the internal gas-liquid separation process within the reactor and the effects of entrained gas on overall reactor fluid dynamics and performance. In this study, a novel numerical model for a commercial scale ebullated bed hydroprocessor is proposed. An analysis of the estimated liquid phase RTD using a liquid axial dispersion model approach agrees with the previously assumed CSTR model assumption. Additionally, two reactor recycle pan configurations are considered, the first generation two-stage recycle cup and the second generation flow-through pan. The presented fluid dynamic model is compared to previous commercial unit experimental trials for both recycle pan configurations. The change in gas holdup due to an increase in treat gas feed rate is predicted to within 2 percentage points for both configurations, while the pump response trend is correctly predicted for the flow-through pan but not the two-stage recycle cup. A theoretical causality of the pump response is discussed. An analysis and discussion of

the effects of gas entrainment by the internally recycled liquid are also presented. This study elucidates the important role and impact of the gas-liquid separation process within an ebullated bed hydroprocessor and concludes with recommendations for performance improvement.

5.1 Introduction

Ebullated bed hydroprocessing reactors (EBHRs) are a widely adopted technology for the upgrading of heavy oil residue (Sahu et al., 2015). The fluid dynamics of these three-phase fluidized bed reactors is complex due to fluid conditions at high temperature and pressure, as well as bubble-particle and bubble-bubble interactions. A sparsity of literature relevant to the conditions and fluid properties contributes to an absence of a predictive fluid dynamic model for a commercial EBHR (Leonard et al., 2015; Rollbusch et al., 2015). Advances in the understanding of EBHR fluid dynamics will aid in the design improvement of current and future commercial units (Pjontek et al., 2015; Ruiz et al., 2005; Sanchez et al., 2008).

Previously, Eccles (1993) proposed a gas holdup correlation for an EBHR based on data from Exxon's Donor Solvent Coal Liquefaction program (Tarmy et al., 1984). This gas holdup model accounts for recycled gas within a commercial scale unit. However, it is specific to the geometry and fluid properties of the reported system. More recently, an investigation by Schweitzer and Kressmann (2004) developed, and experimentally verified, a liquid axial dispersion model for a bench-scale EBHR and was shown to accurately predict liquid residence time distribution (RTD) and conversion. Gas recirculation was not accounted for in the experimental setup or numerical model. Gas holdup was estimated using the approach developed by Krishna et al. (1997) limiting the scalability. Cheng et al. (2014) provided a comparison of a continuous stirred-tank reactor (CSTR) model to an axial dispersion model, similar to that of Schweitzer and Kressmann (2004), demonstrating the benefits of the axial dispersion approach for modeling conversion. Gas holdup was estimated using a bi-disperse bubble size approach, where the approach of Krishna et al. (1997) was used for large bubbles and the approach of de Swart and Krishna (2002) for small bubbles. Similar to the approach

of Schweitzer and Kressmann (2004), the gas holdup correlation does not scale to commercial units.

Investigations of scale-up correlations for EBHR fluid dynamics using a dimensionless similitude approach have attempted to provide more robust estimates of phase holdups (Safoniuk et al., 1999; Sanchez et al., 2008). Additional investigations by Macchi et al. (2001) demonstrated the requirement for a novel dimensionless scaling approach valid for multi-component liquids. In a follow-up work, Pjontek et al. (2015) presented experimental validation at high gas holdup for a multicomponent fluid using a modified version of the dimensionless approach proposed by (Safoniuk et al., 1999).

Although numerous studies have been conducted, measured gas holdup in an LC-Finer^{SM} (Figure 5.1.1), an ebullated bed hydroprocessing technology, is not well predicted by current gas holdup models (McKnight et al., 2003). In this study, we expand on this work and present a novel methodology and numerical framework for predicting phase holdup estimates and liquid residence time for an industrial EBHR. Incorporation of the effects of the recycled gas phase provides a more robust overall fluid dynamic model.

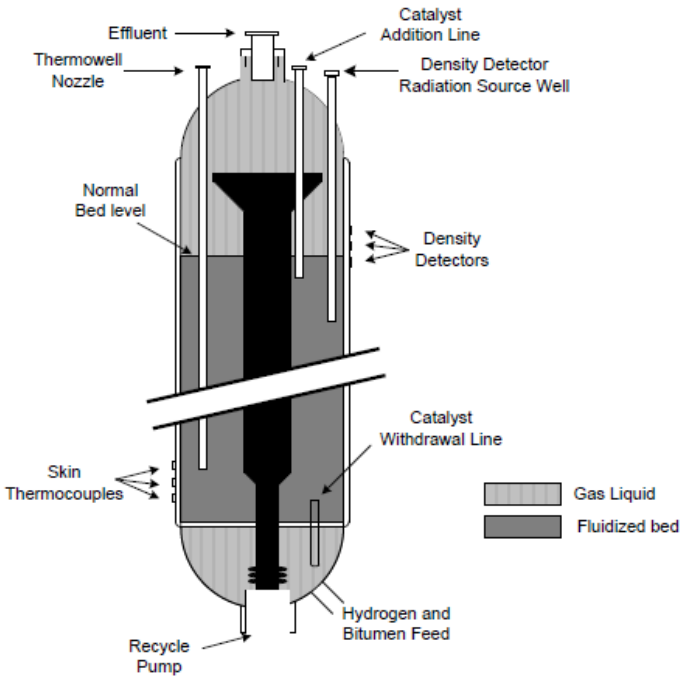

Figure 5.1.1: LC-Finer[SM] schematic (modified from McKnight et al., 2003).

5.2 Numerical Methodology

An ebullated bed reactor is considered as a four component system (Figure 5.2.1). The control volumes selected are the sub-grid region, three-phase fluidized bed, internal gas-liquid separation, and recycle line. The sub-grid volume consists of the volume located below the distributor grid which is bounded by the recycle pump. Here, treat hydrogen gas is sparged into a combination of recycled and feed liquid hydrocarbon, typically vacuum residue (VR). This region is assumed to be occupied by the gas and liquid phases only. The gas-liquid mixture flows through bubble caps installed on the distributor grid providing an approximately uniform distribution of gas and liquid into the fluidized catalyst bed region above. The catalyst bed interface is considered the boundary of the three-phase fluidized bed volume. Above the fluidized catalyst bed is the freeboard region of the reactor where internal gas-liquid separation

occurs. An internal recycle pan located in this region improves gas–liquid separation, preferentially removing gas. The effluent gas-liquid mixture contains excess hydrogen, unconverted and product hydrocarbons. The internal gas-liquid separator region ends at the flanged connection to the recycle line downcomer, where the recycled gas-liquid mixture is drawn down and recycled to the sub-grid region by the recycle pump.

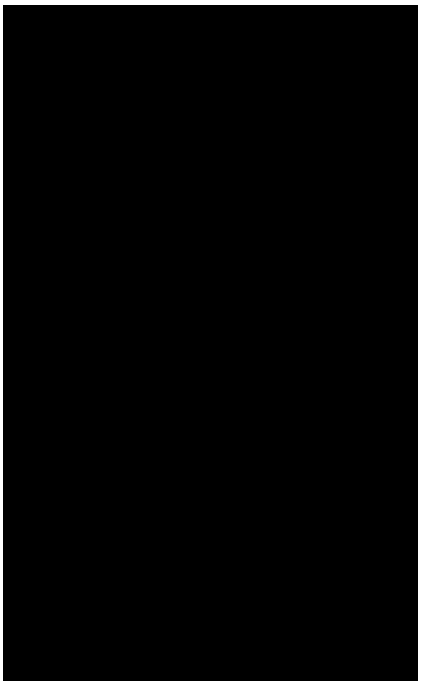

Figure 5.2.1: A compartmental model of an industrial ebullated bed reactor.

5.2.1 Three Phase Fluidized Bed

Three-phase fluidized beds have been the subject of many studies (Fan, 1989). Although correlations exist to predict phase holdups and fluidization behavior, many do not extend well to commercial scale units operated at severe conditions. A modified form of the well-known Richardson-Zaki equation (Eqn. 5.2.2) has been experimentally validated using a dimensionless similitude approach valid for multi-component systems (Pjontek et al., 2015). This correlation is used for the estimation of solids holdup. Haider and Levenspiel (1989)

provide a good estimate of the free-settling velocity for a cylindrical catalyst particle (Eqn. 5.2.1). For spherical catalyst particles, the correlation of Khan and Richardson (2007) may be used to estimate the n index. However, for irregular catalyst shapes such as cylinders experimental determination of the n parameter is preferable. In this model, n was fitted experimentally using spent (equilibrium) hydroprocessing catalyst from a commercial LC-Finer[SM] hydroprocessor (Parisien, 2016). The wall effect parameter k was assumed to be 1.0 due to the large column diameter of commercial units (~3.6 m).

The minimum fluidization liquid velocity for a three phase fluidized bed can computed from equations 5.2.3 to 5.2.7 (Pjontek et al., 2015).

$$Re_{l,T\infty} = \frac{d_V U_{l,T\infty} \rho_l}{\mu_l} = Ar_l^{1/3} \left(\frac{18}{Ar_l^{2/3}} - \frac{2.335 - 1.744\phi}{Ar_l^{1/3}} \right) \quad 5.2.1$$

$$1 - \varepsilon_s = \left(\frac{U_l}{k U_{l,T\infty}} \right)^{1/n} \left(1 + 0.22 \left(\frac{U_g}{U_l} \right)^{0.92} \right) \quad 5.2.2$$

$$Re_{l,mf} = \sqrt{\left(\frac{150(1-\varepsilon_s)}{3.5\phi} \right)^2 + \frac{{\varepsilon_s}^3 \left(1 - \varepsilon_{g,mf}\right)^3 Ar'_L}{1.75}} - \frac{150(1-\varepsilon_s)}{3.5\phi} \quad 5.2.3$$

$$Ar'_l = \frac{\rho_l \left(\rho_s - \left(\rho_g \varepsilon_{g,mf} + \rho_l \left(1 - \varepsilon_{g,mf}\right) \right) \right) g {d_V}^3}{{\mu_l}^2} \quad 5.2.4$$

$$\varepsilon_{s,mf} = \varepsilon_{s,mf}|_{U_g=0} \left(1 - 0.34 \left(1 - \frac{U_{l,mf}}{U_{l,mf}|_{U_g=0}} \right) + 0.22 \left(1 - \frac{U_{l,mf}}{U_{l,mf}|_{U_g=0}} \right) \right) \quad 5.2.5$$

$$\varepsilon_{g,mf} = \frac{0.16 U_g}{\varepsilon_{s,mf} \left(U_g - U_{l,mf} \right)} \quad 5.2.6$$

$$\varepsilon_{s,mf} = \frac{0.415}{\sqrt[3]{\phi}} \quad 5.2.7$$

The fluidized bed region gas holdup is calculated from the bubble rise velocity. Gas holdup correlations based on superficial gas and liquid velocities do not account for bubble diameter and therefore cannot account for distributor effects. A more general drag model approach for estimating gas holdup is used. Applying a force balance to a single bubble gives an equation for its terminal velocity which, in the aggregate, is equivalent to the relative velocity between phases, referred to as the slip velocity (Eqn. 5.2.9). The bubble drag model of Tomiyama (1998a) (Eqn. 5.2.10) was previously demonstrated to provide a good approximation of bubble rise velocity for high pressure contaminated, and therefore coalescence inhibiting, systems (Lane et al., 2016). The expected volumetric mean bubble diameter in an ebullated bed hydroprocessor is estimated experimentally to be in the range of 0.3 mm to 0.5 mm (Parisien, 2016) with previous theoretical estimates of 1 mm (Grace and Zhu, 1992).

Previous holdup correlations accounted for the presence of large bubbles (>5 mm) due to the transition of the gas-liquid flow from homogeneous dispersed flow to coalesced flow. However, these gas holdup correlations are based on studies conducted at superficial gas velocities representative of a slurry column which is significantly higher than the superficial gas velocities expected in an EBHR. Further, for contaminated systems at high pressure, the transition to coalesced bubble flow is observably suppressed (Ishibashi et al., 2001; Parisien, 2016; Rollbusch et al., 2015). Krishna et al. (2000) investigated the transition to coalesced flow at elevated pressures. However, expected operational conditions are within the dispersed bubbly flow regime and, therefore, coalesced bubbly flow is ignored. Industrial data suggests

that a transition to coalesced bubble flow does occur (Eccles, 1993; Ishibashi et al., 2001), though not within typical operational parameters. Further work is required to understand this transition in commercial EBHR.

Conversion of feed VR to volatile hydrocarbon product is expected to contribute to the overall reactor gas holdup. A study of the vaporization of volatile hydrocarbons at bench-scale demonstrated that non-negligible fractions (measured to be in the range of 15% to 35% by weight depending on conversion) of liquid feed, once converted, vaporize thus contributing volume to the gas phase (Gauthier et al., 2007). For the correlation proposed by Eccles (1993), a solids free gas holdup of approximately 10% is predicted with no treat gas flow. This is consistent with the vaporization of converted volatile hydrocarbon. For the LC-Finer[SM] process, a heavy VR feedstock is expected to reduce the gas phase contribution of the hydrocarbon vaporization. A robust estimate of the contribution of volatile hydrocarbons to the gas phase requires reaction kinetics and mass transfer models. Future work will focus on the integration of reaction kinetics and mass transfer with the presented fluid dynamic model. However, in this study, reaction kinetics and mass transfer are ignored, acknowledging that the results represent a lower bound estimate of gas holdup within the reactor.

$$u_{slip} = \frac{U_g}{\varepsilon_g} - \frac{U_l}{1-\varepsilon_g} \tag{5.2.8}$$

$$u_{slip} = u_b = \sqrt{\frac{4}{3}\frac{g d_b}{C_{D,swarm}}\left(\frac{\rho_g - \rho_l}{\rho_l}\right)} \tag{5.2.9}$$

$$C_{D,swarm} = C_{D,\infty} = max\left[\frac{24}{Re}(1 + 0.15Re^{0.687}), \frac{8}{3}\frac{Eo}{Eo+4}\right] \tag{5.2.10}$$

$$\varepsilon_g + \varepsilon_l + \varepsilon_s = 1 \tag{5.2.11}$$

The liquid holdup is determined from the continuity expression (Eqn. 5.2.11). An estimate of liquid RTD is found using an axial dispersion model similar to that of Schweitzer and Kressmann (2004). The change in concentration of a theoretical liquid tracer, C_l, is given by equation 5.2.12. The Péclet number for a gas-liquid-solid fluidized bed is estimated using the same method as Cheng et al. (2014) as presented in equation 5.2.13.

$$\frac{\partial C_{l,b}}{\partial \theta} - u_l \frac{\partial C_{l,b}}{\partial Z} = \frac{1}{Pe_l} \frac{\partial^2 C_{l,b}}{\partial Z^2} \qquad 5.2.12$$

$$Pe_l = \frac{Lu_l}{D_{al}} = \frac{Lu_l}{0.062(gD_T)^{0.5}\left({U_g}^3/g\nu_L\right)^{0.125} D_T} \qquad 5.2.13$$

5.2.2 Internal Gas-Liquid Separator

The recycle pan is a complex irregular geometry (Figure 5.2.2 and Figure 5.2.3) used to separate product gases from the liquid phase. Limited literature on design guidelines or expected separation efficiency of such gas-liquid separator configurations is available. Two previous separator configurations, the two-stage recycle cup (Figure 5.2.2) and the flow-through pan (Figure 5.2.3), were examined in this model for performance comparison. The studies, presented in chapter 4, of these separators using computational fluid dynamic (CFD) methods were validated using pilot plant data providing insight into the gas separation dynamics occurring at the top of the hydroprocessor.

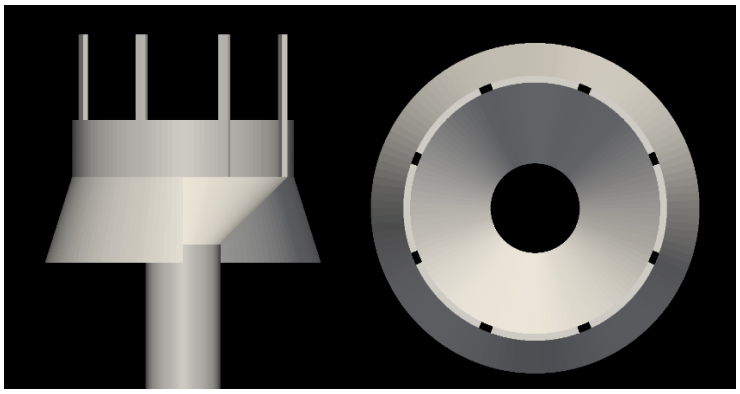

Figure 5.2.2: Plan and profile views of the two-stage recycle cup. Gas-liquid flow enters the separation region from the annulus of the reactor.

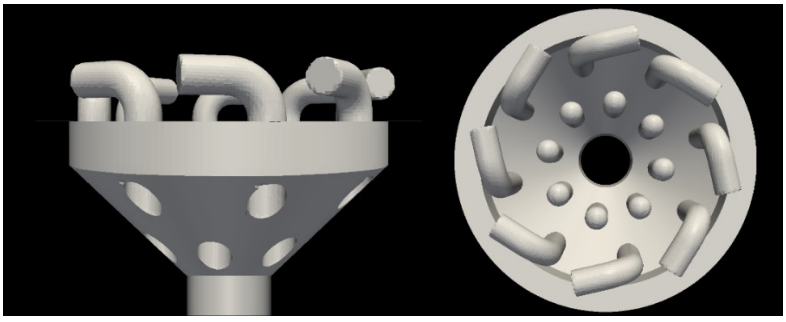

Figure 5.2.3: Plan and profile views of the flow-through recycle pan. Gas-liquid flow enters the separation region through 10-inch pipes.

Similar to conventional phase separators, a liquid recycle fraction is defined as the ratio of the internally recycled liquid flow rate to the total liquid flow rate through the catalyst bed (Eqn. 5.2.14). Gas separation performance, η, gives a measurement of the ratio of recycled gas fraction to the recycled liquid fraction (Eqn. 5.2.15). Ideal separation is found when no gas is recycled and so $\eta = 1$. Whereas, $\eta = 0$ when gas is recycled in the same proportion as the liquid. It was found in chapter 4 that a liquid residence time scale provides a good prediction of the gas separation efficiency in an EBHR.

Studies of the separation performance of the two-stage recycle pan using CFD have predicted foam generation. Assuming bubble coalescence is inhibited as previously discussed, the high

gas-to-liquid flow rates expected at the product line in the separation region may produce a type of effervescent foam. Previous authors have noted the high gas fraction (~80%) measured in this region and anti-foam studies have been performed with mixed results (McKnight et al., 2003). Previous experimental studies, under similar fluid conditions, found that foam occurs when the ratio of gas flow to liquid flow exceeds a critical value (Guitian and Joseph, 1998). While gas-liquid flow rate ratios in this range are not expected in the catalyst bed region, due to the preferential separation of gas in the separator region, foam generation may be present. Further work in this area is required to improve understanding of the nature of the gas-liquid mixture at these conditions and, if a foam exists in this separation region, how to evaluate potential impacts to reactor performance. For this study, performance effects due to the presence of foam are ignored. Additionally, it is assumed no solids from the catalyst bed region of the reactor enter the separation region and therefore the separator region is approximated as gas-liquid.

$$\mathcal{R} \equiv \frac{\dot{m}_{l,r}}{\dot{m}_{l,i}} \tag{5.2.14}$$

$$\eta \equiv 1 - \frac{\dot{m}_{g,r}/\dot{m}_{g,i}}{\mathcal{R}} \tag{5.2.15}$$

$$\kappa = \frac{V_s}{\mathcal{R}\left(u_{l,i}A\right)\varepsilon_{l,i}} \tag{5.2.16}$$

$$\eta = max(min(0.28ln(\kappa) + B, 1), 0) \tag{5.2.17}$$

$$B = \eta_{GE}|_{d_b} - 0.28ln(\kappa)|_{\kappa=28\ s} \tag{5.2.18}$$

$$\eta_{GE,2S} = -0.102d_b^{\,6} + 0.815d_b^{\,5} - 2.339d_b^{\,4} + 2.657d_b^{\,3} - 0.558d_b^{\,2} - 0.094d_b + 0.02 \quad \text{for } 0.1 \text{ mm} < d_b < 2 \text{ mm} \tag{5.2.19}$$

$$\eta_{GE,FT} = 0.326d_b{}^6 - 1.682d_b{}^5 + 2.847d_b{}^4 - 1.922d_b{}^3 + 1.068d_b{}^2 - 0.263d_b + 0.02 \quad \text{for } 0.1 \text{ mm} < d_b < 2 \text{ mm} \qquad 5.2.20$$

The separator region of the reactor is approximated as a CSTR with one inlet from the annulus of the column and two outlets; the recycle and product lines (Eqn. 5.2.21). The relatively small volume of this region with respect to the volume of the bed (approx. 8%) in addition to previous RTD studies by CFD (Lane et al., 2016) provide confidence in this approximation.

$$V_s \frac{\partial C_{l,s}}{\partial t} = \left(\dot{m}_{l,b} C_{l,b} - \dot{m}_{l,r} C_{l,r} - \dot{m}_{l,e} C_{l,e}\right) \qquad 5.2.21$$

5.2.3 Recycle Line and Internal Recycle Pump

Centralized in the reactor is an internal recycle line, where gas-liquid flow from the separation region is recycled by a pump located either externally (H-Oil) or internally (LC-Fining[SM]). The RTD of this region is approximated as a PFR (Eqn. 5.2.22).

$$\frac{\partial C_{l,r}}{\partial t} - u_l \frac{\partial C_{l,r}}{\partial Z} = 0 \qquad 5.2.22$$

5.2.4 Sub-Grid Region

The recycled gas-liquid flow mixes with fresh hydrogen treat gas and VR feed below the distributor grid. It is assumed, based on the design configuration of a typical EBHR that as both treat gas and recycled gas pass through the distributed grid, the gas phase becomes well mixed. As the gas-liquid mixture passes through the distributor grid, shearing forces significantly increase the gas-liquid surface area producing a bubble population with a small mean diameter. Improved estimates of the predicted bubble size generated at the distributor

grid are highly desirable as the phase holdup model is sensitive to the gas-liquid slip velocity and therefore the selected bubble diameter.

The sub-grid region is considered as a CSTR with the phase fraction of phase i given by equation 5.2.24, where, $\dot{m}_{i,f}$ is the feed mass flow rate of phase i, $\dot{m}_{i,r}$ is the mass flow rate contribution from the recycle line of phase i, and $\dot{m}_{i,g}$ is the mass flow rate of phase i to the bed region. Although some work has been done on the optimization of the gas sparge, an assumption of uniform gas distribution through the distributer plate can be made (McKnight et al., 2003). The volume of this region is approximately 8% of total reactor volume, therefore inaccuracies arising from the CSTR approximation are considered to have a negligible effect on the overall reactor simulation (Eqn. 5.2.23 and 5.2.24).

$$\dot{m}_{i,g} = \dot{m}_{i,f} + \dot{m}_{i,r} \qquad 5.2.23$$

$$V_d \frac{\partial C_{l,d}}{\partial t} = \left(\dot{m}_{l,f} C_{l,f} + \dot{m}_{l,r} C_{l,r} - \dot{m}_{l,g} C_{l,g}\right) \qquad 5.2.24$$

5.2.5 Algorithm

The algorithm used for the computation of the phase holdups from the described equations is presented in Figure 5.2.4. The fluidized catalyst bed height is selected based on unit geometry and the location of bed level sensors such that the expanded bed height is equal to the set point for the bed interface during operation. Feed treat gas and VR flow rates are specified, and an initial recycle fraction is set to 0.5. On initialization, a minimum fluidization velocity calculation is performed. If the minimum fluidization criteria are not met, the recycle fraction is increased. New recycle fractions were found using the bisection method. Convergence was achieved typically within 20 iterations. After each update to the recycle

fraction, all flow rates between control volume boundaries are calculated. If the minimum fluidization criteria are met, gas, liquid, and, solid holdup are calculated from equations 5.2.2, 5.2.8, and 5.2.11 respectively. Iteration of equation 5.2.8 is required due to an interdependency with bubble rise velocity.

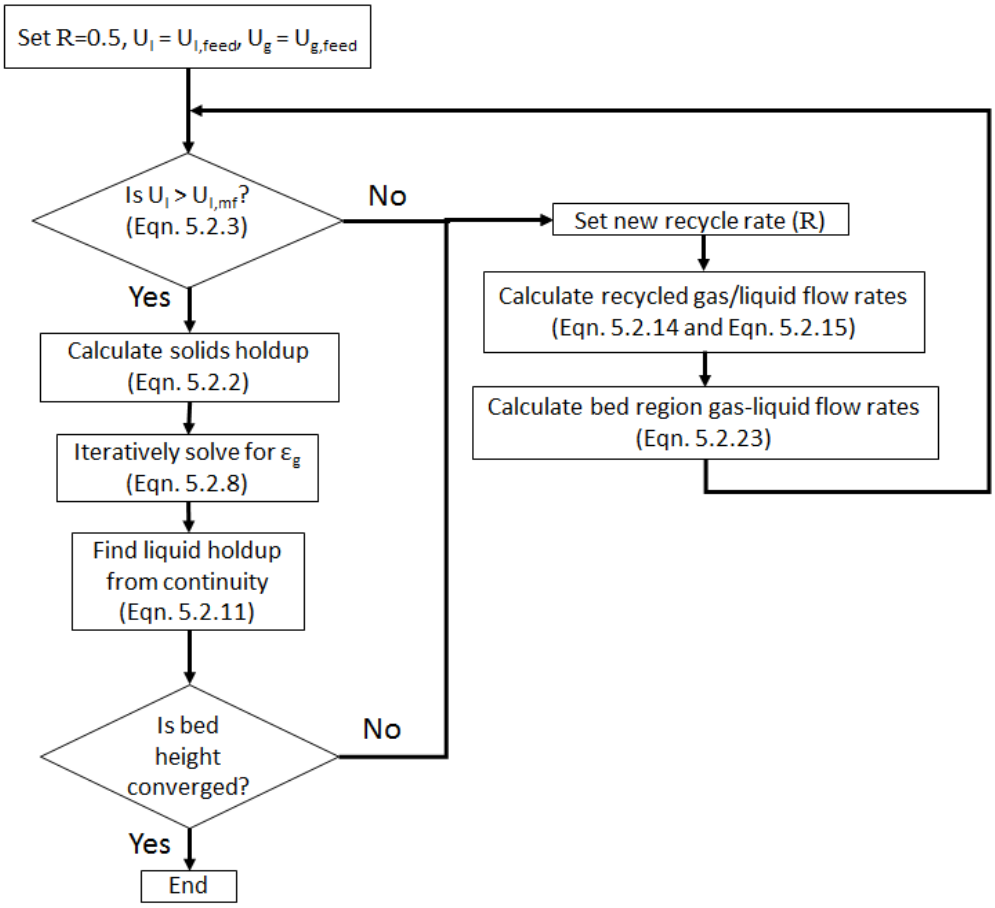

Figure 5.2.4: Solution algorithm flow chart for the presented numerical framework.

All simulations are based on the geometry of an LC-Finer[SM] operated by Syncrude Canada Ltd. For the standard conditions, and unless otherwise noted in the results section, the treat gas flow rate is 0.407 m^3/s, and the VR feed rate is 0.0552 m^3/s. A summary of the system physical properties is provided in

Table 5.2.1.

Table 5.2.1: Summary of physical properties

Parameter	Symbol	Value	Units
Pressure	P	11.7	MPa
Temperature	T	440	°C
Liquid density	ρ_l	661	kg·m^{-3}
Liquid viscosity	μ_l	1.2x10^{-4}	Pa·s
Gas density	ρ_g	50.2	kg·m^{-3}
Bubble diameter	d_b	0.25 - 0.45	mm
Particle density	ρ_s	1814	kg·m^{-3}
Particle length	l_p	3.98	mm
Particle diameter	d_p	0.88	mm

5.3 Model Analysis

5.3.1 RTD of the Liquid Phase

Previous EBHR conversion models have assumed a CSTR type RTD for the liquid phase (Schweitzer and Kressmann, 2004). The liquid RTD estimate for 0.04 m/s treat gas superficial velocity is presented in Figure 5.3.1. The presented model is consistent with a CSTR assumption for the liquid phase RTD and excellent agreement between a CSTR and the liquid phase axial dispersion model RTD is predicted for all commercial scale treat gas flow rates (0 to 0.068 m/s). There is still some uncertainty in the Péclet number correlation due to an absence of experimental studies investigating liquid dispersion for high-pressure three-phase fluidized beds of large diameter (>1 m). However, the liquid RTD is not sensitive to an order of magnitude reduction in the Péclet number. This is due to the significant liquid recycle fraction of approximately 0.65 to 0.95. For applications where the mean liquid residence time or RTD are required, the CSTR assumption thus provides a good approximation for a commercial scale EBHR.

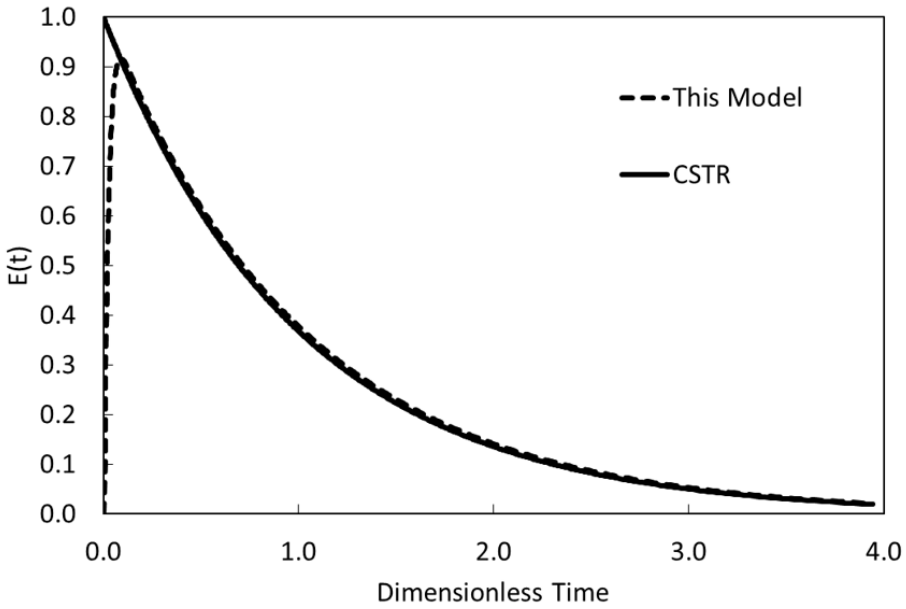

Figure 5.3.1: Liquid phase residence time distribution

5.3.2 Gas Holdups in the Freeboard

The presented numerical framework is compared to the previously reported commercial data of McKnight et al. (2003). Measured freeboard gas holdup within an LC-Finer^{SM} is compared to the freeboard gas holdup estimates of this model in Figure 5.3.2. For the commercial data reported by Syncrude Canada Ltd., the LC-Finer^{SM} is operating with a flow-through pan configuration. For other LC-Finer^{SM} data, no confirmation of the operational recycle pan configuration was available.

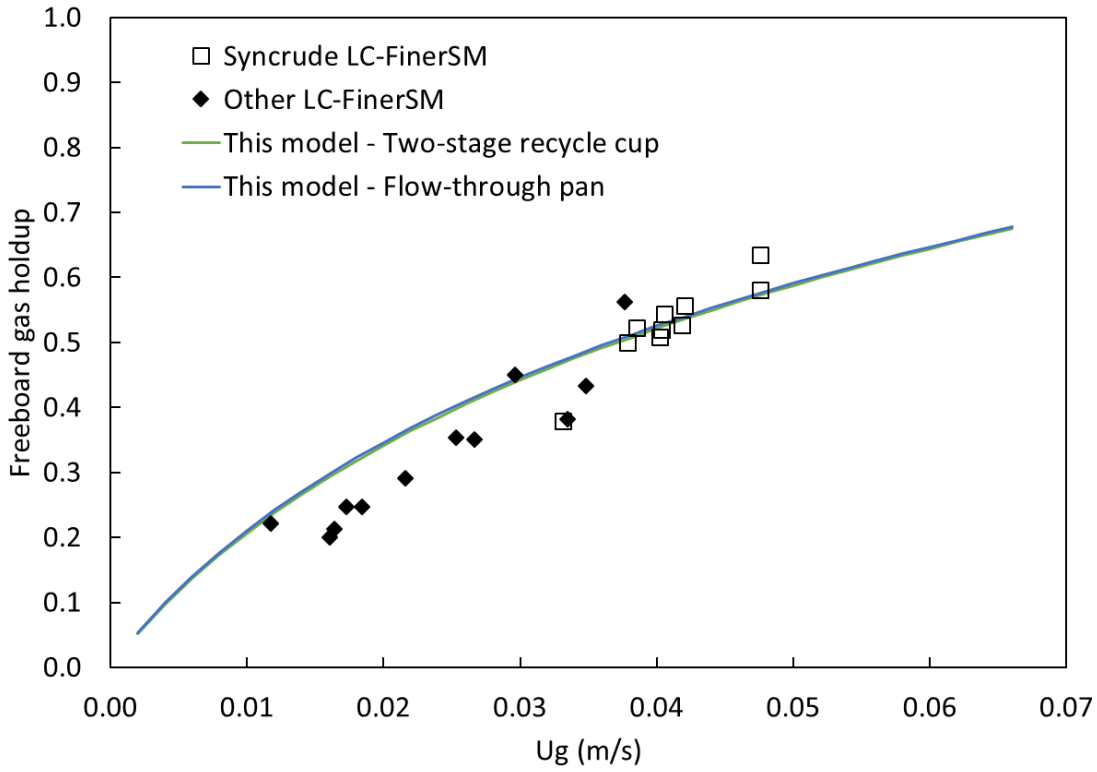

Figure 5.3.2: Comparison of freeboard gas holdup reported by McKnight et al. (2003) to predictions of the proposed model

Previous estimates for bubble diameter in an EBHR range between 0.3 mm to 1.0 mm (Grace and Zhu, 1992; Parisien, 2016). The standard operating condition of 0.04 m/s treat gas superficial velocity and 53% freeboard gas holdup were used to find the best fit for the bubble diameter. The contribution of hydrocarbon vaporization was considered, and best-fit bubble diameters for vaporization fractions of 0%, 15%, and 30% of 1.00 mm, 1.04 mm, and 1.06 mm respectively were found. These bubbles are within the range of previously estimated values. However, improved estimates are desirable as the freeboard gas holdup proved to be sensitive to the selected bubble diameter. Consistent with the gas holdup correlation reported by Eccles et al. (1993) for a coal liquefaction ebullated bed reactor, when the vaporization fraction was above zero, a minimum gas fraction was found as treat gas superficial velocity

went to zero. For all other model simulations, a vaporization fractions of 0% and a bubble diameter of 1.00 mm is assumed.

Both the flow-through pan and two-stage recycle cup configurations are compared to the commercial data demonstrating the freeboard gas holdup reduction as a result of the recycle pan configuration. For a treat gas superficial velocity of 0.04 m/s, the flow-through pan is predicted to decrease the gas holdup from 60% to 53%. For treat gas superficial velocities above 0.068 m/s, no steady-state solution was found. This was a result of the solver being unable to match the fluidized bed height set point. At this treat gas flow rate, gas holdup displaces liquid thereby increasing the liquid interstitial velocity. Without any liquid recycle, the feed liquid flow rate is sufficient to expand the bed above the set point. Higher gas velocities are achievable but require a reduction of feed liquid flow rate or catalyst inventory.

It is noted that, for other LC-Finer^{SM} units, this model appears to consistently over-predict the reported freeboard gas holdup. However, unit specific parameters are unknown (catalyst properties and inventory, recycle pan configuration, liquid flow rates, etc.). Due to the limited commercial data available, this data set is included to provide insight into the overall trend between freeboard gas holdup and treat gas superficial velocity.

5.3.3 Response to Changes in Treat Gas Flow Rate

Two trials conducted by Syncrude, where the LC-Finer^{SM} system response to a change in treat gas superficial velocity was recorded are simulated using the fluid dynamic model. A comparison of these two studies is presented in Figure 5.3.3 and Figure 5.3.4 corresponding to a two-stage recycle cup and flow-through pan configurations, respectively.

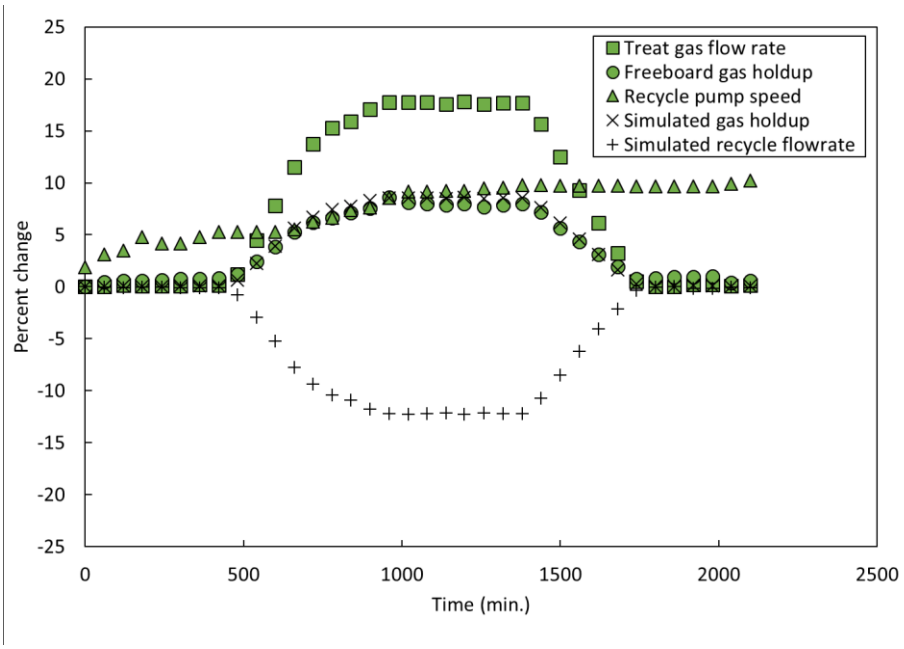

Figure 5.3.3: Comparison of numerical model predictions to experimental measurements of system response to an increase in treat gas flow rate in an LC-Finer^{SM} two-stage recycle cup.

The freeboard gas holdup response to the change in treat gas flow rate is well predicted by the proposed fluid model. The predicted change in gas holdup is generally within 1 percentage point of the reported value. A 14% reduction in recycle flow rate (combined gas-liquid flow) is predicted by the model. However, the experimental data indicates pump RPM continuously increased over the duration of the trial. A 10% increase in pump RPM is observed after the treat gas flow rate returns to its original value. It is possible that the system experienced a process upset or some other transient process during this trial.

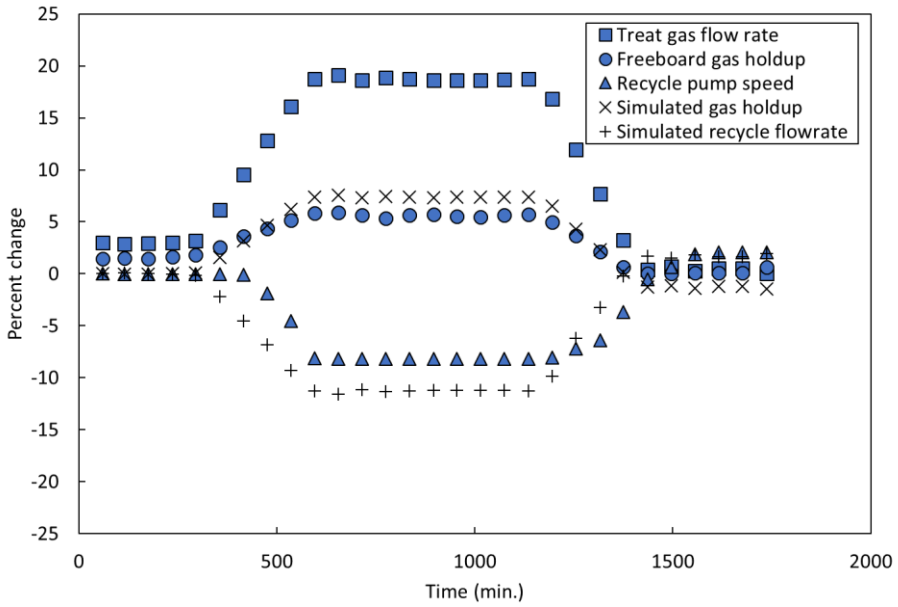

Figure 5.3.4: Comparison of numerical model predictions to experimental measurements of system response to an increase in treat gas flow rate in an LC-Finer^{SM} flow-through pan.

A similar trial was reported for the flow-through pan configuration. The freeboard gas holdup response for this trial is also well predicted by the presented model. It is noted that the model overpredicts by approximately 2 percentage points as the new steady state is reached. In contrast to the two-stage recycle cup trial, pump RPM decreases by 8% with an increase in treat gas flow rate of 18%. The model estimates a reduction in the recycle flowrate of 12% for the same increase in treat gas flow rate. The pump response to the increase in treat gas flow rate for the flow-through pan trial is also as expected. An increase in superficial gas velocity increases bed region gas holdup, displacing the liquid phase and thereby increasing the liquid interstitial velocity. Due to this increase in liquid interstitial velocity, a lower liquid flow rate in the fluidized bed region is required to maintain bed expansion, thus requiring less recycled liquid and lower pump RPM.

5.3.4 Effects of Treat Gas Flow Rate on Gas Recycle

The hydrogen partial pressure in the gas phase at the distributor grid is a function of the ratio of feed hydrogen to recycled hydrogen. An increase in the recycled gas fraction results in lower partial pressure due to the presence of volatile hydrocarbon contaminants. Reduction of hydrogen treat gas partial pressure in an EBHR due to the presence of volatile hydrocarbon components both increases gas phase holdup and decreases dissolved hydrogen, in both cases negatively impacting reactor performance (Chávez et al., 2014; Gauthier et al., 2007). The fraction of recycled gas flow to treat gas flow for standard conditions and varying liquid and gas flow rates is presented in Figure 5.3.5.

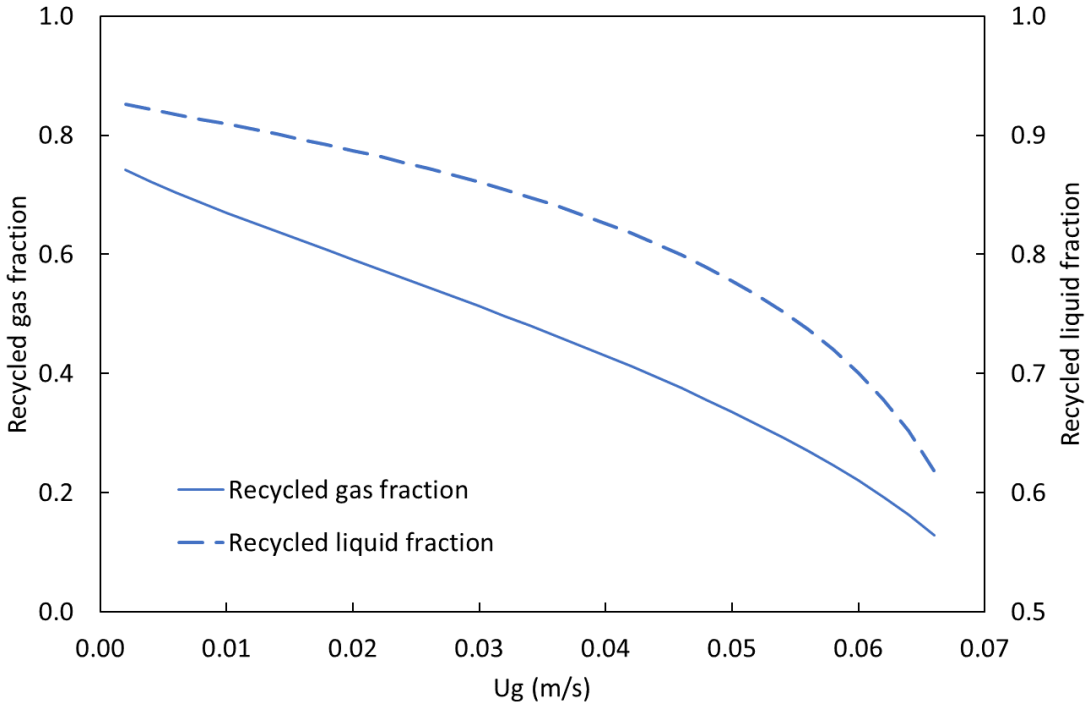

Figure 5.3.5: Model predictions for the fraction of recycled gas to feed treat gas and recycle fraction.

The recycled gas fraction for both the flow-through pan and two-stage recycle cup decreases in a nearly linear relation to the treat gas superficial velocity. This corresponds to a reduction in the recycle fraction of the liquid phase. As the treat gas flow rate is reduced, the lower gas

holdup in the fluidized bed reduced liquid interstitial velocity. Therefore, the additional recycled liquid is required to maintain bed expansion at the set point. This is consistent with previously published observations of a commercial unit where a reduction of the hydrogen treat gas flow rate required an increase in pump RPM to maintain bed expansion (McKnight et al., 2003).

The feedstock for an LC-Finer[SM] has high concentrations of asphaltenes due to the removal of lighter components at the upstream distillation towers. Asphaltenes are extremely high molecular weight, n-heptane insoluble, molecules that are known to oligomerize and precipitate from the liquid as a mesophase which cokes and deposits within, and downstream of, the hydroprocessor (Gawel et al., 2005). To inhibit the rate of asphaltene compound oligomerization, thereby reducing the overall rate of its deposition, hydrogenation of free radical hydrocarbons must be promoted (Sanford, 1995). Hydrogenation promotion is achieved through the increased concentration of dissolved hydrogen in the liquid phase. Through the removal of volatile hydrocarbon products from the reactor, the hydrogen partial pressure can be increased, thereby promoting the hydrogenation of free radical hydrocarbons and reducing the rate of asphaltene polymerization and deposition. As can be seen from Figure 5.3.5, operation at increased treat gas flow rates is expected to increase hydrogen partial pressure through a reduction of recycled gas. Further improvement in the separation efficiency of the recycle pan provides the opportunity to operate a lower treat gas flow rates without reducing hydrogen partial pressure.

5.3.5 Effects of Catalyst Inventory on Gas Recycle

The catalyst inventory is assumed to be the initial inventory after a start-up. Due to continual catalyst additions and withdrawals, and the inability to take direct measurements, there is error

associated with the assumed catalyst inventory. The sensitivity of the model to catalyst inventory is presented in Figure 5.3.6.

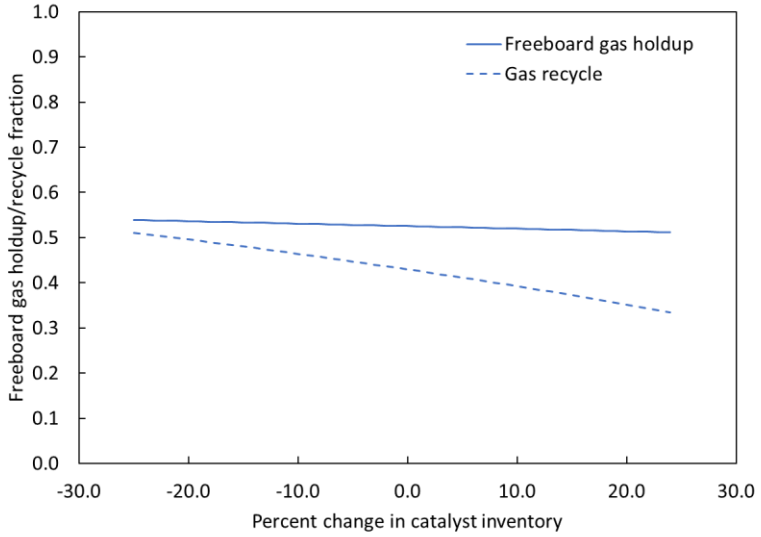

Figure 5.3.6: Sensitivity of freeboard gas holdup and gas recycle fraction to catalyst inventory.

No significant change in freeboard gas holdup is observed over a range of 0.75x to 1.25x of the initial inventory. However, a reduction in recycle fraction with an increase in catalyst inventory is observed. The addition of catalyst inventory reduced the required bed expansion for an equivalent bed height. This reduces the internal fluid recycle requirement, decreasing the recycled gas fraction.

5.4 Conclusions

A novel numerical model for estimating phase holdups and the liquid residence time in a commercial ebullated bed hydroprocessor is presented. This model incorporates the effects of a recycle pan and gas entrainment to assess the impacts on reactor fluid dynamics. The liquid phase axial dispersion model verifies previous CSTR model assumptions for the liquid RTD for commercial scale geometry and flow rates. Gas holdup model predictions are compared to previously reported commercial data. An improved gas holdup estimate is

demonstrated for two recycle pan configurations, the two-stage recycle cup and flow-through pan. A decrease of recycled gas with an increase in treat gas flow rate is observed increasing hydrogen partial pressure at the distributor grid. This is desirable as increasing the hydrogen partial pressure is favourable given the reaction kinetics. The flow-through pan configuration is estimated to provide a 7% reduction in recycled gas and 8% reduction in reactor gas holdup in comparison to the two-stage pan configuration. Improvements to the separation performance of the internal recycle pan are therefore expected to provide additional benefit to commercial ebullated bed hydroprocessing reactors. This fluid model provides a utility for industry to improve their operations through more accurate estimates of relevant process parameters and improved understanding of system dynamics.

6 Conclusions

The objective of this doctoral thesis was to improve the understanding of ebullated bed hydroprocessors through fluid dynamic modeling. The approach taken combined both numerical and experimental investigations to provide insight into how the gas-liquid separation process in an ebullated bed hydroprocessor impacts overall reactor gas holdup and fluidization behavior.

An initial parametric analysis of a first generation recycle pan, the two-stage recycle cup, using CFD, provided insight into the dynamic fluid behavior of the multiphase flow in the separation region of the reactor. A sensitivity analysis of gas separation to the operational parameters fluid velocity, column gas holdup, recycle fraction, and bubble diameter was conducted. The dependence of gas separation on these parameters found that a liquid residence timescale was suitable for the estimation of separation efficacy from operational parameters. Previous studies of the gas holdup in these units have suggested the presence of effervescent foam. By assuming a non-coalescing flow, a bubble-bubble packing limiter was implemented to investigate the performance impact of foam generation. Significant separation efficiency reductions were observed for simulations where disengaged gas exceeded the foam packing limit. Simulation results, for which various drag correlations were implemented, determined that an accurate quantification of the separation efficiency was dependent on a drag correlation validated for fluid conditions representative of a commercial ebullated bed reactor.

Based on the sensitivity of the initial CFD simulation work, an experimental investigation of the drag effects on bubbles traveling in a swarm at elevated pressure in a contaminated system was conducted. This study evaluated the most appropriate drag correlation for use in the CFD

of bubble disengagement. Using a novel analysis methodology to determine the swarm drag coefficient of individual bubbles within a swarm, the following conditions were investigated:

1. High gas holdup (>5%)
2. Small to medium bubble sizes (0.1 mm < d_b < 10 mm)
3. Atmospheric and elevated pressure (0.1 to 6.5 MPa)
4. Polydisperse bubble flow

This work contributed to the relatively limited data for drag coefficients of bubble swarms in a contaminated system at elevated pressure. It is the first such publication to investigate the effective drag coefficient on individual bubbles within a polydisperse bubble swarm. Additionally, this investigation provided important insight into the effects of drag on small bubbles (<1 mm) in swarms previously not reported on. Analysis of the atmospheric pressure experimental results found the swarm correction factor of Lockett and Kirkpatrick (1975), applied to the single bubble drag coefficient of Tomiyama et al., provided a good fit while at elevated pressure (6.5 MPa) no swarm correction was required.

Two unique industrial separator pan configurations were compared to a no-pan configuration leveraging the previously developed CFD approach. Using the drag correlation as experimentally determined, CFD separation results were compared to pilot plant gas disengagement measurements. CFD modeling of the multiphase separation process was found to predict correctly the performance ranking of each internal geometry configuration. Analysis of the grade separation curves, estimated by CFD, for each configuration suggests that the enhanced performance of the flow-though recycle pan geometry realitie to the two-stage recycle cup and no-pan configuration is primarily due to the improved separation of the

larger bubbles classes (>1 mm). No significant difference in separation efficiency for small bubbles (<1 mm) was predicted. Observing the internal flow patterns and structures predicted by CFD in addition to analysis of the RTD are consistent with this hypothesis as increased flow short-circuiting was observed in both the no-pan and two-stage recycle cup configurations. While the flow-through pan also exhibited similar short-circuiting, the reduction of low residence time liquid flow promoted the separation of larger bubble diameters. Small bubble sizes, however, did not benefit from this narrowing of the liquid RTD to the same extent and therefore larger bubbles experience preferential separation performance improvement providing insight for future separator designs.

The performance impact of the separation geometry on the overall fluid dynamics of an ebullated bed hydroprocessor was found through the development of an integrated modeling approach. A novel numerical model, incorporating recycled gas estimates using the previously validated correlation was developed and compared to previously reported commercial data. Effects of gas entrainment for both the flow-through recycle pan and two-stage recycle cup geometries integrated with a fluidization model for the region of the reactor. This model provides improved estimated on overall gas holdup within ebullated bed hydroprocessors, and therefore the liquid residence time estimate.

6.1 Recommendations for future work

Modeling of the gas-liquid separation region using CFD provided gas-liquid separation estimates and insight into the performance of the hydroprocessor internal separator geometries. A preliminary investigation on the effects of foaming was carried out assuming an upper and lower bound on the coalescence rate of the gas bubbles. While a significant impact on separation efficiency was predicted by CFD, this finding has not been

experimentally validated. Little is known about the potential foaming conditions within an ebullated bed hydroprocessor, making a prediction of foam generation rates in the separation region difficult. Due to potentially performance-limiting impact of foam generation, a bench scale investigation of the foaming characteristics of hydrogen and hydrocarbons at the operational temperature and pressure of an ebullated bed hydroprocessor is required to estimate the effects of foam on the ebullated bed hydroprocessor fluid dynamics.

Studies on the drag coefficient of individual bubble size classes within a bubble swarm at both low and high pressure revealed interesting results. At low pressure, an improved single bubble model was found using a simple piecewise function. Many authors have published data at high holdup conditions and provided swarm corrections to individual bubble drag coefficients. However, the effects of polydisperse swarms at high gas holdup conditions requires additional attention. Further, momentum coupling models, for which the gas-liquid systems of interest do not provide an ideal framework for implementation into CFD solvers. A novel theoretical model which extend the momentum coupling of drag on single bubbles at low gas holdup to the generation of foam at high gas holdup would be highly desirable for the CFD simulation of gas-liquid processes which span a large range of gas holdups.

Comparison of the CFD estimate for separation performance to pilot plant data and the integrated fluid dynamic model for an ebullated bed hydroprocessor to commercial gas holdup data both revealed a dependence on bubble size. While previous investigations into the estimated bubble diameter within an ebullated bed hydroprocessor have given estimates in the submillimeter range, the gas holdup and fluid dynamics of an ebullated bed hydroprocessor are sensitive to this parameter. Direct measurements of the mean bubble size are unavailable and, due to the high temperatures and pressure and associated construction requirements of

these reactors, direct measurement is difficult. For practical estimation of gas holdup and system fluid dynamic response prediction, it is recommended that industrial holdup measurements of a commercial scale unit be used to correlate an appropriate bubble size. Future work is required to elucidate the fundamental principles surrounding the bubble generation processes. Specifically, the distributor grid is known to play an important role in the determination of the bubble size distribution. However, no previous literature has provided a methodology to estimate the expected bubble size distribution generated by the grid. Future research to provide clarity into the gas-liquid dynamics of the grid and distributor region provide a more robust and thorough understanding of ebullated bed hydroprocessor fluid dynamics.

The focus of this thesis was to model the gas holdup within an ebullated bed hydroprocessor. Specifically, to investigate the impact of entrained gas on overall performance and phase holdups. Conclusions from the CFD and experimental work suggest that further improvement to gas separation and therefore overall reactor performance can be achieved through improved separating geometry designs. Future separator designs should focus on the separation of large bubbles, through geometries which provide narrow liquid residence time distributions. Edges and protrusions induce recirculation and flow short-circuiting and therefore should be avoided. Pan placement and recycle line dimensions should be optimized to maximize both volume available for the fluidized catalyst and gas-liquid separation. In addition, the feasibility of implementing a centrifugal type separation technology (cyclone separators and swirl tubes) should be assessed in severe conditions and fouling within an ebullated bed hydroprocessor should be investigated. Finally, future grid and distributor designs should be investigated. Gas holdup and separation dynamics were found to be sensitive to the bubble diameter in the freeboard region. Improved distributor grid designs

which increase bubble diameter are favorable to the overall gas separation and reactor performance.

References

Acuña, C.A., and Finch, J.A. (2010). Tracking velocity of multiple bubbles in a swarm. International Journal of Mineral Processing *94*, 147-158.

Ancheyta, J. (2013). Modeling of Processes and Reactors for Upgrading of Heavy Petroleum (CRC Press).

Auton, T.R. (1981) (Cambridge, U.K.: University of Cambridge).

Behzadi, A., Issa, R.I., and Rusche, H. (2004). Modelling of dispersed bubble and droplet flow at high phase fractions. Chemical Engineering Science *59*, 759-770.

Bridge, A., Lapidus, L., and Elgin, J. (1964a). The mechanics of vertical gas–liquid fluidized system. Part I: countercurrent flow. AIChE Journal *10*, 819–826.

Bridge, A.G., Lapidus, L., and Elgin, J.C. (1964b). The Mechanics of Vertical Gas-Liquid Fluidized Systems I: Countercurrent Flow. AIChE Journal *10*, 819.

Buttke, R.D., and Frey, J.R. (1989). Process for Collecting Vapor in Ebullated Bed Reactors, U.S.P. Office, ed. (United States: Amoco Corporation), pp. 5.

Buwa, V.V., and Ranade, V.V. (2002). Dynamics of gas–liquid flow in a rectangular bubble column: experiments and single/multi-group CFD simulations. Chemical Engineering Science *57*, 4715-4736.

Chávez, L.M., Alonso, F., and Ancheyta, J. (2014). Vapor–liquid equilibrium of hydrogen–hydrocarbon systems and its effects on hydroprocessing reactors. Fuel *138*, 156-175.

Cheng, Z.-M., Huang, Z.-B., Yang, T., Liu, J.-K., Ge, H.-L., Jiang, L.-J., and Fang, X.-C. (2014). Modeling on scale-up of an ebullated-bed reactor for the hydroprocessing of vacuum residuum. Catalysis Today *220-222*, 228-236.

Clift, R., Grace, J.R., and Weber, M.E. (1978). Bubbles, Drops, and Particles (New York: Academic Press).

Cortes, C., and Gil, A. (2007). Modeling the gas and particle flow inside cyclone separators. Progress in Energy and Combustion Science *33*, 409-452.

Davidson, J., and Harrison, D. (1966a). The behavior of a continuity bubbling fluidized bed. Chemical Engineering Science *21*, 731-738.

Davidson, J.F., and Harrison, D. (1966b). The behaviour of a continuously bubbling fluidised bed. Chemical Engineering Science *21*, 731-738.

de Swart, J.W.A., and Krishna, R. (2002). Simulation of the transient and steady state behaviour of a bubble column slurry reactor for Fischer–Tropsch synthesis. Chemical Engineering and Processing: Process Intensification *41*, 35-47.

Devanathan, N., McKnight, C.A., VanderHeyden, W.B., Hackman, L.P., Klomans, P.J., and Skwarok, R.W. (1997). Hydrocarbon processing apparatus (Google Patents).

Dijkhuizen, W., Roghair, I., Van Sint Annaland, M., and Kuipers, J.A.M. (2010). DNS of gas bubbles behaviour using an improved 3D front tracking model—Drag force on isolated bubbles and comparison with experiments. Chemical Engineering Science *65*, 1415-1426.

Dijkhuizen, W., Sint Annaland, M.v., and Kuipers, J.A.M. (2007). Direct numerical simulation of the drag force in bubble swarms. In 6th International Conference on Multiphase Flow, ICMF 2007 (Leipzig, Germany).

Eccles, R.M. (1993). Residue hydroprocessing using ebullated-bed reactors. Fuel Processing Technology *35*, 21-38.

Fan, L.S. (1989). Gas-Liquid-Solid Fluidization Engineering, Vol 36 (Stoneham, MA: Butterworth Publishers).

Garnier, C., Lance, M., and Marié, J.L. (2002). Measurement of local flow characteristics in buoyancy-driven bubbly flow at high void fraction. Experimental Thermal and Fluid Science *26*, 811-815.
Gauthier, T., Héraud, J.P., Kressmann, S., and Verstraete, J. (2007). Impact of vaporization in a residue hydroconversion process. Chemical Engineering Science *62*, 5409-5417.
Gawel, I., Bociarska, D., and Biskupski, P. (2005). Effect of asphaltenes on hydroprocessing of heavy oils and residua. Applied Catalysis A: General *295*, 89-94.
Grace, J.R., and Zhu, J. (1992). Understanding of the LC-Finer Hydrodynamics (University of British Columbia: Syncrude).
Griffith, P., and Wallis, G. (1961a). Two phase slug flow. Journal of Heat Transfer *83*, 307–320.
Griffith, P., and Wallis, G.B. (1961b). Two-Phase Slug Flow. Journal of Heat Transfer *83*, 307.
Guitian, J., and Joseph, D. (1998). How bubbly mixtures foam and foam control using a fluidized bed. International Journal of Multiphase Flow *24*, 1-16.
Gupta, A., and Roy, S. (2013). Euler–Euler simulation of bubbly flow in a rectangular bubble column: Experimental validation with Radioactive Particle Tracking. Chemical Engineering Journal *225*, 818-836.
Haider, A., and Levenspiel, O. (1989). Drag coefficient and terminal velocity of spherical and nonspherical particles. Powder Technology *58*, 63-70.
Hoffmann, A.C., and Stein, L.E. (2007). Gas Cyclones and Swirl Tubes, Second Edition edn (Springer).
Ishibashi, H., Onozaki, M., Kobayashi, M., Hayashi, J.i., Itoh, H., and Chiba, T. (2001). Gas holdup in slurry bubble column reactors of a 150t/d coal liquefaction pilot plant process. Fuel *80*, 655-664.
Jakubowski, M., Sterczyska, M., Matysko, R., and Poreda, A. (2014). Simulation and experimental research on the flow inside a whirlpool separator. Journal of Food Engineering *133*, 9-15.
Khan, A.R., and Richardson, J.F. (2007). Fluid-Particle Interactions and Flow Characteristics of Fluidized Beds and Settling Suspensions of Spherical Particles. Chemical Engineering Communications *78*, 111-130.
Krishna, R., De Swart, J.W.A., Ellenberger, J., Martina, G.B., and Maretto, C. (1997). Gas holdup in slurry bubble columns: Effect of column diameter and slurry concentrations. AIChE Journal *43*, 311-316.
Krishna, R., Urseanu, M.I., and Dreher, A.J. (2000). Gas hold-up in bubble columns: influence of alcohol addition versus operation at elevated pressures. Chemical Engineering and Processing: Process Intensification *39*, 371-378.
Lane, C.D., McKnight, C.A., Wiens, J., Reid, K., and Donaldson, A.A. (2016). Parametric analysis of internal gas separation within an ebullated bed reactor. Chemical Engineering Research and Design *105*, 44-54.
Leonard, C., Ferrasse, J.H., Boutin, O., Lefevre, S., and Viand, A. (2015). Bubble column reactors for high pressures and high temperatures operation. Chemical Engineering Research and Design *100*, 391-421.
Lin, T.J., Tsuchiya, K., and Fan, L.S. (1998). Bubble flow characteristics in bubble columns at elevated pressure and temperature. AIChE Journal *44*, 545-560.
Lockett, M., and Kirkpatrick, R. (1975a). Ideal bubbly flow and actual flow in bubble columns. Transactions of the Institution of Chemical Engineers *53*, 267–273.
Lockett, M.J., and Kirkpatrick, R.D. (1975b). Ideal Bubbly Flow and Actual Flow in Bubble Columns. Transactions of the Institution of Chemical Engineers *53*.
Macchi, A., Bi, H., Grace, J.R., McKnight, C.A., and Hackman, L. (2001). Dimensional hydrodynamic similitude in three-phase fluidized beds. Chemical Engineering Science *56*, 6039-6045.

Marrucci, G. (1965a). Rising Velocity of a Swarm of Sphereical Bubbles. I&EC Fundamentals, 224.
Marrucci, G. (1965b). Rising velocity of a swarm of spherical bubbles. Industrial and Engineering Chemistry Research Fundamentals *4*, 224–225.
Martínez, J., Sánchez, J.L., Ancheyta, J., and Ruiz, R.S. (2010). A Review of Process Aspects and Modeling of Ebullated Bed Reactors for Hydrocracking of Heavy Oils. Catalysis Reviews *52*, 60-105.
McKnight, C.A., Hackman, L.P., Grace, J.R., Macchi, A., Kiel, D., and Tyler, J. (2003). Fluid dynamic studies in support of an industrial three-phase fluidized bed hydroprocessor. Can J Chem Eng *81*, 338-350.
Michaelides, E.E. (2006). Particles, Bubbles & Drops - Their Motion, Heat and Mass Transfer (Singapore: World Scientific Publishing Co. Pte. Ltd.).
Moradian, N., Ting, D.S.K., and Cheng, S. (2009). The effects of freestream turbulence on the drag coefficient of a sphere. Experimental Thermal and Fluid Science *33*, 460-471.
Neesse, T., and Dueck, J. (2007). Dynamic modelling of the hydrocyclone. Minerals Engineering *20*, 380-386.
Owen, N.A., Inderwildi, O.R., and King, D.A. (2010). The status of conventional world oil reserves—Hype or cause for concern? Energy Policy *38*, 4743-4749.
Pang, M.J., and Wei, J.J. (2011). Analysis of drag and lift coefficient expressions of bubbly flow system for low to medium Reynolds number. Nuclear Engineering and Design *241*, 2204-2213.
Parisien, V. (2016). Impact of bubble characteristics and particle properties on the fluid dynamics of an ebullated bed hydroprocessor. In Chemical and Biological Engineering (Ottawa, Ontario: University of Ottawa), pp. 66.
Pjontek, D., McKnight, C.A., Wiens, J., and Macchi, A. (2015). Ebullated bed fluid dynamics relevant to industrial hydroprocessing. Chemical Engineering Science *126*, 730-744.
Pjontek, D., Parisien, V., and Macchi, A. (2014). Bubble characteristics measured using a monofibre optical probe in a bubble column and freeboard region under high gas holdup conditions. Chemical Engineering Science *111*, 153-169.
Richardson, J.F., and Zaki, W.N. (1954). The sedimentation of a suspension of uniform spheres under conditions of viscous flow. Chemical Engineering Science *3*, 65-73.
Roghair, I., Baltussen, M.W., Van Sint Annaland, M., and Kuipers, J.A.M. (2013a). Direct Numerical Simulations of the drag force of bi-disperse bubble swarms. Chemical Engineering Science *95*, 48-53.
Roghair, I., Lau, Y.M., Deen, N.G., Slagter, H.M., Baltussen, M.W., Van Sint Annaland, M., and Kuipers, J.A.M. (2011). On the drag force of bubbles in bubble swarms at intermediate and high Reynolds numbers. Chemical Engineering Science *66*, 3204-3211.
Roghair, I., Van Sint Annaland, M., and Kuipers, H.J.A.M. (2013b). Drag force and clustering in bubble swarms. AIChE Journal *59*, 1791-1800.
Rollbusch, P., Bothe, M., Becker, M., Ludwig, M., Grünewald, M., Schlüter, M., and Franke, R. (2015). Bubble columns operated under industrially relevant conditions – Current understanding of design parameters. Chemical Engineering Science *126*, 660-678.
Romanova, U.G., Valinasab, M., Stasiuk, E.N., Yarranton, H.W., Schramm, L.L., and Shelfantook, W.E. (2013). The Effect of Oil Sands Bitumen Extraction Conditions on Froth Treatment Performance. Journal of Canadian Petroleum Technology *45*.
Ruiz, R.S., Alonso, F., and Ancheyta, J. (2005). Pressure and temperature effects on the hydrodynamic characteristics of ebullated-bed systems. Catalysis Today *109*, 205-213.
Saffman, P.G. (1956). The lift on a small sphere in a slow shear flow. Chemical Engineering Science *1*, 249-275.

Safoniuk, M., Grace, J.R., Hackman, L., and McKnight, C.A. (1999). Use of dimensional similitude for scale-up of hydrodynamics in three-phase fluidized beds. Chemical Engineering Science *54*, 4961-4966.
Sahu, R., Song, B.J., Im, J.S., Jeon, Y.-P., and Lee, C.W. (2015). A Review of Recent Advances in Catalytic Hydrocracking of Heavy Residues. Journal of Industrial and Engineering Chemistry.
Sanchez, J., Ruiz, R., Alonso, F., and Ancheyta, J. (2008). Evaluation of the hydrodynamics of high-pressure ebullated beds based on dimensional similitude. Catalysis Today *130*, 519-526.
Sanford, E.C. (1995). Conradson Carbon Residue Conversion during Hydrocracking of Athabasca Bitumen: Catalyst Mechanism and Deactivation. Energy & Fuels *9*, 549-559.
Schubert, H. (2010). Which demands should and can meet a separation model for hydrocyclone classification? International Journal of Mineral Processing *96*, 14-26.
Schweitzer, J.-M., and Kressmann, S. (2004). Ebullated bed reactor modeling for residue conversion. Chemical Engineering Science *59*, 5637-5645.
Shah, Y.T., Kelkar, B.G., Godbole, S.P., and Deckwer, W.D. (1982). Design parameters estimations for bubble column reactors. AIChE Journal *28*, 353-379.
Simonnet, M., Gentric, C., Olmos, E., and Midoux, N. (2007). Experimental determination of the drag coefficient in a swarm of bubbles. Chemical Engineering Science *62*, 858-866.
Tabib, M.V., Roy, S.A., and Joshi, J.B. (2008). CFD simulation of bubble column—An analysis of interphase forces and turbulence models. Chemical Engineering Journal *139*, 589-614.
Tarmy, B., Chang, M., Coulaloglou, C., and Ponzi, P. (1984). The three phase hydrodynamic characteristics of the EDS coal liquefaction reactors: their development and use in reactor scaleup. Paper presented at: Internat Symp on Chem Reac Eng, Sept.
Tomiyama, A. (1998a). Struggle with computational bubble dynamics. Multiphase Science and Technology, Vol 10 Issue 4 1998 *10*, 369-405.
Tomiyama, A. (1998b). Struggle with computational bubble dynamics. Paper presented at: Third International Conference on Multiphase Flow (Lyon: ICMF'98).
Torobin, L.B., and Gauvin, W.H. (1960). Fundamental aspects of solids-gas flow: Part V: The effects of fluid turbulence on the particle drag coefficient. The Canadian Journal of Chemical Engineering *38*, 189-200.
Van Wachem, B. (2000). Derivation, Implementation, and Validation of Computer Simulation Models for Gas-Solid Fluidized Beds (Delft, Netherlands: Delft University of Technology).
Wang, D.M. (1994). Modelling of bubbly flow in a sudden pipe expansion (BRITE/EURAM II (BE 4098)), pp. II-34.
Xiao, Q., Yang, N., and Li, J. (2013). Stability-constrained multi-fluid CFD models for gas–liquid flow in bubble columns. Chemical Engineering Science *100*, 279-292.

Appendix A: Description of CFD simulations

ACENET

All CDF simulations were conducted using the ACENET high performance computing cluster. The open-source CFD software OpenFOAM 2.2.0 was used for all simulations. CFD simulations were carried out on the ACENET cluster processors, typically AMD Opteron-based machines running Red Hat Enterprise Linux (RHEL) 4. Test cases were executed on a local machine, an Intel® Core™ i7 Xenon processor (3.3 GHz) running the Ubuntu 12.10 operating system. The approximate run time for a case to complete was 50 hours on the local machine. Additional information regarding the use of the ACENET computational cluster can be found in the ACENET users guide (https://www.ace-net.ca/wiki/User_Guide).

OpenFOAM

The CFD software OpenFOAM was employed throughout this study. OpenFOAM was selected for its open source software licence and the ability to manipulate source code. The version of OpenFOAM used throughout this study (2.2.0) can be found in the OpenFOAM repository which, at the time of publication, is located at http://openfoam.org/.

Mesh generation

Mesh grids were generated using a combination of Altair HyperMesh, and snappyHexMesh. For the two-stage recycle cup the entire simulated domain was meshed using Hyperworks. For the flow-through pan the initial domain was constructed in HyperMesh consisting of ~50 000 hex cells. The resulting cell mesh has the inlet pipe removed from it using the OpenFOAM snappyHexMesh utility. Figure A.1 and A.2 illustrate a cross-section of the original and final meshes used for this study.

Mesh dimensions

The following table provides a summary of key geometric dimensions used for generation of the CFD cell mesh. Additional geometry details are found in the cited patent documentation.

Table A.1: Geometric dimensions for the two-stage recycle pan and flow-through pan mesh geometries.

Parameter	Value	Units
Column diameter	1.2	m
Recycle line diameter	0.26	m
Product line diameter	0.26	m
Inlet pipe diameter	0.102	m
Dome radius of curvature	0.6	m

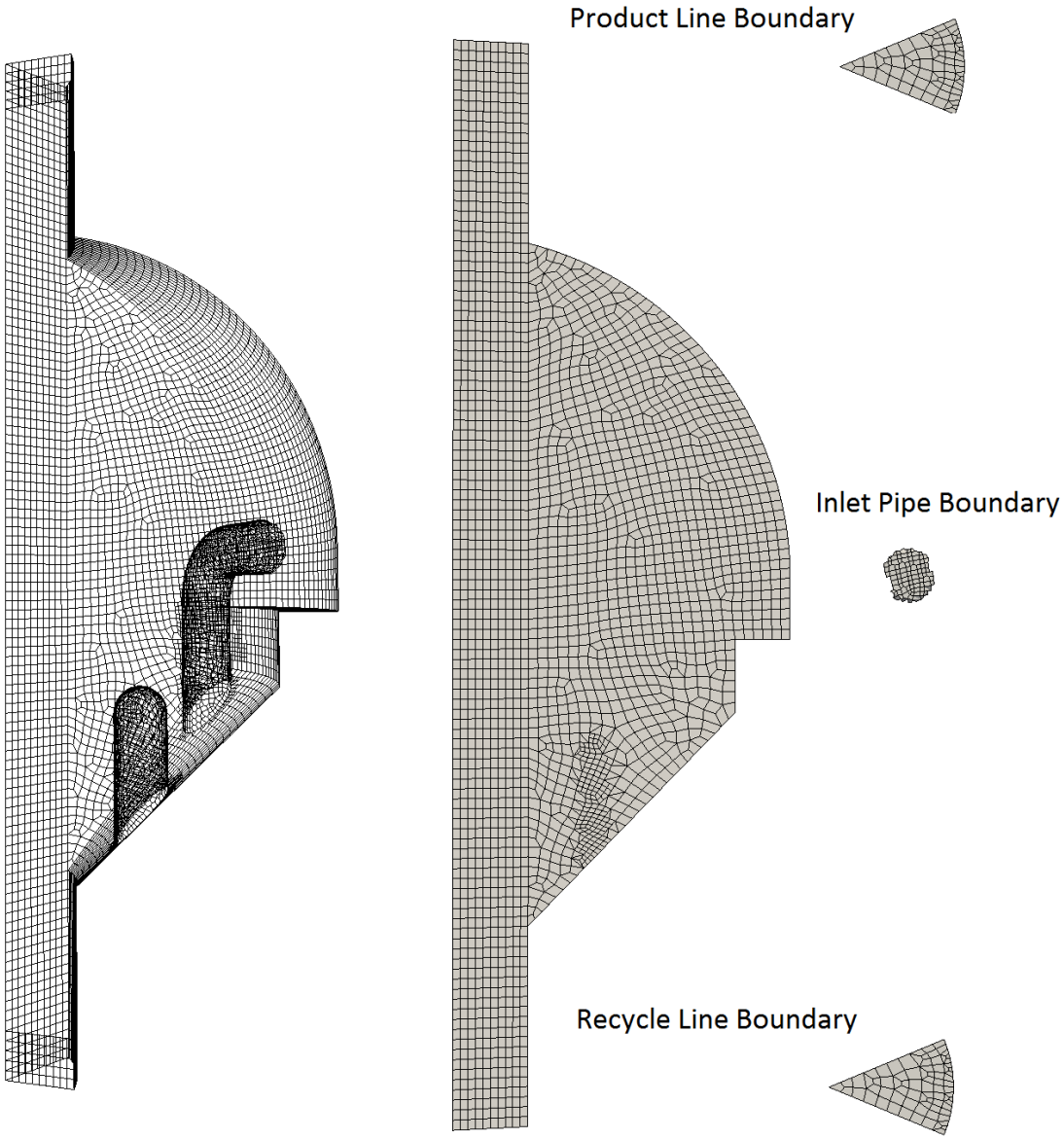

Figure A.1: Flow-through pan mesh detail.

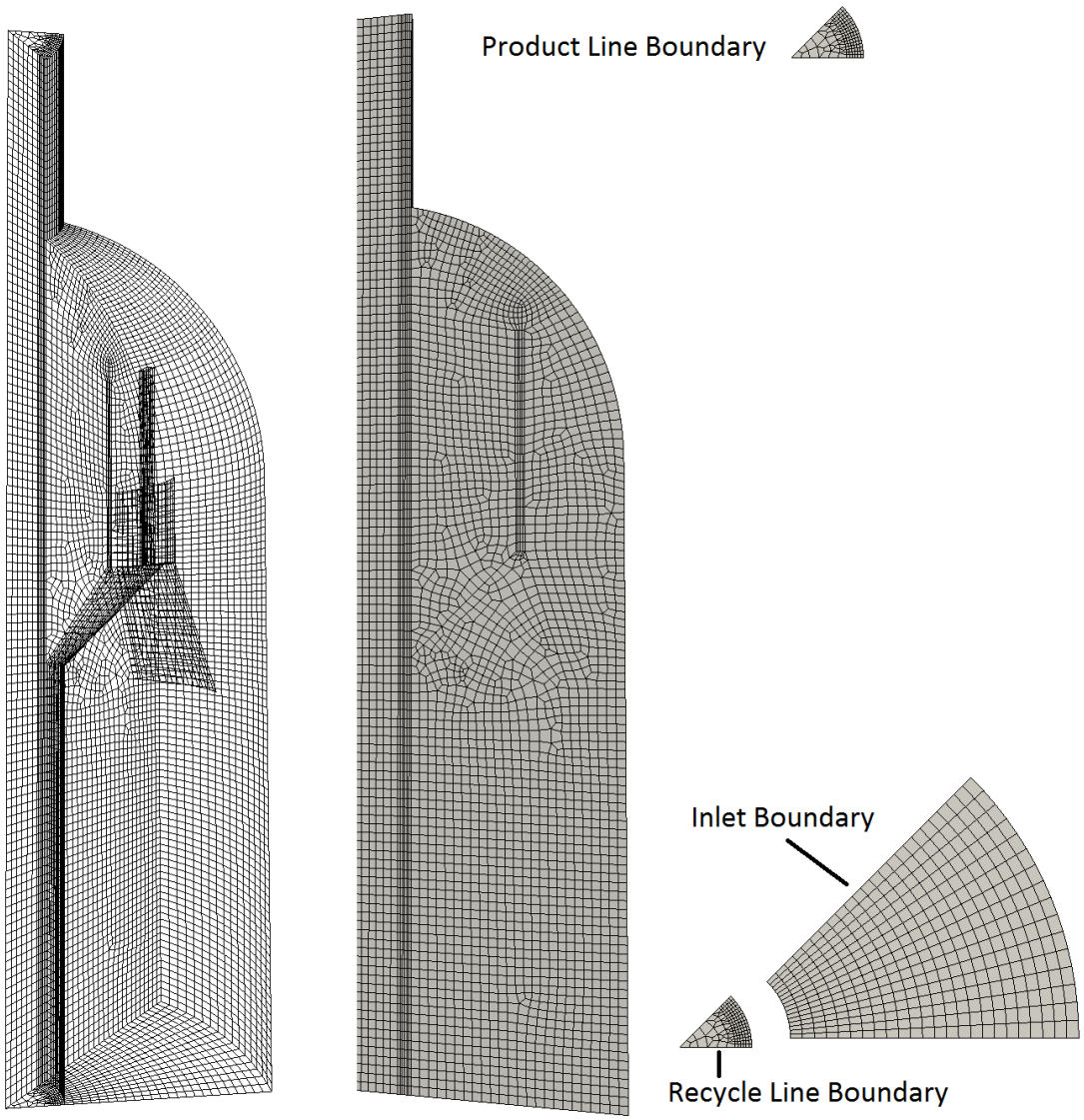

Figure A.2: Two-stage recycle cup mesh detail.

OpenFOAM case setup

The *OpenFOAM 2.2.0* solver *twoPhaseEulerFoam* was used throughout this study. A summary of settings and parameters follows. Additional details on these solvers and required input

parameters can be found in the OpenFOAM user's manual (http://foam.sourceforge.net/docs/Guides-a4/UserGuide.pdf).

createPatchDict

The ebullated bed reactor internal geometry of the separation region was modeled as a 45 degree wedge geometry. A cyclic boundary condition was implemented on both wedge faces. An arbitrary mesh interface was selected as mesh elements on either side of the wedge did not align exactly preventing the direct cell-to-cell patch interfacing.

decomposeParDict

All simulations were run in parallel to improve execution time. The decompositions of the simulated domain onto individual computational cores was controlled through the system/decomposeParDict file. Cases were run in parallel on 8 CPU cores. The domain was partitioned with approximately equivalent cell counts in the axial (vertical) direction.

```
\*---------------------------------------------------------------
------------*/
FoamFile
{
    version     2.0;
    format      ascii;
    class       dictionary;
    location    "system";
    object      decomposeParDict;
}
// * * * * * * * * * * * * * * * * * * * * * * * * * * * * * * * * *
* * * * * * //

numberOfSubdomains 8;

method          hierarchical;
preservePatches (cyc_half0);
preservePatches (cyc_half1);

hierarchicalCoeffs
```

```
{
    n               (1 8 1);
    delta           0.00001;
    order           xyz;
}


//
*********************************************************************
******** //
```

fvSchemes

Numerical schemes implemented for the following operations are set in the system/fvSchemes:

- Gradient (gradSchemes)
- Divergence (divSchemes)
- Laplacian (laplacianSchemes)
- Interpolation (interpolationSchemes)
- Surface normal gradient (snGradSchemes)
- Fields requiring flux to be calculated (fluxRequired)

Gaussian integration was used for all numerical methods utilizing variations of linear interpolation for cell values. The interpolation scheme used is noted in the system/fvSchemes files directsly proceeding the Gauss keyword (`Gauss <interpolationScheme>`). Below the system/fvSchemes files is provided.

```
\*-----------------------------------------------------------------
------------*/
FoamFile
{
    version     2.0;
    format      ascii;
    class       dictionary;
    location    "system";
```

```
    object      fvSchemes;
}
// * * * * * * * * * * * * * * * * * * * * * * * * * * * * * * * * * *
* * * * * * //

ddtSchemes
{
    default         Euler;
}

gradSchemes
{
    default         Gauss linear;
}

divSchemes
{
    default         none;
    div(phi1,U1)    Gauss limitedLinearV 1;
    div(phi2,U2)    Gauss limitedLinearV 1;
    div(phi2,k)     Gauss limitedLinear 1;
    div(phi2,epsilon) Gauss limitedLinear 1;
    div(phi,alpha1)  Gauss limitedLinear01 1;
    div(phir,alpha1) Gauss limitedLinear01 1;
    div(phi,Theta)  Gauss limitedLinear 1;
    div(Rc1)        Gauss linear;
    div(Rc2)        Gauss linear;
}

laplacianSchemes
{
    default         none;

    laplacian(nuEff1,U1) Gauss linear corrected;
    laplacian(nuEff2,U2) Gauss linear corrected;
    laplacian(Dp,p) Gauss linear corrected;
    laplacian(alpha1PpMag,alpha1) Gauss linear corrected;
    laplacian((alpha1k*nuEff2),k) Gauss linear corrected;
    laplacian((alpha1Eps*nuEff2),epsilon) Gauss linear corrected;
// Additional Turbulence Schemes
    laplacian(DepsilonEff,epsilon) Gauss linear corrected;
    laplacian(DkEff,k) Gauss linear corrected;
}

interpolationSchemes
{
    default         linear;
}

snGradSchemes
{
    default         corrected;
```

```
}

fluxRequired
{
    default         no;
    p               ;
}


//
*********************************************************************
******** //
```

fvSolution

The algorithm used to solve the pressure equation, tolerences for cell values, and equation solver specification are set in the system/fvSolutions file. The solver implements the PIMPLE algorithm, a combination of the Pressure Implicit with Splitting of Operators (PISO) and the Semi-implicit Method for Pressure Linked Equations (SIMPLE), to iterate the pressure-velocity governing equations each simulated time step.

The pressure equation is computed using a generalised geometric-algebraic multi-grid (GAMG) solver. The phase fraction term alpha (ε) is solved using a preconditioned bi-conjugate gradient (PBiCG) solver. The system/fvSolutions file used in all simulation is provided below.

```
\*---------------------------------------------------------------
------------*/
FoamFile
{
    version     2.0;
    format      ascii;
    class       dictionary;
    location    "system";
    object      fvSolution;
}
// * * * * * * * * * * * * * * * * * * * * * * * * * * * * * * * * * *
* * * * * * //

solvers
```

```
{
    p
    {
        solver          GAMG;
        tolerance       1e-10;
        relTol          0.1;
        smoother        DIC;
        nPreSweeps      0;
        nPostSweeps     2;
        nFinestSweeps   2;
        cacheAgglomeration true;
        nCellsInCoarsestLevel 10;
        agglomerator    faceAreaPair;
        mergeLevels     1;
    }

    pFinal
    {
        $p;
        tolerance       1e-10;
        relTol          0;
    }

    alpha
    {
        solver          PBiCG;
        preconditioner  DILU;
        tolerance       1e-10;
        relTol          0.1;
    }

    alpha1Final
    {
        solver          PBiCG;
        preconditioner  DILU;
        tolerance       1e-10;
        relTol          0;
    }
}

PIMPLE
{
    nCorrectors     2;
    nNonOrthogonalCorrectors 1;
    nAlphaCorr      1;
    nAlphaSubCycles 2;
    correctAlpha    yes;
//    pRefCell        0;
//    pRefValue       0;
}

relaxationFactors
```

```
{
    "U.*"           1;
    "T.*"           1;
    "alpha1.*"      1;
    "Theta.*"       1;
    "k.*"           1;
    "epsilon.*"     1;
}


//
************************************************************************
******** //
```

interfacialProperties

The drag model for each phase is specified in the constant/interfactialProperties directory. Drag was implemented on only the dispersed gas phase, assuming no droplet-in-gas flow was present within the simulated domain. The parameter dragModel1 specifics the gas phase drag closure.

```
\*---------------------------------------------------------------------
------------*/
FoamFile
{
    version     2.0;
    format      ascii;
    class       dictionary;
    location    "constant";
    object      interfacialProperties;
}
// * * * * * * * * * * * * * * * * * * * * * * * * * * * * * * * * * *
* * * * * * //

dragModel1      TomiyamaContaminated;

dragModel2      SchillerNaumann;

dragPhase       "1";

residualSlip    0;

//
************************************************************************
******** //
```

ppProperties

The parameters for the packing limiter solid pressure model are set in constant/ppProperties.

Solids pressure is enabled by setting `packingLimiter  on;` specificing the maximum phase fraction through `alphaMax` and the coefficient of restitution using `g0`.

```
\*---------------------------------------------------------------
------------*/
FoamFile
{
    version     2.0;
    format      ascii;
    class       dictionary;
    location    "constant";
    object      ppProperties;
}
// * * * * * * * * * * * * * * * * * * * * * * * * * * * * * * *
* * * * * * //

preAlphaExp     300;

expMax          10;

alphaMax        0.8;

g0              g0 [ 1 -1 -2 0 0 0 0 ] 0.9;

packingLimiter  on;


//
****************************************************************
******** //
```

p

Recycle rate was controlled through the implementation of a dynamically controlled pressure condition on the recycle line boundary face. This condition was set in the 0/p file using a

groovyBC boundary type. Implementation of this boundary condition requires the installation of Swak4Foam release 0.2.3. The 0/p file entries associated to this pressure boundary are:

```
    outletBottom
    {

       type groovyBC;
       value           uniform 1000;
       valueExpression
"min(max(pOutlet+0.05*pOutlet*error/mag(error)*moderror,100),2000
0)";
       variables
"mInlet{pipe_inlet1}=sum(phi2*alpha2);pOutlet{outletBottom}=sum(p
*mag(Sf()))/sum(mag(Sf()));mOutlet{outletBottom}=max(sum(phi2*alp
ha2),0);recycle=0.8;error=(mag(mOutlet/mInlet)-
recycle)/recycle;moderror=mag(error);";

    }
```

Appendix B: Copyright Licenses

ELSEVIER LICENSE
TERMS AND CONDITIONS

Sep 06, 2016

This Agreement between Chris Lane ("You") and Elsevier ("Elsevier") consists of your license details and the terms and conditions provided by Elsevier and Copyright Clearance Center.

License Number	3939130101294
License date	Aug 30, 2016
Licensed Content Publisher	Elsevier
Licensed Content Publication	Chemical Engineering Research and Design
Licensed Content Title	Parametric analysis of internal gas separation within an ebullated bed reactor
Licensed Content Author	C.D. Lane,C.A. McKnight,J. Wiens,K. Reid,A.A. Donaldson
Licensed Content Date	January 2016
Licensed Content Volume Number	105
Licensed Content Issue Number	n/a
Licensed Content Pages	11
Start Page	44
End Page	54
Type of Use	reuse in a thesis/dissertation
Portion	full article
Format	electronic
Are you the author of this Elsevier article?	Yes
Will you be translating?	No
Order reference number	
Title of your thesis/dissertation	Modeling the Fluid Dynamics of a Commercial Ebullated Bed Hydroprocessor
Expected completion date	Aug 2016
Estimated size (number of pages)	136
Elsevier VAT number	GB 494 6272 12
Requestor Location	Chris Lane 311-633 W 8th Ave. Vancouver, BC V5Z 1C7 Canada Attn: Chris Lane
Total	0.00 CAD
Terms and Conditions	

INTRODUCTION

1. The publisher for this copyrighted material is Elsevier. By clicking "accept" in connection with completing this licensing transaction, you agree that the following terms and conditions apply to this transaction (along with the Billing and Payment terms and conditions established by Copyright Clearance Center, Inc. ("CCC"), at the time that you opened your Rightslink account and that are available at any time at http://myaccount.copyright.com).

GENERAL TERMS

2. Elsevier hereby grants you permission to reproduce the aforementioned material subject to the terms and conditions indicated.
3. Acknowledgement: If any part of the material to be used (for example, figures) has appeared in our publication with credit or acknowledgement to another source, permission must also be sought from that source. If such permission is not obtained then that material may not be included in your publication/copies. Suitable acknowledgement to the source must be made, either as a footnote or in a reference list at the end of your publication, as follows:
"Reprinted from Publication title, Vol /edition number, Author(s), Title of article / title of chapter, Pages No., Copyright (Year), with permission from Elsevier [OR APPLICABLE SOCIETY COPYRIGHT OWNER]." Also Lancet special credit - "Reprinted from The Lancet, Vol. number, Author(s), Title of article, Pages No., Copyright (Year), with permission from Elsevier."
4. Reproduction of this material is confined to the purpose and/or media for which permission is hereby given.
5. Altering/Modifying Material: Not Permitted. However figures and illustrations may be altered/adapted minimally to serve your work. Any other abbreviations, additions, deletions and/or any other alterations shall be made only with prior written authorization of Elsevier Ltd. (Please contact Elsevier at permissions@elsevier.com)
6. If the permission fee for the requested use of our material is waived in this instance, please be advised that your future requests for Elsevier materials may attract a fee.
7. Reservation of Rights: Publisher reserves all rights not specifically granted in the combination of (i) the license details provided by you and accepted in the course of this licensing transaction, (ii) these terms and conditions and (iii) CCC's Billing and Payment terms and conditions.
8. License Contingent Upon Payment: While you may exercise the rights licensed immediately upon issuance of the license at the end of the licensing process for the transaction, provided that you have disclosed complete and accurate details of your proposed use, no license is finally effective unless and until full payment is received from you (either by publisher or by CCC) as provided in CCC's Billing and Payment terms and conditions. If full payment is not received on a timely basis, then any license preliminarily granted shall be deemed automatically revoked and shall be void as if never granted. Further, in the event that you breach any of these terms and conditions or any of CCC's Billing and Payment terms and conditions, the license is automatically revoked and shall be void as if never granted. Use of materials as described in a revoked license, as well as any use of the materials beyond the scope of an unrevoked license, may constitute copyright infringement and publisher reserves the right to take any and all action to protect its copyright in the materials.
9. Warranties: Publisher makes no representations or warranties with respect to the licensed material.
10. Indemnity: You hereby indemnify and agree to hold harmless publisher and CCC, and their respective officers, directors, employees and agents, from and against any and all claims arising out of your use of the licensed material other than as specifically authorized pursuant to this license.
11. No Transfer of License: This license is personal to you and may not be sublicensed, assigned, or transferred by you to any other person without publisher's written permission.

12. No Amendment Except in Writing: This license may not be amended except in a writing signed by both parties (or, in the case of publisher, by CCC on publisher's behalf).
13. Objection to Contrary Terms: Publisher hereby objects to any terms contained in any purchase order, acknowledgment, check endorsement or other writing prepared by you, which terms are inconsistent with these terms and conditions or CCC's Billing and Payment terms and conditions. These terms and conditions, together with CCC's Billing and Payment terms and conditions (which are incorporated herein), comprise the entire agreement between you and publisher (and CCC) concerning this licensing transaction. In the event of any conflict between your obligations established by these terms and conditions and those established by CCC's Billing and Payment terms and conditions, these terms and conditions shall control.
14. Revocation: Elsevier or Copyright Clearance Center may deny the permissions described in this License at their sole discretion, for any reason or no reason, with a full refund payable to you. Notice of such denial will be made using the contact information provided by you. Failure to receive such notice will not alter or invalidate the denial. In no event will Elsevier or Copyright Clearance Center be responsible or liable for any costs, expenses or damage incurred by you as a result of a denial of your permission request, other than a refund of the amount(s) paid by you to Elsevier and/or Copyright Clearance Center for denied permissions.

LIMITED LICENSE

The following terms and conditions apply only to specific license types:
15. **Translation**: This permission is granted for non-exclusive world **English** rights only unless your license was granted for translation rights. If you licensed translation rights you may only translate this content into the languages you requested. A professional translator must perform all translations and reproduce the content word for word preserving the integrity of the article.
16. **Posting licensed content on any Website**: The following terms and conditions apply as follows: Licensing material from an Elsevier journal: All content posted to the web site must maintain the copyright information line on the bottom of each image; A hyper-text must be included to the Homepage of the journal from which you are licensing at http://www.sciencedirect.com/science/journal/xxxxx or the Elsevier homepage for books at http://www.elsevier.com; Central Storage: This license does not include permission for a scanned version of the material to be stored in a central repository such as that provided by Heron/XanEdu.
Licensing material from an Elsevier book: A hyper-text link must be included to the Elsevier homepage at http://www.elsevier.com . All content posted to the web site must maintain the copyright information line on the bottom of each image.

Posting licensed content on Electronic reserve: In addition to the above the following clauses are applicable: The web site must be password-protected and made available only to bona fide students registered on a relevant course. This permission is granted for 1 year only. You may obtain a new license for future website posting.
17. **For journal authors:** the following clauses are applicable in addition to the above:
Preprints:
A preprint is an author's own write-up of research results and analysis, it has not been peer-reviewed, nor has it had any other value added to it by a publisher (such as formatting, copyright, technical enhancement etc.).
Authors can share their preprints anywhere at any time. Preprints should not be added to or enhanced in any way in order to appear more like, or to substitute for, the final versions of articles however authors can update their preprints on arXiv or RePEc with their Accepted Author Manuscript (see below).
If accepted for publication, we encourage authors to link from the preprint to their formal publication via its DOI. Millions of researchers have access to the formal publications on ScienceDirect, and so links will help users to find, access, cite and use the best available

version. Please note that Cell Press, The Lancet and some society-owned have different preprint policies. Information on these policies is available on the journal homepage.
Accepted Author Manuscripts: An accepted author manuscript is the manuscript of an article that has been accepted for publication and which typically includes author-incorporated changes suggested during submission, peer review and editor-author communications.
Authors can share their accepted author manuscript:

- immediately
    - via their non-commercial person homepage or blog
    - by updating a preprint in arXiv or RePEc with the accepted manuscript
    - via their research institute or institutional repository for internal institutional uses or as part of an invitation-only research collaboration work-group
    - directly by providing copies to their students or to research collaborators for their personal use
    - for private scholarly sharing as part of an invitation-only work group on commercial sites with which Elsevier has an agreement
- after the embargo period
    - via non-commercial hosting platforms such as their institutional repository
    - via commercial sites with which Elsevier has an agreement

In all cases accepted manuscripts should:

- link to the formal publication via its DOI
- bear a CC-BY-NC-ND license - this is easy to do
- if aggregated with other manuscripts, for example in a repository or other site, be shared in alignment with our hosting policy not be added to or enhanced in any way to appear more like, or to substitute for, the published journal article.

Published journal article (JPA): A published journal article (PJA) is the definitive final record of published research that appears or will appear in the journal and embodies all value-adding publishing activities including peer review co-ordination, copy-editing, formatting, (if relevant) pagination and online enrichment.
Policies for sharing publishing journal articles differ for subscription and gold open access articles:
Subscription Articles: If you are an author, please share a link to your article rather than the full-text. Millions of researchers have access to the formal publications on ScienceDirect, and so links will help your users to find, access, cite, and use the best available version.
Theses and dissertations which contain embedded PJAs as part of the formal submission can be posted publicly by the awarding institution with DOI links back to the formal publications on ScienceDirect.
If you are affiliated with a library that subscribes to ScienceDirect you have additional private sharing rights for others' research accessed under that agreement. This includes use for classroom teaching and internal training at the institution (including use in course packs and courseware programs), and inclusion of the article for grant funding purposes.
Gold Open Access Articles: May be shared according to the author-selected end-user license and should contain a CrossMark logo, the end user license, and a DOI link to the formal publication on ScienceDirect.
Please refer to Elsevier's posting policy for further information.
18. **For book authors** the following clauses are applicable in addition to the above:
Authors are permitted to place a brief summary of their work online only. You are not allowed to download and post the published electronic version of your chapter, nor may you scan the printed edition to create an electronic version. **Posting to a repository:** Authors are permitted to post a summary of their chapter only in their institution's repository.

19. **Thesis/Dissertation**: If your license is for use in a thesis/dissertation your thesis may be submitted to your institution in either print or electronic form. Should your thesis be published commercially, please reapply for permission. These requirements include permission for the Library and Archives of Canada to supply single copies, on demand, of the complete thesis and include permission for Proquest/UMI to supply single copies, on demand, of the complete thesis. Should your thesis be published commercially, please reapply for permission. Theses and dissertations which contain embedded PJAs as part of the formal submission can be posted publicly by the awarding institution with DOI links back to the formal publications on ScienceDirect.

Elsevier Open Access Terms and Conditions

You can publish open access with Elsevier in hundreds of open access journals or in nearly 2000 established subscription journals that support open access publishing. Permitted third party re-use of these open access articles is defined by the author's choice of Creative Commons user license. See our open access license policy for more information.

Terms & Conditions applicable to all Open Access articles published with Elsevier:

Any reuse of the article must not represent the author as endorsing the adaptation of the article nor should the article be modified in such a way as to damage the author's honour or reputation. If any changes have been made, such changes must be clearly indicated.

The author(s) must be appropriately credited and we ask that you include the end user license and a DOI link to the formal publication on ScienceDirect.

If any part of the material to be used (for example, figures) has appeared in our publication with credit or acknowledgement to another source it is the responsibility of the user to ensure their reuse complies with the terms and conditions determined by the rights holder.

Additional Terms & Conditions applicable to each Creative Commons user license:

CC BY: The CC-BY license allows users to copy, to create extracts, abstracts and new works from the Article, to alter and revise the Article and to make commercial use of the Article (including reuse and/or resale of the Article by commercial entities), provided the user gives appropriate credit (with a link to the formal publication through the relevant DOI), provides a link to the license, indicates if changes were made and the licensor is not represented as endorsing the use made of the work. The full details of the license are available at http://creativecommons.org/licenses/by/4.0.

CC BY NC SA: The CC BY-NC-SA license allows users to copy, to create extracts, abstracts and new works from the Article, to alter and revise the Article, provided this is not done for commercial purposes, and that the user gives appropriate credit (with a link to the formal publication through the relevant DOI), provides a link to the license, indicates if changes were made and the licensor is not represented as endorsing the use made of the work. Further, any new works must be made available on the same conditions. The full details of the license are available at http://creativecommons.org/licenses/by-nc-sa/4.0.

CC BY NC ND: The CC BY-NC-ND license allows users to copy and distribute the Article, provided this is not done for commercial purposes and further does not permit distribution of the Article if it is changed or edited in any way, and provided the user gives appropriate credit (with a link to the formal publication through the relevant DOI), provides a link to the license, and that the licensor is not represented as endorsing the use made of the work. The full details of the license are available at http://creativecommons.org/licenses/by-nc-nd/4.0.

Any commercial reuse of Open Access articles published with a CC BY NC SA or CC BY NC ND license requires permission from Elsevier and will be subject to a fee.

Commercial reuse includes:

- Associating advertising with the full text of the Article
- Charging fees for document delivery or access
- Article aggregation
- Systematic distribution via e-mail lists or share buttons

Posting or linking by commercial companies for use by customers of those companies.

20. **Other Conditions**:

v1.8

Questions? customercare@copyright.com or +1-855-239-3415 (toll free in the US) or +1-978-646-2777.

ELSEVIER LICENSE
TERMS AND CONDITIONS

Sep 06, 2016

This Agreement between Chris Lane ("You") and Elsevier ("Elsevier") consists of your license details and the terms and conditions provided by Elsevier and Copyright Clearance Center.

License Number	3939130306606
License date	Aug 30, 2016
Licensed Content Publisher	Elsevier
Licensed Content Publication	Chemical Engineering Science
Licensed Content Title	Investigation of bubble swarm drag at elevated pressure in a contaminated system
Licensed Content Author	C.D. Lane,V. Parisien,A. Macchi,A.A. Donaldson
Licensed Content Date	2 October 2016
Licensed Content Volume Number	152
Licensed Content Issue Number	n/a
Licensed Content Pages	11
Start Page	381
End Page	391
Type of Use	reuse in a thesis/dissertation
Intended publisher of new work	other
Portion	full article
Format	electronic
Are you the author of this Elsevier article?	Yes
Will you be translating?	No
Order reference number	
Title of your thesis/dissertation	Modeling the Fluid Dynamics of a Commercial Ebullated Bed Hydroprocessor
Expected completion date	Aug 2016
Estimated size (number of pages)	136
Elsevier VAT number	GB 494 6272 12
Requestor Location	Chris Lane 311-633 W 8th Ave. Vancouver, BC V5Z 1C7 Canada Attn: Chris Lane
Total	0.00 USD

Terms and Conditions

INTRODUCTION

1. The publisher for this copyrighted material is Elsevier. By clicking "accept" in connection with completing this licensing transaction, you agree that the following terms and conditions apply to this transaction (along with the Billing and Payment terms and conditions established by Copyright Clearance Center, Inc. ("CCC"), at the time that you opened your Rightslink account and that are available at any time at http://myaccount.copyright.com).

GENERAL TERMS

2. Elsevier hereby grants you permission to reproduce the aforementioned material subject to the terms and conditions indicated.
3. Acknowledgement: If any part of the material to be used (for example, figures) has appeared in our publication with credit or acknowledgement to another source, permission must also be sought from that source. If such permission is not obtained then that material may not be included in your publication/copies. Suitable acknowledgement to the source must be made, either as a footnote or in a reference list at the end of your publication, as follows:
"Reprinted from Publication title, Vol /edition number, Author(s), Title of article / title of chapter, Pages No., Copyright (Year), with permission from Elsevier [OR APPLICABLE SOCIETY COPYRIGHT OWNER]." Also Lancet special credit - "Reprinted from The Lancet, Vol. number, Author(s), Title of article, Pages No., Copyright (Year), with permission from Elsevier."
4. Reproduction of this material is confined to the purpose and/or media for which permission is hereby given.
5. Altering/Modifying Material: Not Permitted. However figures and illustrations may be altered/adapted minimally to serve your work. Any other abbreviations, additions, deletions and/or any other alterations shall be made only with prior written authorization of Elsevier Ltd. (Please contact Elsevier at permissions@elsevier.com)
6. If the permission fee for the requested use of our material is waived in this instance, please be advised that your future requests for Elsevier materials may attract a fee.
7. Reservation of Rights: Publisher reserves all rights not specifically granted in the combination of (i) the license details provided by you and accepted in the course of this licensing transaction, (ii) these terms and conditions and (iii) CCC's Billing and Payment terms and conditions.
8. License Contingent Upon Payment: While you may exercise the rights licensed immediately upon issuance of the license at the end of the licensing process for the transaction, provided that you have disclosed complete and accurate details of your proposed use, no license is finally effective unless and until full payment is received from you (either by publisher or by CCC) as provided in CCC's Billing and Payment terms and conditions. If full payment is not received on a timely basis, then any license preliminarily granted shall be deemed automatically revoked and shall be void as if never granted. Further, in the event that you breach any of these terms and conditions or any of CCC's Billing and Payment terms and conditions, the license is automatically revoked and shall be void as if never granted. Use of materials as described in a revoked license, as well as any use of the materials beyond the scope of an unrevoked license, may constitute copyright infringement and publisher reserves the right to take any and all action to protect its copyright in the materials.
9. Warranties: Publisher makes no representations or warranties with respect to the licensed material.
10. Indemnity: You hereby indemnify and agree to hold harmless publisher and CCC, and their respective officers, directors, employees and agents, from and against any and all claims arising out of your use of the licensed material other than as specifically authorized pursuant to this license.
11. No Transfer of License: This license is personal to you and may not be sublicensed, assigned, or transferred by you to any other person without publisher's written permission.

12. No Amendment Except in Writing: This license may not be amended except in a writing signed by both parties (or, in the case of publisher, by CCC on publisher's behalf).
13. Objection to Contrary Terms: Publisher hereby objects to any terms contained in any purchase order, acknowledgment, check endorsement or other writing prepared by you, which terms are inconsistent with these terms and conditions or CCC's Billing and Payment terms and conditions. These terms and conditions, together with CCC's Billing and Payment terms and conditions (which are incorporated herein), comprise the entire agreement between you and publisher (and CCC) concerning this licensing transaction. In the event of any conflict between your obligations established by these terms and conditions and those established by CCC's Billing and Payment terms and conditions, these terms and conditions shall control.
14. Revocation: Elsevier or Copyright Clearance Center may deny the permissions described in this License at their sole discretion, for any reason or no reason, with a full refund payable to you. Notice of such denial will be made using the contact information provided by you. Failure to receive such notice will not alter or invalidate the denial. In no event will Elsevier or Copyright Clearance Center be responsible or liable for any costs, expenses or damage incurred by you as a result of a denial of your permission request, other than a refund of the amount(s) paid by you to Elsevier and/or Copyright Clearance Center for denied permissions.

LIMITED LICENSE

The following terms and conditions apply only to specific license types:
15. **Translation**: This permission is granted for non-exclusive world **English** rights only unless your license was granted for translation rights. If you licensed translation rights you may only translate this content into the languages you requested. A professional translator must perform all translations and reproduce the content word for word preserving the integrity of the article.
16. **Posting licensed content on any Website**: The following terms and conditions apply as follows: Licensing material from an Elsevier journal: All content posted to the web site must maintain the copyright information line on the bottom of each image; A hyper-text must be included to the Homepage of the journal from which you are licensing at http://www.sciencedirect.com/science/journal/xxxxx or the Elsevier homepage for books at http://www.elsevier.com; Central Storage: This license does not include permission for a scanned version of the material to be stored in a central repository such as that provided by Heron/XanEdu.
Licensing material from an Elsevier book: A hyper-text link must be included to the Elsevier homepage at http://www.elsevier.com . All content posted to the web site must maintain the copyright information line on the bottom of each image.

Posting licensed content on Electronic reserve: In addition to the above the following clauses are applicable: The web site must be password-protected and made available only to bona fide students registered on a relevant course. This permission is granted for 1 year only. You may obtain a new license for future website posting.
17. **For journal authors:** the following clauses are applicable in addition to the above:
Preprints:
A preprint is an author's own write-up of research results and analysis, it has not been peer-reviewed, nor has it had any other value added to it by a publisher (such as formatting, copyright, technical enhancement etc.).
Authors can share their preprints anywhere at any time. Preprints should not be added to or enhanced in any way in order to appear more like, or to substitute for, the final versions of articles however authors can update their preprints on arXiv or RePEc with their Accepted Author Manuscript (see below).
If accepted for publication, we encourage authors to link from the preprint to their formal publication via its DOI. Millions of researchers have access to the formal publications on ScienceDirect, and so links will help users to find, access, cite and use the best available

version. Please note that Cell Press, The Lancet and some society-owned have different preprint policies. Information on these policies is available on the journal homepage.
Accepted Author Manuscripts: An accepted author manuscript is the manuscript of an article that has been accepted for publication and which typically includes author-incorporated changes suggested during submission, peer review and editor-author communications.
Authors can share their accepted author manuscript:

- immediately
    - via their non-commercial person homepage or blog
    - by updating a preprint in arXiv or RePEc with the accepted manuscript
    - via their research institute or institutional repository for internal institutional uses or as part of an invitation-only research collaboration work-group
    - directly by providing copies to their students or to research collaborators for their personal use
    - for private scholarly sharing as part of an invitation-only work group on commercial sites with which Elsevier has an agreement
- after the embargo period
    - via non-commercial hosting platforms such as their institutional repository
    - via commercial sites with which Elsevier has an agreement

In all cases accepted manuscripts should:

- link to the formal publication via its DOI
- bear a CC-BY-NC-ND license - this is easy to do
- if aggregated with other manuscripts, for example in a repository or other site, be shared in alignment with our hosting policy not be added to or enhanced in any way to appear more like, or to substitute for, the published journal article.

Published journal article (JPA): A published journal article (PJA) is the definitive final record of published research that appears or will appear in the journal and embodies all value-adding publishing activities including peer review co-ordination, copy-editing, formatting, (if relevant) pagination and online enrichment.
Policies for sharing publishing journal articles differ for subscription and gold open access articles:
Subscription Articles: If you are an author, please share a link to your article rather than the full-text. Millions of researchers have access to the formal publications on ScienceDirect, and so links will help your users to find, access, cite, and use the best available version.
Theses and dissertations which contain embedded PJAs as part of the formal submission can be posted publicly by the awarding institution with DOI links back to the formal publications on ScienceDirect.
If you are affiliated with a library that subscribes to ScienceDirect you have additional private sharing rights for others' research accessed under that agreement. This includes use for classroom teaching and internal training at the institution (including use in course packs and courseware programs), and inclusion of the article for grant funding purposes.
Gold Open Access Articles: May be shared according to the author-selected end-user license and should contain a CrossMark logo, the end user license, and a DOI link to the formal publication on ScienceDirect.
Please refer to Elsevier's posting policy for further information.
18. **For book authors** the following clauses are applicable in addition to the above:
Authors are permitted to place a brief summary of their work online only. You are not allowed to download and post the published electronic version of your chapter, nor may you scan the printed edition to create an electronic version. **Posting to a repository:** Authors are permitted to post a summary of their chapter only in their institution's repository.

19. **Thesis/Dissertation**: If your license is for use in a thesis/dissertation your thesis may be submitted to your institution in either print or electronic form. Should your thesis be published commercially, please reapply for permission. These requirements include permission for the Library and Archives of Canada to supply single copies, on demand, of the complete thesis and include permission for Proquest/UMI to supply single copies, on demand, of the complete thesis. Should your thesis be published commercially, please reapply for permission. Theses and dissertations which contain embedded PJAs as part of the formal submission can be posted publicly by the awarding institution with DOI links back to the formal publications on ScienceDirect.

Elsevier Open Access Terms and Conditions

You can publish open access with Elsevier in hundreds of open access journals or in nearly 2000 established subscription journals that support open access publishing. Permitted third party re-use of these open access articles is defined by the author's choice of Creative Commons user license. See our open access license policy for more information.

Terms & Conditions applicable to all Open Access articles published with Elsevier:

Any reuse of the article must not represent the author as endorsing the adaptation of the article nor should the article be modified in such a way as to damage the author's honour or reputation. If any changes have been made, such changes must be clearly indicated.

The author(s) must be appropriately credited and we ask that you include the end user license and a DOI link to the formal publication on ScienceDirect.

If any part of the material to be used (for example, figures) has appeared in our publication with credit or acknowledgement to another source it is the responsibility of the user to ensure their reuse complies with the terms and conditions determined by the rights holder.

Additional Terms & Conditions applicable to each Creative Commons user license:

CC BY: The CC-BY license allows users to copy, to create extracts, abstracts and new works from the Article, to alter and revise the Article and to make commercial use of the Article (including reuse and/or resale of the Article by commercial entities), provided the user gives appropriate credit (with a link to the formal publication through the relevant DOI), provides a link to the license, indicates if changes were made and the licensor is not represented as endorsing the use made of the work. The full details of the license are available at http://creativecommons.org/licenses/by/4.0.

CC BY NC SA: The CC BY-NC-SA license allows users to copy, to create extracts, abstracts and new works from the Article, to alter and revise the Article, provided this is not done for commercial purposes, and that the user gives appropriate credit (with a link to the formal publication through the relevant DOI), provides a link to the license, indicates if changes were made and the licensor is not represented as endorsing the use made of the work. Further, any new works must be made available on the same conditions. The full details of the license are available at http://creativecommons.org/licenses/by-nc-sa/4.0.

CC BY NC ND: The CC BY-NC-ND license allows users to copy and distribute the Article, provided this is not done for commercial purposes and further does not permit distribution of the Article if it is changed or edited in any way, and provided the user gives appropriate credit (with a link to the formal publication through the relevant DOI), provides a link to the license, and that the licensor is not represented as endorsing the use made of the work. The full details of the license are available at http://creativecommons.org/licenses/by-nc-nd/4.0.

Any commercial reuse of Open Access articles published with a CC BY NC SA or CC BY NC ND license requires permission from Elsevier and will be subject to a fee.

Commercial reuse includes:

- Associating advertising with the full text of the Article
- Charging fees for document delivery or access
- Article aggregation
- Systematic distribution via e-mail lists or share buttons

Posting or linking by commercial companies for use by customers of those companies.

20. **Other Conditions**:

v1.8

Questions? customercare@copyright.com or +1-855-239-3415 (toll free in the US) or +1-978-646-2777.